

Biomolecular Diffusion in Nanofluidics

THÈSE N° 4736 (2010)

PRÉSENTÉE LE 16 JUILLET 2010

À LA FACULTÉ SCIENCES ET TECHNIQUES DE L'INGÉNIEUR
LABORATOIRE DE MICROSYSTÈMES 4
PROGRAMME DOCTORAL EN MICROSYSTÈMES ET MICROÉLECTRONIQUE

ÉCOLE POLYTECHNIQUE FÉDÉRALE DE LAUSANNE

POUR L'OBTENTION DU GRADE DE DOCTEUR ÈS SCIENCES

PAR

Nicolas DURAND

acceptée sur proposition du jury:

Prof. J. Brugger, président du jury
Prof. Ph. Renaud, Prof. T. Lasser, directeurs de thèse
Prof. J. C. Eijkel, rapporteur
A. Sayah, rapporteur
Prof. J. Schrenzel, rapporteur



ÉCOLE POLYTECHNIQUE
FÉDÉRALE DE LAUSANNE

Suisse
2010

A ma chère Aline, qui m'a soutenu chaque jour de cet ouvrage

A mes parents, qui m'ont toujours montré la bonne direction à prendre

*L'homme est infiniment grand par rapport à l'infiniment petit
et infiniment petit par rapport à l'infiniment grand ;
ce qui le réduit presque à zéro.*

VLADIMIR JANKÉLÉVITCH (1903 - 1985)

Abstract

Imagine a small integrated biomedical analysis laboratory, connected to your home computer, which would be capable of diagnosing illnesses, a lack of vitamins, or the over-presence of substances from samples of blood, urine or saliva. This hypothetic system would be able to give a diagnosis within minutes, finally advising the user about the optimal targeted medicines to take or the right specialist to consult for fast recovery.

Of course this system will not be ready in the near future, but this thesis aims to bring some new elements to this exciting project by investigating the diffusion of proteins in well-defined nanometer-sized confined areas. Understanding molecular dynamics in nanoconfinement volumes is fundamental for designing the appropriate lab-on-a-chip devices able to transport, pre-concentrate, separate and sense biomolecules. However, a multitude of phenomena occurring at the nanoscale are still to be discovered and currently, there is a lack of accurate theoretical models to predict the transport of proteins in nanofluidics.

Based on measurements performed in 50 nm high 1D nanochannels, where the surface-to-volume ratio is extremely high, protein-surface interactions were initially investigated. Using electrical measurements, the adsorption and desorption kinetics of highly concentrated bovine serum albumin proteins was characterized in different scenarios. Ionic strength conditions were identified, where the electrical conductance is dominated by volume effects due to the adsorbed or bound proteins, leading to potential applications of rapid immunology on-chip. Other situations, where the protein charges were directly influencing the nanochannel conductance, were also highlighted, giving a better understanding of how the adsorbed proteins counterions modify the surface charges.

Furthermore, the transport of single proteins diffusing through nanochannels was analyzed using fluorescence correlation spectroscopy. Direct measurements inside nanochannels has allowed the identification of different

regimes of interacting proteins, depending on the thickness of the electrical double layer (constituted of immobile ions which equilibrate the surface charges). Taking into account the steric exclusion due to the small channel size, the reversible surface adsorption, and the exclusion-enrichment effect due to the charge of the proteins and ionic strength of the solution, novel theoretical models describing the hindered diffusion of proteins were elaborated. Conditions where the diffusion of proteins through the nanochannels were of the same magnitude as in the bulk were both predicted and experimentally verified.

Finally, a novel method is presented to measure the apparent diffusion coefficients of fluorescently-labeled molecules directly inside a nanofluidic system. This technique, based on steady-state dispersion of proteins in a transversal nanoslit, demonstrates that under specific ionic conditions, the apparent diffusion coefficient of wheat germ agglutinin proteins is four orders of magnitude lower than its free diffusion value. Based on this system, the binding affinity of two different proteins was directly measured, demonstrating the potential of this method to be used as a biosensor for quantifying rapid protein complex formation.

This thesis mainly deals with fundamental studies related to surface physics and physical chemistry applied to life sciences. The work points out novel, important, experimentally-verified complements to define solid theoretical models, in order to go forward with the design of complex nanofluidic systems applied to biomedical and biological applications.

Keywords: *adsorption, apparent diffusion coefficient, biomolecules, conductance, desorption, diffusion, dispersion, effective diffusion coefficient, electrical double layer, fluorescence correlation spectroscopy, ionic strength, lab-on-a-chip, micro total analysis system, nanochannel, nanoelectromechanical systems, nanofluidics, nanoslit, protein-surface interaction, proteomics, separation, surface charge.*

Version abrégée

Imaginez un petit appareil connectable à votre ordinateur, dans lequel serait miniaturisé un laboratoire d'analyse biomédicale, et que vous pourriez utiliser de temps en temps pour diagnostiquer une maladie, un manque de vitamines ou encore la présence anormale d'une substance depuis un échantillon de sang, d'urine ou de salive. Ce système futuriste pourrait fournir un diagnostic complet en quelques minutes et ainsi conseiller à l'utilisateur le remède optimal à prendre ou le bon spécialiste à consulter afin d'arrêter la progression de la maladie et de guérir rapidement.

Actuellement, la technologie ne permet pas encore de réaliser un tel appareil, mais cette thèse s'est donné pour objectif d'y contribuer en étudiant la diffusion de biomolécules dans des espaces confinés à une échelle nanométrique. Une bonne compréhension de la physique des fluides confinés est fondamentale pour le développement de « micro laboratoires sur puce », capables de transporter, de préconcentrer, de séparer et même d'identifier des biomolécules.

En se basant sur des mesures réalisées dans des canaux nanométriques (50 nm de hauteur), pour lesquels le rapport surface sur volume est extrêmement haut, les cinétiques d'adsorption et de désorption entre protéines et surfaces ont été mesurées électriquement avec succès. Les conditions ioniques où la conductivité électrique est dominée par les effets de réduction de volume (dus aux protéines qui adsorbent aux surfaces) ont été identifiées, ouvrant ainsi des perspectives intéressantes pour des applications d'immunologie sur puce par exemple. D'autres conditions pour lesquelles les charges des protéines influencent directement la conductance électrique des nanocanaux ont également été identifiées, apportant une meilleure compréhension de la façon dont les contre-ions des protéines adsorbées modifient les charges de surface effectives.

De plus, le transport de protéines isolées diffusant à travers des nanocanaux, a été analysé au moyen de la spectroscopie de corrélation de fluorescence.

Des mesures réalisées directement à l'intérieur des nanocanaux ont permis l'identification de plusieurs régimes d'interactions entre protéines et surfaces, dépendant notamment de l'épaisseur de la couche électrique double (constituée de ions immobiles compensant les charges de surface). En tenant compte de l'exclusion stérique, de l'adsorption réversible entre protéines et surfaces et des effets d'exclusion et d'enrichissement, de nouveaux modèles théoriques décrivant la diffusion de protéines en milieux confinés ont été élaborés. Les conditions, pour lesquelles la diffusion des protéines au travers des nanocanaux est du même ordre de grandeur que leur coefficient de diffusion libre, ont été prédites et vérifiées expérimentalement.

Finalement, une nouvelle méthode pour mesurer directement les coefficients de diffusion apparents de biomolécules à l'intérieur de systèmes nanofluidiques est présentée. Cette technique, basée sur un état d'équilibre de dispersion des protéines dans une nanofente transversale, démontre que pour certaines conditions ioniques, le coefficient de diffusion apparent des protéines est plusieurs ordres de grandeur inférieur à leur coefficient de diffusion standard. Grâce à ce système, l'affinité moléculaire entre deux types de protéines différentes a pu être mesurée, assurant à cette méthode un intéressant potentiel comme biocapteur pour quantifier rapidement la formation de protéines.

Cette thèse apporte des éclaircissements sur certains principes fondamentaux reliés à la physique des surfaces et à la chimie physique appliquées aux sciences de la vie. Plusieurs nouveaux modèles théoriques, vérifiés expérimentalement, sont élaborés en vue d'améliorer le design de systèmes nanofluidiques pour des applications biomédicales et biologiques.

Mots-clés: *adsorption, biomolécules, conductance, désorption, diffusion, dispersion, coefficient de diffusion apparent, coefficient de diffusion effectif, couche électrique double, spectroscopie de corrélation de fluorescence, force ionique, laboratoire sur puce, nanocanal, systèmes nanoélectromécaniques, nanofluidique, nanofente, interaction protéine-surface, protéomique, séparation, charge de surface.*

Acknowledgements

First of all, I would like to thank my thesis director Prof. Philippe Renaud who closely guided this work. I express my deepest gratitude for introducing me to the wonderful world of micro and nanosystems. I have appreciated the freedom he provided me and his availability for discussion. Moreover, I thank him for giving useful advice and great ideas.

I am also particularly grateful to my thesis co-director Prof. Theo Lasser, who opened his laboratory to me. I thank him for his motivation, his efficiency, and most of all, to have actively participated in helping me to realize my dream: to found a company.

I express my gratitude to Prof. Jan Eijkel, Prof. Jacques Schrenzel and Dr. Abdeljalil Sayah, for having accepted to be members of the jury of my thesis and Prof. Jürgen Brugger for having accepted to the position of President of the jury. I appreciate their valuable comments and feedback.

I would like to deeply acknowledge my predecessors in nanofluidics Dr. Reto Schoch and Dr. Adrien Plecis, and to all my Masters students for their great work: Raphaël Goetschmann, Gaspard Pardon, Joël Stadelmann, Arthur Queval, Nicolas Rebeaud, Elli Saveriades, Thomas Lanvin, Jean-Baptiste Gay and Stefano Varricchio.

Many thanks to Dr. Arnaud Bertsch, Dr. André Mercanzini, Kristopher Pataky, Dr. Erica Martin-Williams and Jennifer Franz for being my proof-reader. I have really appreciated their help in reading this manuscript, as well as correcting my English.

A big thank you to the secretaries, Kathlyn Mayor, Sylvie Clavel, Rose-Mary Apothéloz, Marie Halm, Judith Chaubert and Claudia D'Agostino, for their professionalism, efficiency, and of course their consistent good humor which was greatly appreciated.

I am particularly grateful to my office mates, Lynda Metref, Mina Todorova and Harsha Kasi, for having supported me. We definitively shared a good time!

My deepest gratitude goes to Raphaël Tornay, Nicolas Demierre, Yves Moser, Vahid Fakhfour, Emile Dupont, Frédéric Lacharme, Pierre Joris, Jean-Baptiste Orhan, Rana Afshar, Ulrike Lehmann, Sophie Baranek, André Mercanzini, Alessandro Mapelli, Matteo Leonardi, Jagoda Dobrzynska, Sébastien Jiguet, Marc Heuschkel, Mario Schlund, Marc Boers, Matthias Geissbühler, Iwan Märki, Greg del Val, Yannick Fournier and Lionel Micol for their friendship and for all the lunches and breaks we shared (including babyfoots, UT, darts, Sat, bugnettes, chinese hot pot, etc.).

I also warmly thank all other former and actual colleagues in the LMIS and LOB, especially Ana, Anja, Camille, Claudio, Daniel, Elodie, Fabien, Guillaume, Harald, Joël, Ludovica, Martin, Michaël, Nazar, Nicolas Abelé, Nina, Noelia, Pontus, Raphaël F., Rob, Ronit, Shady, Thomas, Venkat, Willyan, and all the others I may have forgotten...

Thanks to Prof. Marc Pfeifer, Denis Prim and Rémy Dufresne from HES-SO Sion for their expertise in biotechnology.

Many thanks to all the technicians, in particular the cleanroom staff, the microengineering workshop mechanics, and the Printed Circuit Board staff.

I would like to congratulate the committee of Robopoly and AéroPoly for everything we have accomplished together. I really had fun with you guys!

Finally, I especially thank my parents Francine and Marc, and my sister Marilyne, who have always let me choose my way and have supported me morally and financially. I would never have accomplished this thesis without their help and their encouragements.

Last but not least, I most heartily thank my wife Aline who gave me the energy day after day to overcome this long work.

THANK YOU!

Lausanne, April 2010

Nicolas Durand

CONTENTS

Abstract	vii
Version abrégée	ix
Acknowledgements	xi
Contents	xvi
Nomenclature	xvii
1 Introduction	1
1.1 Towards miniaturization	2
1.2 Lab-on-a-Chip	3
1.3 The origins of nanofluidics	5
1.4 Main nanofluidics achievements up-to-date	6
1.4.1 Methods for fabricating nanofluidic structures	6
Top-down methods	6
Bottom-up methods	8
Examples of microfabricated nanofluidic devices	9
1.4.2 Sensing, sequencing and actuation using nanofluidic structures . .	10
1.4.3 Separation and preconcentration using nanofluidic structures . .	13

1.5	Motivation and scope of this thesis	17
1.6	Thesis structure	19
2	Transport phenomena in nanofluidics	21
2.1	Forces in nanofluidics	22
	Solvation forces	22
	Fluctuation forces	23
	Van der Waals forces	23
	Electrostatic forces	24
	Other forces	24
2.2	Fluid dynamics at nanoscale	24
	2.2.1 Low Reynolds number fluidics	26
	2.2.2 Pressure-driven flow	26
2.3	Molecular diffusion in liquids	27
	2.3.1 Brownian motion	28
	2.3.2 Diffusion in concentrated solutions	29
2.4	Electrostatics in liquids	30
	2.4.1 Surface charge density	30
	2.4.2 Potential distribution and electrical double layer	30
	2.4.3 Electrical double layer in 1D nanochannels	32
2.5	Biomolecules and their environment	34
2.6	Conclusion	35
3	Fabrication and experimental setup	37
3.1	System design and fabrication	38
	3.1.1 Microfabrication process	39
	3.1.2 Chip design	39
	3.1.3 Experimental setup	42
	Electrical setup	44
	FCS setup	44
	Microscope setup	45
3.2	Chip characterization	45

3.2.1	Surface roughness and glass dissolution	45
3.2.2	Electrical characterization	46
3.3	Conclusion	48
4	Electrical detection of proteins kinetics in nanoconfinements	49
4.1	Motivation	50
4.2	Adsorption and desorption kinetics	51
4.3	Hindered diffusion of proteins in nanoconfined spaces	52
4.3.1	The partitioning effect	52
4.4	Effect of the presence of proteins on the nanoslit conductance	55
4.5	Electrical measurements	58
4.5.1	Adsorption kinetics at high ionic strength	58
	Effect of an induced flow on the electrical conductance	61
	Effect of pH and ionic strength variations	62
4.5.2	Adsorption kinetics at low ionic strength	63
4.6	Outlook and conclusions	65
5	Direct measurements of diffusing species using FCS	67
5.1	Single molecule detection in nanochannels using FCS	68
5.2	Materials and methods	71
5.3	Results and discussion	72
5.3.1	3D diffusion of WGA	72
5.3.2	Exclusion of proteins from the nanochannel at low ionic strength	72
5.3.3	Confined diffusion of negatively charged proteins	74
5.4	Gradient profile across a nanochannel	77
5.4.1	Simple diffusive case	77
5.4.2	Diffusion and convection	79
5.5	Outlook and conclusions	81

6	Apparent diffusion measurement using steady-state dispersion	83
6.1	Apparent diffusion in nanoconfinements	84
6.2	Steady-state dispersion effects	86
6.2.1	Theory	87
6.2.2	Finite element analysis	90
6.3	Single-component dispersion experiments	91
	Materials and methods	91
	Results and discussion	92
6.4	Detecting proteins complex formation	93
	Materials and methods	94
	Results and discussion	94
6.5	Outlook and conclusions	97
7	Conclusion and outlook	99
7.1	Summary of achievements and recommendations	100
7.1.1	Electrical detection of protein-surface interaction	100
7.1.2	Transition between surface-dominated and bulk diffusion regimes	102
7.1.3	Measurement of apparent diffusion coefficient	104
7.1.4	Detection of protein complex formation	105
7.2	Future perspectives	105
7.2.1	Technical improvements	106
7.2.2	Biomedical and biological applications	107
	Immunology on-chip	107
	Solving DNA puzzles	107
	Combine sieving, preconcentration and sensing	109
7.3	Concluding remarks	109
	Bibliography	127
	A Curriculum Vitae	129
	B Publications	133

NOMENCLATURE

Variables and constants

α	Constant retention parameter	[-]
β	Dimensionless position	[-]
χ	Bulk-surface partitioning cofactor	[-]
ΔP	Pressure variation	[Pa]
η	Solvent viscosity	[Pa·s]
Γ	Surface concentration of bound molecules	[mol·m ⁻²]
Γ_0	Effective surface coverage	[mol·m ⁻²]
Γ_{max}	Full coverage surface concentration	[mol·m ⁻²]
λ	Ratio of the solute diameter to nanochannel height	[-]
λ_D	Debye length	[m]
$\langle c_{nC} \rangle$	Mean concentration of solute in the nanochannel	[M]
μ	Ionic mobility	[m ² ·V ⁻¹ ·s ⁻¹]
ν_{kin}	Kinematic viscosity	[m ² ·s ⁻¹]
ω	Aspect ratio of the sampling volume	[-]

NOMENCLATURE

Φ	Flow of solution in the microchannel	[l·s ⁻¹]
Φ_β	Partitioning coefficient	[-]
Φ_m	Mass flow of solution	[kg·s ⁻¹]
Φ_{nC}	Equilibrium partitioning coefficient	[-]
Ψ	Debye-Hückel approximation for the electrical potential	[V]
Ψ	Electric potential due to surface charge	[V]
Ψ_S	Surface potential	[V]
ρ	Density	[kg·m ⁻³]
ρ_r	Electrical resistivity of the medium	[Ω·m]
σ_0	Surface charge density	[C·m ⁻²]
σ_S	Effective surface charge density	[C·m ⁻²]
τ	Time constant	[s]
τ_{bulk}	Bulk diffusion time	[s]
τ_D	Characteristic time of diffusion	[s]
τ_{eff}	Effective diffusion time	[s]
τ_{surf}	Surface diffusion time	[s]
θ	Parametric angle coordinate for the flow position	[°]
ε_0	Permittivity of vacuum (= 8.85·10 ⁻¹²)	[F·m ⁻¹]
ε_r	Dielectric constant of the medium	[-]
ζ	Electric potential due to surface charge	[V]
ζ	Zeta potential	[V]
A	Cross-sectional area	[m ²]
c	Concentration	[mol·m ⁻³]
c_0	Protein concentration	[M]

NOMENCLATURE

C_{EDL}	Electrical double layer capacitance	[F]
c_i	Electrolyte ionic concentration	[M]
C_{stray}	Parasitic capacitance	[F]
D	Diffusion coefficient	$[\text{m}^2 \cdot \text{s}^{-1}]$
D_{app}	Apparent diffusion coefficient	$[\text{m}^2 \cdot \text{s}^{-1}]$
D_{bulk}	Bulk diffusion coefficient	$[\text{m}^2 \cdot \text{s}^{-1}]$
D_{eff}	Effective diffusion coefficient	$[\text{m}^2 \cdot \text{s}^{-1}]$
D_{surf}	Surface diffusion coefficient	$[\text{m}^2 \cdot \text{s}^{-1}]$
d_s	Solute diameter	[m]
e	Electron charge ($= 1.6 \cdot 10^{-19}$)	[C]
E_a	Activation energy	$[\text{J} \cdot \text{mol}^{-1}]$
F	Faraday constant ($= 9.65 \cdot 10^4$)	$[\text{C} \cdot \text{mol}^{-1}]$
f	Friction coefficient of the solute	$[\text{Pa} \cdot \text{m} \cdot \text{s}]$
f_0	Working frequency	[Hz]
G	Nanoslit conductance	[S]
G_τ	Autocorrelation function	[-]
G_S	Surface conductance	[S]
G_V	Bulk conductance	[S]
$h_{\mu C}$	Microchannel height	[m]
h_{nC}	Nanochannel height	[m]
h_{nS}	Nanoslit height	[m]
I_B	Background intensity	[Hz]
I_{tot}	Total intensity	[Hz]
J	Flux per unit area	$[\text{mol} \cdot \text{m}^{-2} \cdot \text{s}^{-1}]$

NOMENCLATURE

K	Equilibrium constant	$[M^{-1}]$
k_B	Boltzmann constant ($= 9.65 \cdot 10^{-23}$)	$[J \cdot K^{-1}]$
k_{off}	Rate of desorption	$[s^{-1}]$
k_{on}	Rate of adsorption	$[M^{-1} \cdot s^{-1}]$
l_{nC}	Nanochannel length	$[m]$
l_{nS}	Nanoslit length	$[m]$
M	Total amount of solute	$[mol]$
N_A	Avogadro constant ($= 6.022 \cdot 10^{23}$)	$[mol^{-1}]$
n_{i0}	Ionic concentration away from the surface	$[m^{-3}]$
n_p	Charge of one protein	$[-]$
NA	Numerical aperture	$[-]$
q	Net charge of the solute	$[e]$
R	Molecular gas constant ($= 8.31$)	$[J \cdot mol^{-1} \cdot K^{-1}]$
$R_{\mu C}$	Microchannel electrical resistance	$[\Omega]$
R_{Φ}	Hydrodynamic resistance	$[m^{-1} \cdot s^{-1}]$
R_{nS}	Nanoslit electrical resistance	$[\Omega]$
r_{nS}	Parametric coordinate for the flow position	$[m]$
r_s	Protein radius (assuming spherical model)	$[m]$
r_{xy}	Radius of the microscope observation volume	$[m]$
r_z	Half of the microscope observation volume height	$[m]$
s	Substitution variable	$[-]$
S_{nC}	Nanochannel section	$[m^2]$
T	Temperature	$[K]$
t	Time	$[s]$

NOMENCLATURE

u	Flow velocity	$[\text{m}\cdot\text{s}^{-1}]$
u_0	Initial flow velocity	$[\text{m}\cdot\text{s}^{-1}]$
V	Nanoconfinement volume	$[\text{m}^3]$
V_0	Initial volume	$[\text{m}^3]$
w_{nC}	Nanochannel width	$[\text{m}]$
w_{nS}	Nanoslit width	$[\text{m}]$
x	Projection axis parallel to the nanochannel	$[\text{m}]$
y	Projection axis parallel to the microchannel	$[\text{m}]$
z	Projection axis parallel to the height	$[\text{m}]$
z_i	Valency of ion i	$[-]$
pH	Hydrogen potential	$[-]$
pI	Isoelectric point	$[-]$

Abbreviations

μ TAS	Micro Total Analysis Systems
ACF	Autocorrelation Function
AFM	Atomic Force Microscopy
ANA	Anisotropic Nanofilter Array
APD	Avalanche Photo Diode
aSi	Amorphous Silicon
BSA	Bovine Serum Albumin
CE	Capillary Electrophoresis
CMI	Center of MicroNanoTechnology, EPFL
CNT	Carbon Nanotubes
CVD	Chemical Vapor Deposition

NOMENCLATURE

DI water	Deionized water
DLVO	Theory elaborated by Derjaguin, Landau, Verwey and Overbeek
DNA	Deoxyribonucleic Acid
DRIE	Deep Reactive Ion Etching
EBL	Electron-Beam Lithography
EDL	Electrical Double Layer
EDLO	Electrical Double Layer Overlap
ELISA	Enzyme Linked Immunosorbent Assay
EPFL	Ecole Polytechnique Fédérale de Lausanne
FCS	Fluorescence Correlation Spectroscopy
FEM	Finite Element Method
FIB	Focused Ion Beam
FITC	Fluorescein Isothiocyanate
HIV	Human Immunodeficiency Virus
HPLC	High Performance Liquid Chromatography
HUG	Hôpitaux Universitaires de Genève
LCR	Inductance (L), Capacitance (C), Resistance (R)
LOC	Lab-On-a-Chip
MD	Molecular Dynamics simulations
MEMS	Microelectromechanical Systems
NEMS	Nanoelectromechanical Systems
NMR	Nuclear Magnetic Resonance
OWLS	Optical Waveguide Lightmode Spectroscopy
PBS	Phosphate Buffered Saline

NOMENCLATURE

PCR	Polymerase Chain Reaction
PMMA	Poly-Methyl-Methacrylate
rGFP	Recombinant Green Fluorescent Proteins
RNA	Ribonucleic Acid
SEM	Scanning Electron Microscopy
SPR	Surface Plasmon Resonance
TIR-FCS	Total Internal Reflection Fluorescence Correlation Spectroscopy
TIRF	Total Internal Reflectance Fluorescence
UV	Ultraviolet
WGA	Wheat Germ Agglutinin

NOMENCLATURE

CHAPTER

1

INTRODUCTION

This chapter gives an introduction to nanofluidics. A first section will provide the reader with an overview of miniaturized systems, followed by a focus on the lab-on-a-chip concept leading to nanofluidic systems. After a short introduction on nanofluidics notion and history, the main achievements will be presented, with emphasis on the devices fabrication, and their use for sensing and manipulating biomolecules. Finally, the motivation, scope, and outline of this thesis will be described.

"I would like to describe a field, in which little has been done, but in which an enormous amount can be done in principle. This field is not quite the same as the others in that it will not tell us much of fundamental physics but it is more like solid-state physics in the sense that it might tell us much of great interest about the strange phenomena that occur in complex situations. Furthermore, a point that is most important is that it would have an enormous number of technical applications."

Richard Feynman, 1959

1. INTRODUCTION

1.1 Towards miniaturization

Over the last two decades, significant steps have been performed in miniaturization. Thanks to advancements in fabrication techniques of the semiconductor device, mechanical, fluidic, electromechanical, and thermal systems have been miniaturized down to the nanometer scale. In the 1990's, these successful advancements lead to a new field of interest, microelectromechanical systems (MEMS); after 2000, to the nanoelectromechanical systems (NEMS). Electrostatic, magnetic, electromagnetic, pneumatic, and thermal actuators, motors, valves, gears, cantilevers, diaphragms and tweezers less than $100\ \mu\text{m}$ in size have been fabricated. These have been used as sensors for pressure, temperature, mass flow, velocity, sound and chemical compositions, such as actuators for linear and angular motions, and as simple components for complex systems, such as robots, micro-heat-engines and micro-heat-pumps.¹

One of the most successful examples of MEMS technology currently available in industry is the accelerometer. First introduced by Analog Devices in 1991, accelerometers are now widely used in automobiles, where they control the airbag's release in case of an accident. Another famous example is the arrays of micro-mirrors used in some video projectors: every micro-mirror is electrically actuated several hundred times per second and corresponds to each pixel creating the projected picture. Figure 1.1 shows a microscopy picture of microfabricated mirrors for embedded video projection in future mobile phones, from Lemoptix SA.

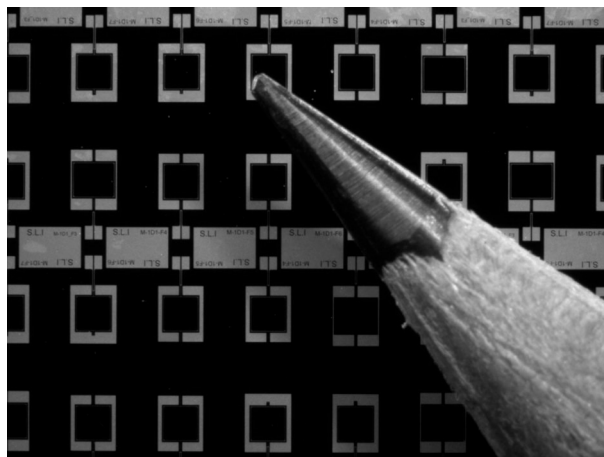


Figure 1.1: Microscopy picture of microfabricated mirrors for projection systems. From Lemoptix SA. The size of the pencil tip gives an idea of the size of the mirrors.

In applications like medical diagnostics, miniaturization offers the potential of low sample consumption, high throughput, integration, automation and fast analysis times. The emphasis is mainly on finding the compromise among cost, performance, and time to result, leading to single-use devices that reduce cross-contamination. Thus, scientists have developed miniaturized laboratories (Lab-on-a-Chip) integrating one or several laboratory functions on a single chip, from only millimeters in size to a few square centimeters.

1.2 Lab-on-a-Chip

Lab-on-a-chip systems (LOC), also called micro total analysis systems (μ TAS), deal with the handling of extremely small fluid volumes down to attoliters. Their development is driven by the desire for faster, lower cost analysis of complex sample mixture in a single, compact device. The idea is to detect biomolecules, to transport, mix and characterize them from a sample directly taken from the patient. In standard genomic analysis, the deoxyribonucleic acid (DNA) molecules have to be purified and amplified before being analyzed. If this non-trivial work can be integrated directly inside the micro device, complex diagnostics would be performed directly from the scratch sample. Figure 1.2 illustrates the concept of a LOC developed by Agilent Technologies which allows the genotype (identification of viruses in this case) from DNA strands. In this example, the integration is not complete as there is still the need for a computer system to extract and treat the data.

LOC development also opens new fields of applications like water and food quality analysis—fields with markets measured in billions of dollars per year.

Huge effort is now put on the development of large-scale integrated LOC using different functional units. For example, Hong and Quake³ have developed a nanofluidic system that can be used for parallelized high-throughput screening of fluorescence-based single-cell array. As shown in figure 1.3, the various inputs are loaded with food dyes to show the channels and sub-elements of the fluidic logic. Their chip has 2,056 valves, which are used to manipulate 256 compartments containing bacterial cells expressing an enzyme of interest that are combined on a pairwise basis with 256 other compartments containing a fluorogenic substrate used to assay for a desired activity. Cells that display a particularly interesting activity can be selected and recovered from the chip using valve-based addressing of the compartments.

The introduction of LOC has generated a renewed interest in microfluidics, which deals with micrometric channels, as well as, more recently, in nanofluidics, which is

1. INTRODUCTION

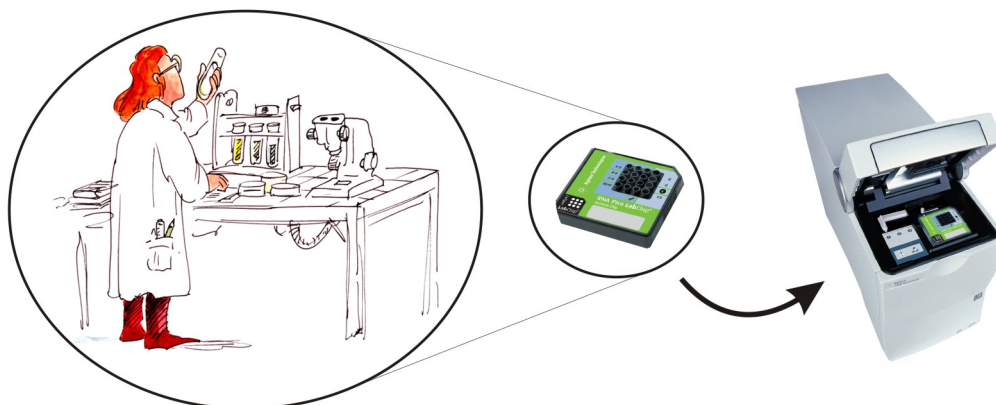


Figure 1.2: Concept of Lab-on-a-Chip. The laboratory illustration is adapted from the DRASS². RNA 6000 Pico Kit Guide from Agilent.

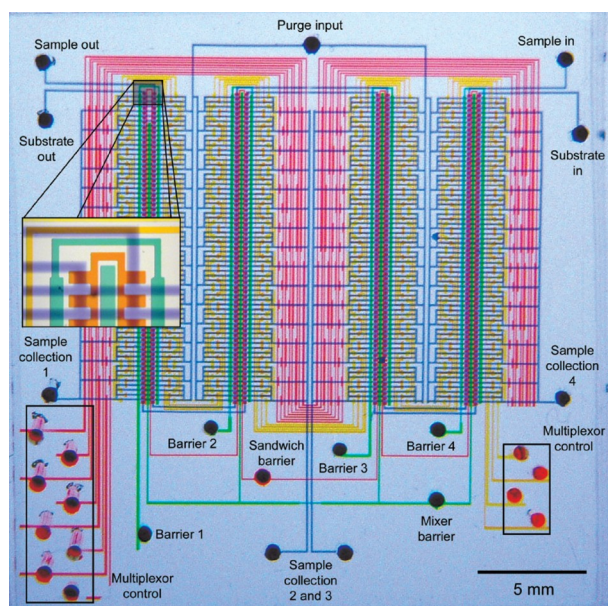


Figure 1.3: Optical micrograph of a large-scale integrated nanofluidic system. Adapted from Hong and Quake³

often defined as the study and application of fluid flow in and around structures with features that measure less than 100 nm in one or more directions⁴.

1.3 The origins of nanofluidics

Although nanofluidics is considered as a new field of research, the study of fluidic motion at small size scale has always been part of several physical and engineering areas. For example, oil transport through nanoporous filters has been important in petroleum engineering for a long time.

Figure 1.4 shows a schematic diagram indicating the great number of classical disciplines directly related to nanofluidics. It highlights the multidisciplinary approach needed for the great diversity of the field.

Nanofluidics is still in the early stage, but already allows one to take advantage of phenomena that do not exist at the macro-scale. This field has steadily gained interest over the last decade, as demonstrated by the increasing number of scientific publications (illustrated in figure 1.5).

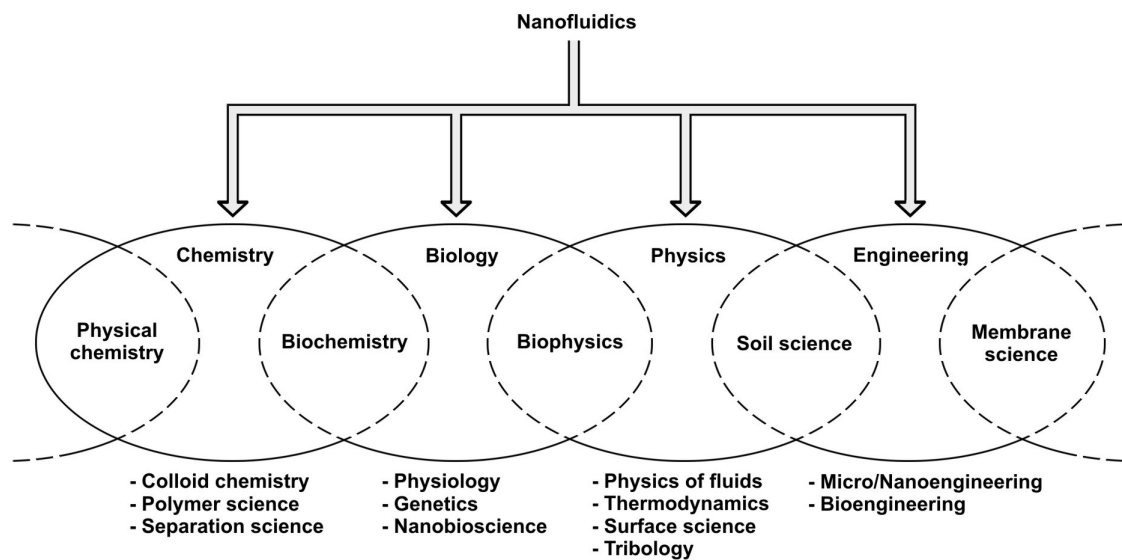


Figure 1.4: Classical disciplines related to nanofluidics and some relevant subjects studied. Adapted from Eijkel *et al.*⁴

1. INTRODUCTION

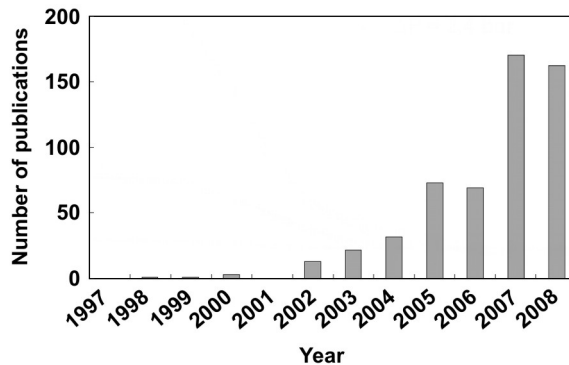


Figure 1.5: Number of articles on nanofluidics and its variations for the last decade (taken from ISI Web of Knowledge).

1.4 Main nanofluidics achievements up-to-date

Nanofluidics is becoming a major field of research^{5;6} and has been applied in microfluidic systems allowing for DNA manipulation⁷, protein separation^{8;9}, sample preconcentration¹⁰, and single molecule detection¹¹. The majority of current nanofluidic research is intended for bioengineering and biotechnology applications. This section covers some of the recent and significant publications and patents relating to nanofluidic devices, and methods for fabricating such devices.

1.4.1 Methods for fabricating nanofluidic structures

Firstly, an overview of the current techniques employed in nanofluidic device fabrication is presented. As proposed by Mijatovic *et al.*¹², fabrication of nanofluidic devices can be divided roughly into two categories: top-down methods which start with patterns made on a large scale and reduced in lateral dimensions before forming nanostructures, and bottom-up methods which begin with atoms or molecules to build up nanostructures. The main micromachining techniques based on top-down and bottom-up methods are summarized in table 1.1.

Top-down methods

Top-down methods for nanofluidic device fabrication can be subdivided into several categories.

Firstly, in *bulk-machining*, the nanochannel is created by etching trenches in a substrate wafer, or similarly, for *film-machining*, in the film deposited on the substrate. Typically, this can be done by standard photolithography followed by wet or dry etching of the

1.4 Main nanofluidics achievements up-to-date

Technique		Capability			Dimensions
		Nanochannels	Nanoslit	Nanopores	
Top-down	Bulk-machining	Yes ^{13;14}	Yes ^{15;16}	Yes ^{17;18;19;20}	> 3 nm
	Film-machining	Yes ²¹	Yes ^{5;22}	Yes ²³	> 10 nm
	Surface-machining	Yes ^{24;25;26}	Yes ^{27;28}	Yes ²⁹	> 10 nm
	Mold-machining	Yes ^{30;31;32;33}	Yes ^{34;35}	-	> 75 nm
	Deformation-machining	Yes ³⁶	-	-	> 400 nm
	Integrating existing membranes	-	-	Yes ^{37;38}	> 30 nm
Bottom-up	Biological nanopore	-	-	Yes ³⁹	> 1.4 nm
	Nanotubes	Yes ^{40;41}	-	Yes ⁴²	> 2.5 nm

Table 1.1: Overview of the techniques widely used in the fabrication of nanofluidic devices.

substrate or the deposited film. A secondary wafer is then bonded to the first one to close the fluidic system. The main advantages of the bulk- and film-machining techniques are the possibility to design well-controlled, large area structures suitable for mass production. However, lithographic methods are often expensive.

In *surface-machining*, first a bottom layer is deposited on the wafer, followed by the deposition of the sacrificial layer and its patterning. Then the top layer is deposited on top of the sacrificial layer and patterned. The nanochannel is then formed after etching the sacrificial layer. The strength of this technique is that it is relatively easy to fabricate. However, the etching time may be very long, special irrigation holes have to be designed, and the channel lengths are limited.

In *mold-machining*, first the inverse shape of the desired structure is fabricated. This shape is then filled with a structural material and the mold can be etched or removed to obtain the desired structure. Mold-machining is mainly performed by soft- or nano-imprint lithography. The advantage of this technique is that it is cheap and the structures are relatively easy to replicate. However, the fabrication of the mold is expensive and a new mold is needed for every change of design.

Deformation-machining is an exotic but interesting method based on reducing the channel dimensions by heating the system while applying a uniaxial tensile force. This technique, derived from the well-known optical fiber draw method, has several advantages such as low cost and is rapid to fabricate, however, it is limited to some plastics. Moreover, the channel dimensions are extremely difficult to guarantee and to replicate.

1. INTRODUCTION

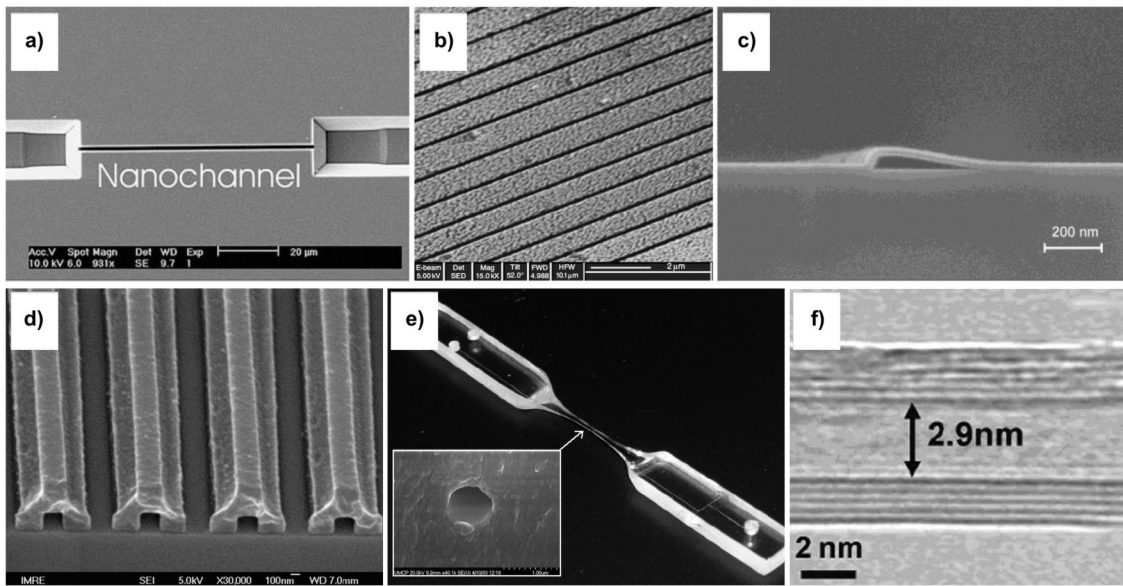


Figure 1.6: Scanning electron microscope images of 2D nanochannels fabricated by a) bulk-machining¹³ (top view), b) film-machining²¹ (top view), c) surface-machining²⁴ (cross-section), d) mold-machining³⁰ (cross-section), e) deformation-machining³⁶ (global system and cross-section) and f) using carbon nanotubes⁴³ (cross-section).

Finally, the integration of existing synthetic nanoporous membranes, which was the first way to perform nanofluidics decades ago, is still used by some research groups. The strength of this method is mainly its cost and its simplicity to produce. However, the size of the nanopores is distributed over a large range of dimensions and their direction can be quite random.

Bottom-up methods

In bottom-up methods, the atoms and molecules are assembled into small nanostructures by controlled chemical reactions, which make these techniques cheaper than conventional lithographic methods.

Nanofluidic devices based on biologic ion-channel nanopores as well as carbon nanotubes (CNT) with an inner diameter from 1.4 to 4.6 nm were reported in the nanofluidics literature. These devices are primarily used for their naturally, well-defined structures. However, the nanostructures are randomly positioned unless they are combined with top-down methods, thus making them very difficult to use.

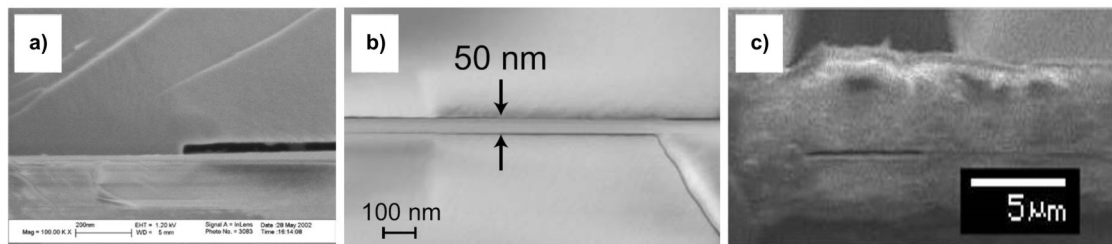


Figure 1.7: Scanning electron microscope images of nanoslits (cross-sections) fabricated by a) bulk-machining¹⁵, b) film-machining⁵ and c) surface-machining²⁷.

Examples of microfabricated nanofluidic devices

2D nanochannels are defined as channels having two of their dimensions in the nanometer range, whereas 1D nanochannels have only one. As presented in figure 1.6, 2D nanochannels based on bulk and film-machining, using deep reactive ion etching (DRIE)¹³, electron-beam lithography (EBL)¹⁴ and focused ion beam (FIB) lithography²¹, were fabricated. Using surface-machining, Tas *et al.* and Nichols *et al.*⁴⁴ have reported different methods based on wet-etching and etching of sacrificial strip, creating 2D nanochannels down to 20 nm²⁴. Han *et al.*²⁶ and Lee *et al.*²⁵ even fabricated 10 nm high nanochannels using DRIE. Mold-machining was also a successful technique to fabricate 2D nanochannels, as shown by Dumond *et al.*³⁰, Guo *et al.*³² and Ilic *et al.*³³. However, the minimum dimensions reached using this technique are still high for some nanofluidic applications (> 75 nm). A very interesting concept of mold-machining to fabricate tunable elastomeric 2D nanochannels was presented by Huh *et al.*³¹; they were able to tune the nanochannel dimensions by applying an external force on the elastomeric material closing the channel, which facilitate sieving and trapping of nanoparticles. Another simple method for fabricating 2D nanochannels based on thermomechanical deformation of rigid polymer substrates was demonstrated by Sivanesan *et al.*³⁶, but the channel sizes are still very large (> 400 nm). Finally, 2D nanochannels based on carbon nanotubes were realised by Mattia *et al.*⁴³, demonstrating the possibility to create extremely small and well-defined channels using bottom-up methods.

As presented in figure 1.7, 1D nanochannels (or nanoslits) were also fabricated using similar methods. However, instead of expensive lithography techniques, Haneveld *et al.*¹⁵ and Mao *et al.*¹⁶ demonstrate the possibility of creating 20 nm high nanoslits by wet etching and DRIE techniques. Using film-machining, Schoch *et al.*^{5;22} structured a pre-deposited 50 nm thick layer of amorphous silicon which was used as a spacer

1. INTRODUCTION

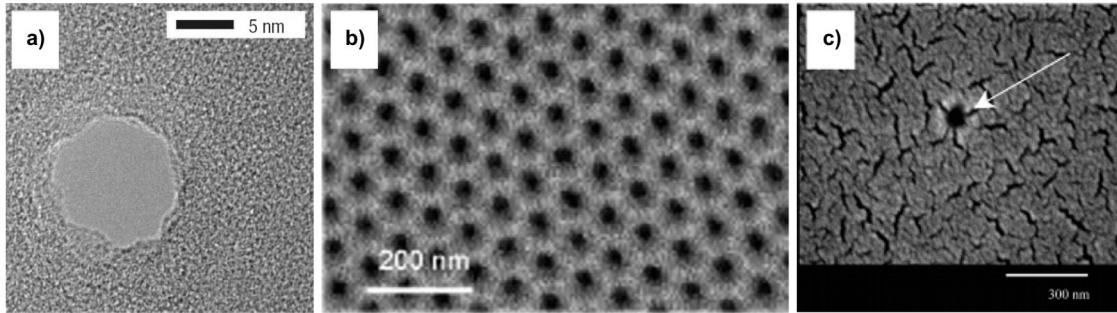


Figure 1.8: Scanning electron microscope images of nanopores (cross-sections) fabricated by a) bulk-machining¹⁷, b) film-machining²³ and c) surface-machining³⁷.

in order to define the height of the 1D nanochannel. Based on surface-machining, Eijkel and Sparreboom *et al.*^{27;28} have fabricated 50 nm high nanoslits by removing a sacrificial layer by wet etching. Finally, 200 nm high nanoslits were also created using mold-machining, as presented by Wang *et al.*³⁴ and Peng *et al.*³⁵.

Figure 1.8 presents some of the different methods to create nanopores. First, bulk- and film-machining of nanopores with a diameter larger than 3 nm have also been performed using wet etching¹⁹, EBL¹⁷, FIB^{18;20} and aluminium anodization²³. Takmakov *et al.*²⁹ presented a surface-machining method based on hydrothermal treatment of anodized alumina membranes. They obtained pores shrinking down to 10 nm in diameter. As described by Harrell *et al.*³⁷, another method consists in isolating nanopores of membranes obtained from commercial sources. In this case, they were able to prepare a membrane sample containing single nanopores with diameters as small as 30 nm. Finally, single carbon nanotubes have been integrated in an epoxy matrix by Sun and Crooks⁴² and used as Coulter counter. Biological pores have also been successfully used, as demonstrated by Kasianowicz *et al.*⁴⁵ who integrated a 2.6 nm diameter α -hemolysin ion channel in a lipid bilayer membrane.

1.4.2 Sensing, sequencing and actuation using nanofluidic structures

Once the nanofluidic devices were successfully fabricated, emphasis was put on sensing and manipulating biomolecules using the unique properties of the nanofluidic structures.

For sensing, two main types of detection methods were commonly integrated in nanofluidic systems: fluorescent and electrical detections. Optical approaches are straightforward and provide direct visual proof. Concerning industrial applications, however, electrical detection is inexpensive, does not require fluorescent dyes and is therefore

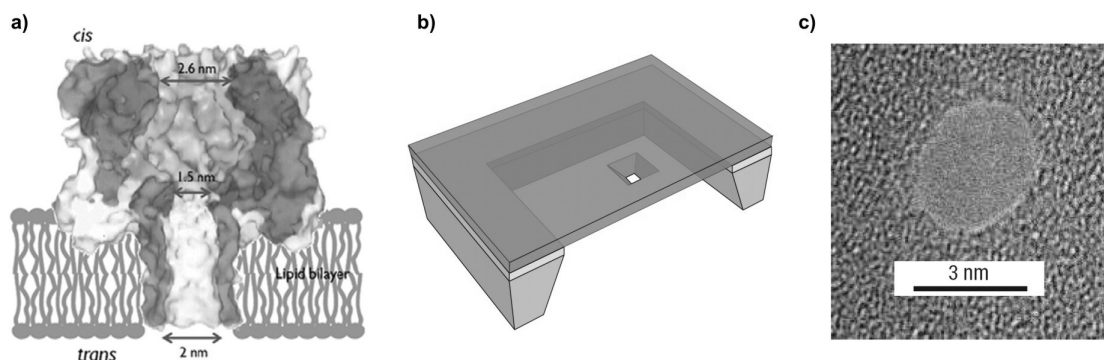


Figure 1.9: Nanopore-based single-molecule analysis: (a) the three-dimensional crystal structure of an α -hemolysin protein nanopore, (b) 3D illustration of a microfabricated nanopore and (c) Transmission electron microscopy (TEM) drilling and image of a nanopore with a diameter of 3 nm. Adapted from Dekker³⁹.

favorable. However, in most of the following reported techniques, both detections were used in order to cross check the validity of both kinds of measurements.

Recent studies have demonstrated that a nanopore can act as a single-molecule sensor. For example, Kasianowicz *et al.*⁴⁵ have successfully characterized the transport of single strands of RNA and DNA across an α -hemolysin protein nanopore (α -hemolysin is the protein illustrated in figure 1.9a, which is secreted by the bacterium *Staphylococcus*). However, it is not possible to control the pore diameter or to use it over a wide range of pH, salt concentration, temperature and mechanical stress. An alternative to protein nanopores is the use of solid-state nanopores, which can be tuned in size with nanometer precision and allow better mechanical, chemical and electrical stability (figure 1.9b and c). Usually, the analysis of translocation events is performed electrically by measuring the changes in ionic conductivity. Molecules are driven through a nanopore by an electric field, and physically block the nanopore. This produces a temporal change in current^{46;47;48;49}. Several research groups have used this principle to detect binding between biomolecules, such as antibody-antigen⁵⁰ or antibody-virus interactions⁵¹. Iqbal *et al.* have even demonstrated the possibility to make the nanopore DNA selective by precoating it with hair-pin loop DNA⁵².

Individual carbon nanotubes have also been used as nanopores. Fan *et al.* have integrated inorganic nanotubes with microfluidic systems to create nanofluidic devices for single DNA molecule sensing⁵³. Bournalon *et al.* have demonstrated the possibility to measure the ionic solution flow inside the carbon nanotube by sensing its change in electrostatic potential⁵⁴. However, manipulation of single carbon nanotubes is still tricky, and will probably stay a research-oriented nanofluidic solution.

1. INTRODUCTION

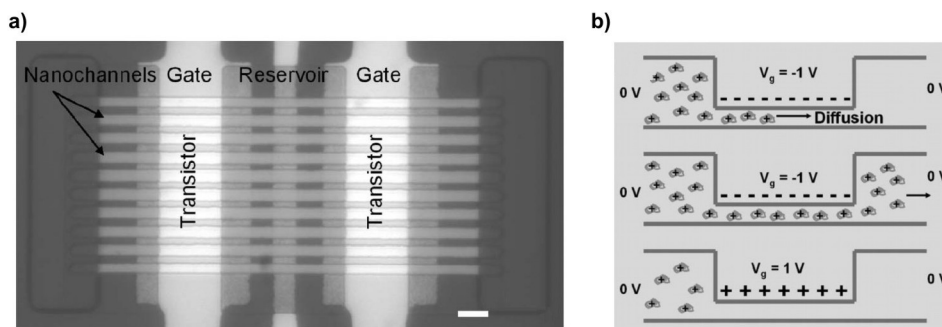


Figure 1.10: Nanofluidic transistor. (a) Micrograph of the fabricated device, with $20\ \mu\text{m}$ long channels (white scale bar is $10\ \mu\text{m}$). (b) Effect of the gate voltage showing the diffusion of avidin proteins when the transistor is turned on or off. Adapted from Karnik *et al.*⁵⁵

Karnik *et al.* have presented a nanofluidic transistor where the electrodes are in direct contact with the solution in the nanochannels⁵⁵ (figure 1.10). They controlled the protein transport through the confinement using electrostatic fields with gate voltages of ± 1 V. Wang *et al.* have reused this concept of nanofluidic field-effect transistor for glucose sensing⁵⁶ and Im *et al.* have demonstrated the possibility to detect the binding between streptavidin and biotin⁵⁷ in such systems, leading to potential immunological applications.

Nanofluidic diodes have also been developed by Vlasiouk *et al.* and Karnik *et al.* Based on single asymmetric nanopores whose surfaces were patterned so that half the nanochannel was positively charged and the other half negatively charged, they demonstrated an analogous principle of operation to that of a bipolar semiconductor diode^{58;59}. This kind of nanofluidic diodes may find applications in control of pH, ionic concentrations, and separation processes in the future.

Another interesting nanofluidic device was proposed by Yi *et al.* They fabricated nanogap capacitors and successfully detected the presence of single stranded DNA in solution, which changes the capacitance value⁶⁰. On a similar principle, Schoch *et al.* and Karnik *et al.* demonstrated the possibility to detect biomolecules and their reaction kinetics with target molecules on surfaces by reading the change of conductivity of the nanochannels^{61;62}.

Nanofluidic structures also present an advantage in fluorescence microscopy in the sense that the measurement volume is restricted to the geometry of the nanochannel. Thanks to the high surface-to-volume ratio, microscopy in nanochannels allows single molecule detection^{11;63} and biomolecules-surfaces interactions kinetics measurement.

Finally, due to size limitations, standard pumping or valving cannot be easily adapted to micro or nanoscale fluidic devices. Hence, interesting approaches were proposed and developed. For example, Lopez, *et al.*⁶⁴ developed a method for forming a stimuli responsive polymer that can be mounted in a nanoporous platform for sensing and actuation. By changing the environment conditions surrounding the valve, such as temperature, pH, ionic strength, intensity or frequency of light, it causes the responsive polymers to shrink in size in such a way that openings are formed which allow liquid flow around them. Once the environmental conditions are reversed to the original state, the actuator goes back to its original size and the nanovalve closes. This principle can be used as an inexpensive pumping method.

1.4.3 Separation and preconcentration using nanofluidic structures

Another important area of application for nanofluidics is separation science. In standard separation science techniques, nanometer-sized apertures are widely employed. For example nanoporous materials are used for size exclusion chromatography, nanoporous gels for DNA separation and nanoporous silica packings for high performance liquid chromatography (HPLC). The problem of these systems is the randomness of the nanostructuring and the spatial averaging. By using well-defined gel-free nanostructures, it is possible to improve the yield and the effectiveness of these techniques. Several groups developed a nanofluidic trap for separation of DNA molecules based on the size of nucleic acids^{67;68;8;69;70}. This nanofluidic trap consists of alternating restricted areas to constrain the flow, and large regions to allow molecules to relax for efficient separation in the thin regions. The restricted areas have to be significantly smaller than the size of the molecule to be sieved⁷¹. As presented in figure 1.11, Fu and Schoch *et al.* demonstrated a continuous-flow anisotropic nanofilter array (ANA) system, where DNA and proteins are separated using different sieving mechanisms including Ogston sieving, entropic trapping and electrostatic sieving⁷².

A solid-state DNA sequencing device was developed for rapid, high-resolution separation of single-stranded DNA ladder bands using a nanofabricated separation matrix⁷³. The separation matrix consists of a number of pillars separated by a distance of 10 to 30 nm. Lopez *et al.*⁷⁴ patented a nanofluidic separation matrix containing an array of nanostructures that provide a gradient of size in at least one direction of the plane. Figure 1.12 illustrates this principle of gradient nanostructures at the interface between micro and nanofluidics^{75;76}. High throughput is another very important point in the development of devices for bio-separation. Lee *et al.*⁷⁷ developed a nanofluidic

1. INTRODUCTION

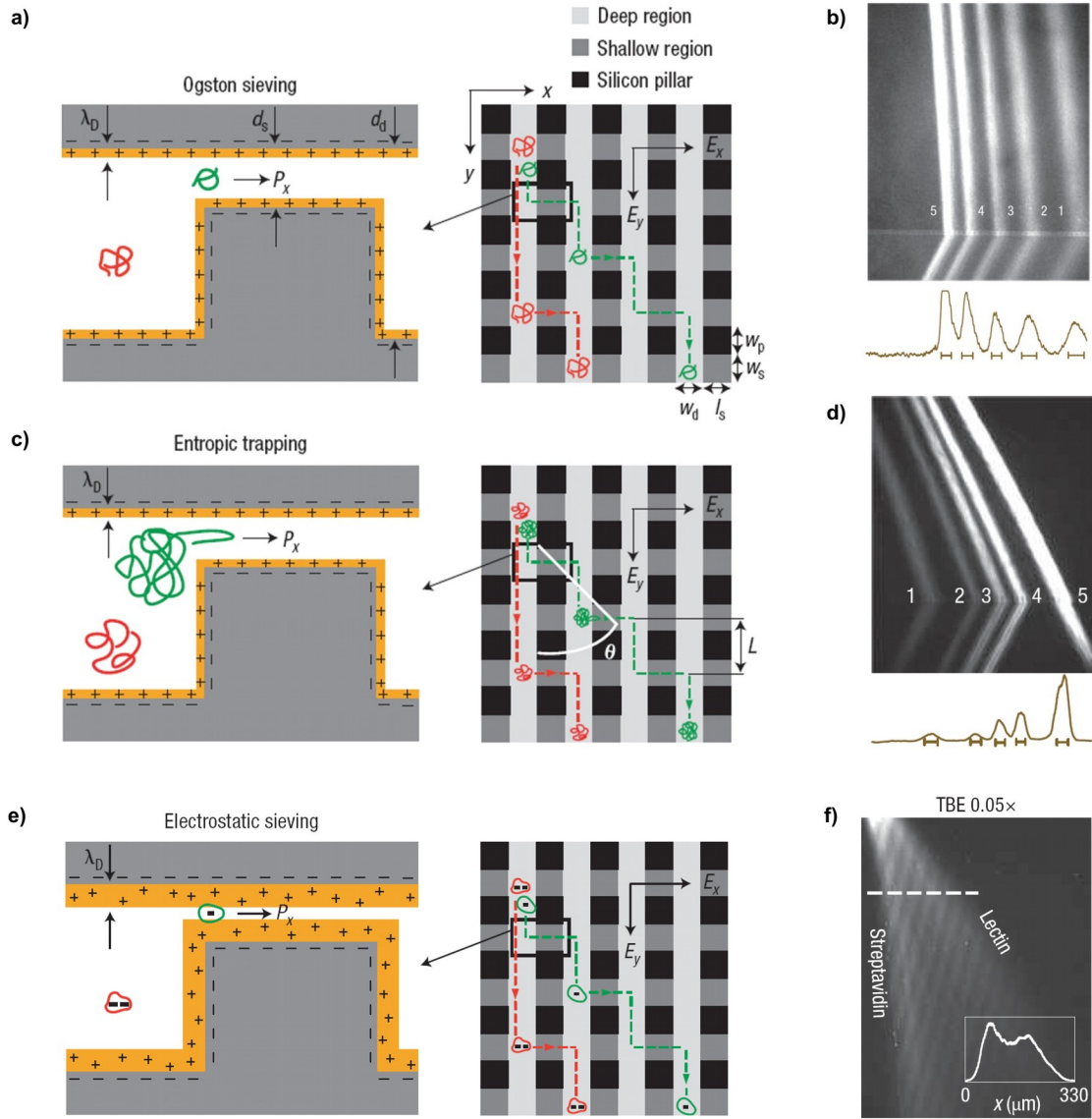


Figure 1.11: Schematics and fluorescence photographs showing negatively charged DNA molecules assuming bidirectional motion in the anisotropic nanofilter array (ANA) under influence of two orthogonal electric fields E_x and E_y . a) Ogston sieving applies for molecules smaller than the nanofiler gap size. b) Measurements of the Ogston sieving for DNA fragments of 50 bp (1), 150 bp (2), 300 bp (3), 500 bp (4) and 766 bp (5). c) Entropic trapping applies for long polyelectrolytes, when the radius of gyration is larger than the nanochannel gap size. d) Measurements of the entropic trapping for long DNA fragments of 2,322 bp (1), 4,361 bp (2), 6,557 bp (3), 9,416 bp (4) and 23,130 bp (5). e) Electrostatic sieving applies when the Debye length is comparable to the nanochannel gap size, rendering the transport charge-selective. f) Measurements of the electrostatic sieving showing the separation of lectin and streptavidin. Adapted from Fu and Schoch *et al.*⁷²

1.4 Main nanofluidics achievements up-to-date

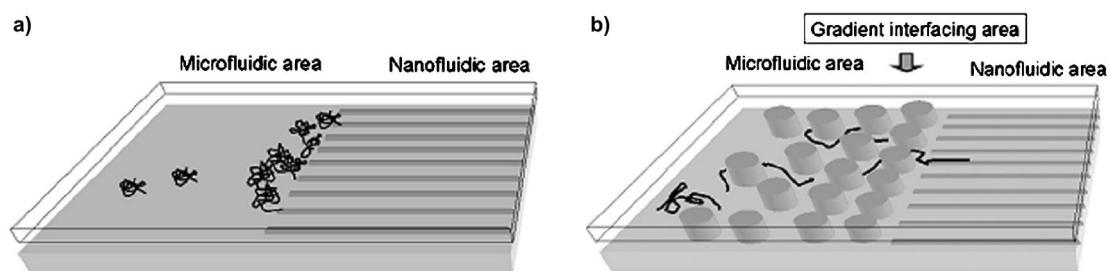


Figure 1.12: Schematic diagrams showing the principle of gradient nanostructures for interfacing micro and nanofluidics. a) When long DNA are drawn by hydrodynamic flow or electric field from a high-entropy area to confining nanochannels, the molecules tend to stick at the entrances of the channels. b) The interfacing region of fluidic structures with gradient dimensions pre-stretches DNA molecules and thus make them enter easily the nanochannels. Adapted from Cao *et al.*⁷⁶

platform for ultra fast sequencing of DNA and RNA molecules. Their device consists of nanometer gaps for the passage of a single DNA strand where lateral nanoelectrodes measure a gated tunneling current. It has the potential to perform DNA sequencing at a rate of about 1 million bases per second per nanogap.

One of the fundamental problems in biomedical diagnostics is that target proteins (or biomarkers) are generally not concentrated enough in initial solutions, such as blood, saliva or urine for a direct detection. The lack of effective molecular amplification strategies, such as polymerase chain reaction (PCR), is an important bottleneck in protein biosensing. An interesting strategy to address this issue is to preconcentrate on-chip proteins in small sample volumes in order to produce higher concentrations. Thus, nanochannels have been demonstrated as an effective protein preconcentration tool. As presented in figure 1.13, Schoch *et al.* have measured the concentration of recombinant green fluorescent proteins (rGFP) in a microchannel using the permselectivity of a nanochannel⁵. They applied an electric field (10 V) across a nanochannel in order to transport the charged proteins from one microchannel to another. However, due to environmental conditions that will be extensively discussed in the next chapter, the exclusion effect prevents the proteins from entering the channel and a preconcentration effect is obtained.

Wang *et al.* characterized a similar preconcentration nanofluidic device^{10;78}. They electrokinetically trapped and collected million-fold concentrated proteins, and showed the possibility to use this "plug" of concentrated species in further analysis, such as immunological reactions. As shown in figure 1.14, they obtained a highly efficient and flexible way to enhance immunoassay detection sensitivity and binding kinetics within

1. INTRODUCTION

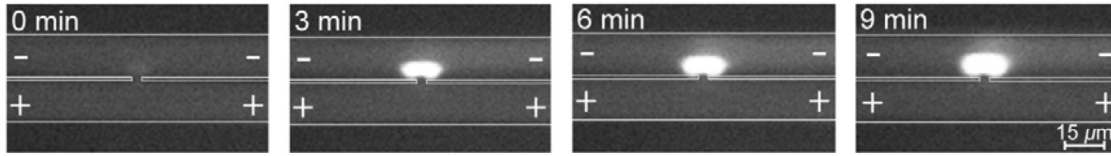


Figure 1.13: Preconcentration of recombinant green fluorescent proteins (rGFP) in the cathodic microchannel in front of a 50 nm height nanochannel. The preconcentration zone (in white) increases in size and concentration over time (illustrated for 0, 3, 6 and 9 min at 10 V). Adapted from Schoch *et al.*⁵

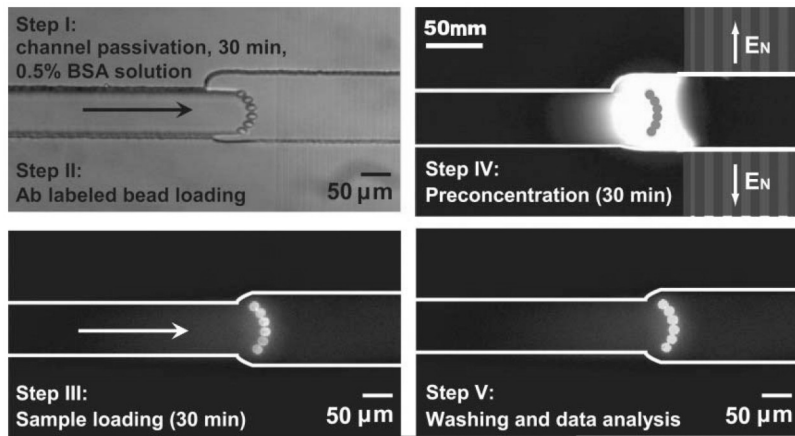


Figure 1.14: Nanofluidic preconcentration device. Illustrations show beads loading, proteins preconcentration and immunosensing procedures. Adapted from Wang *et al.*⁷⁹

30 minutes. Such devices can be used to address the most critical detection issues in the detection of common disease biomarkers⁷⁹.

Models for predicting the preconcentration rates and dynamics were given by Plecis *et al.*⁸⁰. They studied the competition between the electroosmotic dragging force and the highly nonlinear electrophoretic forces induced by the polarization effect. They highlighted different preconcentration regimes suggesting that the mobility and the valence of the species of interest are the most important parameters in the determination of the preconcentration rates.

Concentration of proteins were also performed using porous silica membranes^{81;82}. In this case, as for Ogston sieving, the exclusion of fluorescently labeled ovalbumin from nanopores was obtained because of their size which was larger than the pores size. They used preconcentration in order to increase sensitivity when performing on-chip capillary electrophoresis (CE) and chromatography.

Finally, Kim *et al.* presented an interesting device composed of functionalized micro-

tubules in nanofluidic technologies⁸³, in which they preconcentrated up to 5 orders of magnitude the target molecules in order to strongly reduce the analysis time.

1.5 Motivation and scope of this thesis

It is a fact: the continuous growth of miniaturized electronics related to advances in microfabrication technology and combined with recent advances in molecular biology, has led to the development of highly miniaturized micro- and nanofluidic devices for biomedical and biological analysis. As highlighted above, a multitude of functional blocks such as cell or protein sorting, sieving, preconcentrating, manipulating, sequencing and sensing have been developed. For designing such functional devices, there is a clear need to understand biomolecular transport at this scale, and until now, accurate and simple models describing the diffusion of biomolecules in these confined areas has been missing.

Based on the high surface-to-volume ratio, nanofluidics is the perfect environment to allow for the precise measurement of molecule-surface interactions. Using adequate tools allowing single molecule detection, these surface interactions can be characterized in different environmental conditions. For example, interacting molecules will sometimes be retained and it will affect their diffusion through the nanoconfinement. Obtaining information or even predicting effective and apparent diffusion coefficients is a fundamental aspect in order to model the transport of proteins in future, complex lab-on-a-chip applications.

As an introductory experiment, a rough evaluation of the diffusion coefficient of fluorescently labeled wheat germ agglutinin (WGA) proteins in a nanochannel was obtained by measuring the broadening of the fluorescence intensity of the advancing front. This method does not allow an accurate measurement, but is sufficient to measure the order of magnitude of the diffusion coefficient. As presented in figure 1.15, the comparison between the front profile after 0 and 400 s indicates that the apparent diffusion coefficient is below 10^{-14} m²/s, which is 4 orders of magnitude lower than the value in the bulk reported by Munson, *et al.*⁸⁴ ($D_{WGA,bulk}=7.6\cdot 10^{-11}$ m²/s). In these conditions, the advance of the fluorescent front is mostly limited by the pressure-driven flow that was applied from the external reservoirs and not by the diffusion caused by the concentration gradient.

The strong decrease of the protein diffusion coefficient value is measured in nanofluidics, but still misunderstood. Based on novel experiments, this thesis aims to provide new

1. INTRODUCTION

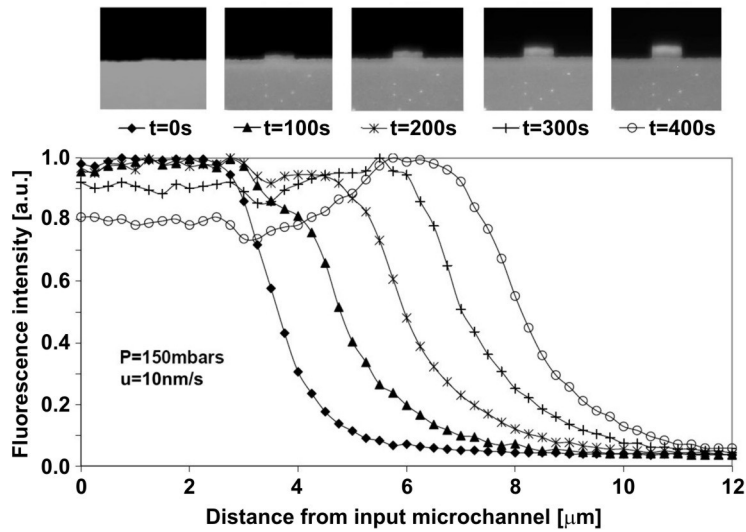


Figure 1.15: 2 μM fluorescently labeled WGA proteins flowing in a 50 nm high nanochannel (pressure-driven flow conditions). The solution is composed of 10 mM KCl in de-ionized water (pH=7). The pushing pressure is 150 mbar and the flow linear speed (advance of the fluorescent front) in the nanochannel is about 10 nm/s.

theoretical models for the prediction of the mass transport of biomolecules in nanoconfinements, and thus will provide a potential explanation for the strong decrease in the diffusion coefficient.

The goals of this thesis can be summarized as:

- to select and improve an existing nanofluidic fabrication and manipulation technology;
- to elaborate novel theoretical models describing the passive transport behavior in these conditions;
- to study and characterize the biomolecules-surfaces interactions;
- to measure the hindered transport of single proteins in a nanochannel in different environmental conditions;

Transport phenomena governing the movements of biomolecules in nanofluidics will be electrically and optically investigated in order to bring a deeper understanding at the fundamental level.

1.6 Thesis structure

Apart from this introductory chapter presenting the context and the main findings in nanofluidics, the thesis includes 6 chapters.

Chapter 2 will provide the fundamental theory to understand the following work. I will introduce the main forces acting in nanofluidics and will provide equations describing the fluid dynamics at the nanoscale. The diffusion of biomolecules in concentrated solutions will also be discussed as well as electrostatic phenomena occurring in liquids. Then I will go on with a general description of biomolecules in solutions, and the assumptions made in order to simplify theoretical models.

Chapter 3 is dedicated to practical matters. I will present microfabrication steps and the experimental setup interfacing with fluid, optical and electric control equipment. The different nanofluidic devices I manufactured will also be mechanically and electrically characterized.

In chapter 4, I will supply a theoretical model describing the concentration of proteins inside nanoconfinements, taking into account the steric exclusion, the presence of reversibly adsorbed molecules on surfaces and the exclusion-enrichment effect. Then, the electrical detection and characterization of protein-surface interaction will be performed. The measurement of proteins detected with a response time in the minute range and their kinetic parameters for the adsorption and desorption over a wide range of pH and at different ionic concentrations will be discussed.

In chapter 5, based on single molecule detection experiments using fluorescence correlation spectroscopy (FCS), I will measure the effective diffusion coefficient and demonstrate the different diffusion regimes governed by the solution characteristics (*i.e.* ionic strength, pH, charge and concentration of proteins).

Chapter 6 will introduce a novel method to measure the apparent diffusion coefficient of fluorescently labeled molecules. To begin, I will discuss why it is interesting to measure the apparent diffusion of biomolecules, and the concept of steady-state dispersion upon which I have elaborated. I will conclude this chapter by demonstrating the possibility to detect the complex formation of proteins using nanofluidic devices.

Finally the results and findings are summarized in chapter 7, and I will conclude this work with recommendations for future developments and applications.

1. INTRODUCTION

CHAPTER

2

TRANSPORT PHENOMENA IN NANOFLUIDICS

This chapter presents the governing principles behind nanofluidics that will be used during this thesis. First, forces such as solvation, fluctuations, Van der Waals, and electrostatic, which are strongly acting at the nanoscale will be described. I will also discuss the theory of nanoconfined fluid dynamics and the molecular diffusion in concentrated solutions. Subsequently, electrokinetic phenomena, such as surface charge density, potential distribution and electrical double layer, which are important concepts in nanofluidics, will be described. Finally, the characteristic parameters of biomolecules in function of their surrounding fluidic conditions will be discussed, as well as assumptions made in order to simplify further theoretical models.

2. TRANSPORT PHENOMENA IN NANOFUIDICS

2.1 Forces in nanofluidics

As the dimensions shrink, the physical scaling laws impose different descriptions and approximations. For example, when reducing the size of a particle in a liquid solution, the force due to the earth's gravity, which is dominant at the human scale, will become insignificant at the nanoscale in comparison to others, such as electrostatic forces.

Several forces are acting in nanofluidics and the most important are sketched in figure 2.1 and listed in table 2.1. Curves were calculated using the following values: the interaction surface $S=5 \cdot 10^{-7} \text{ m}^2$, the Boltzmann constant $k_B=1.38 \cdot 10^{-23} \text{ J/K}$, the temperature $T=300 \text{ K}$, the spacing between attachment sites $s=8.5 \text{ nm}$, the brush thicknesses $L=22.5 \text{ nm}$, the Hamaker constant $C_H=2.2 \cdot 10^{-20} \text{ J}$, a viscosity $\eta=0.001 \text{ Pa}\cdot\text{s}$, a flow velocity $u=1 \mu\text{m/s}$, a density $\rho=1000 \text{ kg/m}^3$ and a gravity acceleration $g=9.81 \text{ m/s}^2$.

Forces	Typical equation	Scaling	Reference
Solvation	DLVO theory	$F \propto \exp(a-b \cdot l)$	Henderson ⁸⁵
Fluctuation	$F \approx \frac{SkT}{s^3} \exp\left(-\frac{\pi l}{L}\right)$	$F \propto \exp(-a \cdot l)$	De Gennes ⁸⁶
Van der Waals	$F = -\frac{C_H R}{6l^2}$	$F \propto l^{-2}$	Israelachvili ⁸⁷
Electrostatic	$F = \varepsilon_0 \varepsilon_r R \Psi_1 \Psi_2 \cdot \ln\left(1 + \exp\left(-\frac{l}{\lambda_D}\right)\right)$	$F \propto \exp(a-b \cdot l)$	Israelachvili ⁸⁷
Stokes drag	$F = 6\pi\eta u r_p$	$F \propto l^1$	Batchelor ⁸⁸
Gravity	$F = \frac{4}{3}\pi\rho g r_p^3$	$F \propto l^3$	Newton

Table 2.1: Main forces acting in nanofluidics and their scaling in function of the characteristic length of the system.

Solvation forces

The origin and nature of the solvation forces, also called hydration forces, has long been controversial, especially in the colloidal and biological literature. Repulsive hydration forces appear to arise whenever water molecules strongly bind to surfaces containing hydrophilic groups (as this is the case for glass used in this thesis), and their strength depends on the energy needed to disrupt the hydrogen-bonding network and to dehydrate two surfaces as they approach each other⁸⁹. Henderson, *et al.*⁸⁵ proposed an adaptation of the DVLO (named after the scientists Derjaguin, Landau, Verwey and Overbeek) theory for describing the solvation forces, and Israelachvili, *et al.*⁸⁷ successfully measured solvation forces between two curved mica surfaces of radii $R=1 \text{ cm}$ in

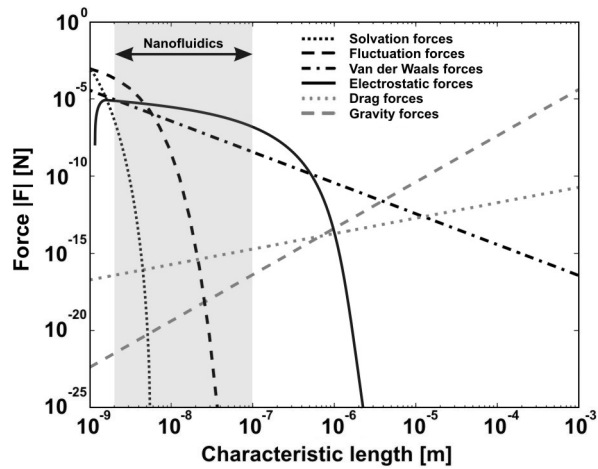


Figure 2.1: Scaling of main forces acting in nanofluidics in function of the characteristic length of the system (particle radius r_p or distance l between two parallel planes). The grey zone represents the area of interest in nanofluidics.

10^{-3} M KCl. As reported in figure 2.2, they measured short-range oscillatory solvation forces arising when surface distances were smaller than 2 nm. Solvation forces are very strongly attractive in channels smaller than 1 nm, but decay exponentially very quickly when increasing channel dimension and can thus be neglected in the scope of this thesis.

Fluctuation forces

When two surfaces covered by polymers or biomolecules such as proteins approach each other in a liquid solution, they experience a force once the polymer layers begin to overlap. This interaction, also called steric repulsion, usually leads to a repulsive osmotic force due to the unfavorable entropy associated with the confinement between the surfaces. Taunton, *et al.*⁹⁰ have measured the repulsive force between two polystyrene brush layers disposed onto mica surfaces in toluene and a theoretical model has been proposed by de Gennes, *et al.*⁸⁶. The fluctuation forces are also decaying exponentially and their effect could become important in nanofluidics if the size of the channel is in the same order as the size of the adsorbed molecules.

Van der Waals forces

Van der Waals forces are attractive forces between molecules or between a molecule and a surface, and are also repulsive interactions that prevent the complete collapse of matter to nuclear densities. They are a consequence of quantum dynamics because they are caused by correlations in the fluctuating polarization of molecules. In this

2. TRANSPORT PHENOMENA IN NANOFUIDICS

section, Van der Waals forces are considered as attractive forces between a particle and a surface. Israelachvili, *et al.*⁸⁷ have successfully measured attractive Van der Waals forces for two curved mica surfaces at a distance l . They proposed a model based on the Hamaker constant C_H and they showed that Van der Waals forces decay with l^2 . These forces can still be considered as short-range interactions.

Electrostatic forces

When an uncharged surface is in contact with an aqueous solution, the dissolution of the surface as well as the adsorption of charged molecules present in the solution may charge the surface positively or negatively. This phenomenon leads to the apparition of an electrical double layer (EDL) that will be introduced in section 2.4.2. Here, the electrostatic forces between a particle and a surface may be strongly attractive or repulsive, depending on the charges of the particle, those of the surface, and of the ionic concentration of the solution. Israelachvili, *et al.*⁸⁷ were able to measure repulsive electrostatic forces for two curved mica surfaces at a distance l . They also proposed a theoretical model which shows that electrostatic forces roughly decay exponentially with l . The electrostatic forces are the stronger forces acting in nanofluidics, and thus electrostatic interactions between charged surfaces and diffusing biomolecules will be deeply studied in chapter 5.

Other forces

The Stokes drag force depends directly on the velocity of the particles and of the effective viscosity of the solution. This force is acting to slow down the diffusion movement of the molecules and will be used in section 2.3 to determine the diffusion coefficient. In micro and nanofluidics, the force due to the earth's gravity is largely too small to influence the molecules. I also do not introduce electrophoretic and magnetic forces as no electric or magnetic fields were applied in the experiments performed in this thesis, but if their intensity is strong enough, they can become important forces in nanofluidics.

2.2 Fluid dynamics at nanoscale

By definition, fluids are composed of molecules that collide with one another and solid objects as surfaces. In this work, fluids are assumed to obey the continuum assumption, but one major effect that cannot be ignored by the continuum description is the ordering of molecules close to the solid walls. In bulk liquids, the molecules do not order spatially

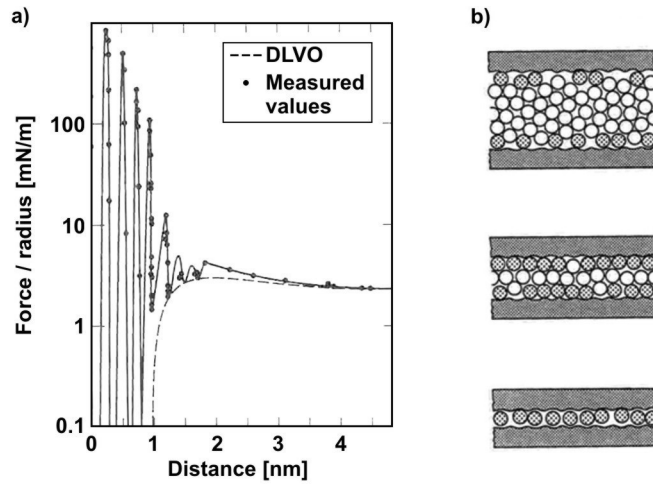


Figure 2.2: (a) Measured short-range force between two curved mica surfaces in 10^{-3} M KCl. The dashed line shows the expected DLVO interaction. (b) Schematic of how real structures, possessing crystalline structure, force the liquid molecules between them to adopt lateral, solid-like ordering commensurate with the atomic corrugations of the surfaces. This ordering is in addition to the layering, which occurs even between smooth unstructured surfaces. Adapted from Israelachvili⁸⁷.

like in a solid crystal, however, close to a solid wall or in very narrow nanoconfinements, the molecules often assume a partially ordered structure, as demonstrated by Zangi *et al.*⁹¹ using molecular dynamics (MD) simulations. The ordering leads to density oscillations in the liquid as measured by Israelachvili⁸⁷ and reported in figure 2.2. The dashed line represents the equation DLVO. These oscillations extend only a few nanometers away from the wall, suggesting that on length scales of about 3 nm they are already negligible. Then, the question arises: how well are the results of continuum theory reproduced on a larger length scale. The pressure-driven flow of simple liquids in nanochannels has been studied by means of MD simulations and compared to the Poiseuille flow profile⁹². It turns out that already in channels of a height of 8 nm, the MD results reproduce the parabolic flow profile very well, which means that the solutions filling the 50 nm high nanochannels presented in this thesis are also described very well by the continuum theory.

Consequently, properties such as density, pressure, temperature, and velocity are taken to be well-defined at infinitesimally small points, and are assumed to vary continuously from one point to another. The momentum equations for Newtonian fluids are the

2. TRANSPORT PHENOMENA IN NANOFUIDICS

Navier-Stokes equations, which is a non-linear set of differential equations that describe the flow of a fluid whose stress depends linearly on velocity gradients and pressure:

$$\rho \left[\frac{\partial u_c}{\partial t} + u_c \frac{\partial u_c}{\partial z} \right] = \rho F_{ext} - \frac{\partial \Delta P}{\partial x} + \eta \frac{\partial^2 u_c}{\partial z^2} \quad (2.1)$$

where ΔP is the external pressure, u_c the flow velocity, ρ and η the density and viscosity of the fluid and F_{ext} an external force.

2.2.1 Low Reynolds number fluidics

Almost all physical phenomena behave qualitatively differently when the length scale of the system is changed. In fluid mechanics, the Reynolds number is the dimensionless parameter that determines the relative importance of inertia compared to frictional force due to viscosity. It is written as:

$$Re = \frac{h u_c \rho}{\eta} \quad (2.2)$$

where h is a relevant length of the fluidic system. A system is generally considered to be in the laminar flow regime when $Re < 100$, which is always the case in nanofluidics⁹³. For the low Reynolds number regime and assuming no external forces (*i.e.* neglecting electric potentials due to the surface charge and no streaming potential), the equation 2.1 is reduced to:

$$\eta \frac{\partial^2 u_c}{\partial z^2} = \frac{\partial \Delta P}{\partial x} \quad (2.3)$$

As this equation is time-independent, the fluid reacts only to external forces (such as electric fields or hydraulic pressures). Moreover, when the external force is reversed, the fluid motion is also reversed without mixing or irreversible change. This turbulence-free fluidic environment is perfect for manipulating fragile biomolecules such as proteins.

2.2.2 Pressure-driven flow

Fluid in a nanochannel can be moved by the application of a pressure difference ΔP in the x -direction across the channel. A solution to equation 2.3 with the boundary conditions $u_c(z = \pm h/2) = 0$, is given by the Hagen-Poiseuille equation with a parabolic velocity distribution in z :

$$u_c(z) = \frac{1}{2\eta} \frac{\partial \Delta P}{\partial x} \left[z^2 - \left(\frac{h}{2} \right)^2 \right] \quad (2.4)$$

As the 1D nanochannels fabricated in this thesis have the smallest dimension in the height direction, the parabolic flow distribution will occur in the z -direction and the flow profile in x -direction will appear to be flat. This phenomenon will be described and widely used in experiments of chapter 6.

The flow resistance of a nanochannel depends on its cross-section and its length l_{nC} . For a rectangular channel of width w_{nC} much larger than the channel height h_{nC} , the flow resistance R_{Φ} can be approximated by:

$$R_{\Phi} = \frac{12\eta l_{nC}}{w_{nC} h_{nC}^3} \quad (2.5)$$

And based on the relation $\Delta P = R_{\Phi} \Phi_m$, (with the mass flow $\Phi_m = u_c w_{nC} h_{nC} \rho$) the pressure drop ΔP along the channel is calculated to be:

$$\Delta P = \frac{12\eta l_{nC} \Phi_m}{w_{nC} h_{nC}^3} \quad (2.6)$$

2.3 Molecular diffusion in liquids

In nanofluidics as well as in micro or macroscale fluidics, the concentration distribution of a solute in a solvent can change in two ways. Firstly, when there is a motion of the fluid, such as the pressure-driven flow, any given small portion of the fluid will move as a whole with unchanged composition. This results in a purely mechanical mixing and the concentration of the solution at any point in space varying with time. If we ignore any processes of thermal conduction and internal friction which may also be taking place, this change in concentration is a thermodynamically reversible process and does not result in energy dissipation.

Secondly, a change in composition can occur by the molecular transfer of the components from one part of the solvent to another. The equalization of the concentration by this direct change of composition of every small portion of fluid is called "diffusion". Diffusion is an irreversible process and is, like thermal conduction, one of the sources of energy dissipation in a mixture of fluids. It occurs in liquids as well as in solids or gases. However, since mass transfer is strongly influenced by molecular spacing, diffusion occurs more readily in gases than in liquids and more in liquids than in solids.

2. TRANSPORT PHENOMENA IN NANOFUIDICS

2.3.1 Brownian motion

Diffusion is caused by random molecular motion of the particles suspended in the fluid, which move in a stochastic manner (called the Brownian motion). This movement finds its origin in the collisions between the solute and the solvent molecules. While its average displacement is zero, the root mean square of the displacement of rigid solute spheres diffusing in a continuum of solvents is $\sqrt{2Dt}$ per degree of freedom, with the diffusion coefficient D which is given by Einstein⁹⁴:

$$D = \frac{k_B T}{f} = \frac{k_B T}{6\pi\eta r_s} \quad (2.7)$$

where k_B is Boltzmann's constant, T the temperature, f the friction coefficient of the solute, η is the solvent viscosity, and r_s the solute radius. Equation 2.7, which is known as the Stokes-Einstein equation, is limited to infinitely dilute solutions. The diffusion coefficient in liquids varies also with solute concentration, frequently up to an order of magnitude. Batchelor⁸⁸ proposed an empirical correction factor, but we can assume equation 2.7 to give an acceptable order of magnitude value. The inverse dependence on the friction factor implies that for a given duration, the smaller the particle, the farther it diffuses. Since the viscosity is related to temperature by $\eta \sim \exp(E_a/RT)$, the diffusivity roughly increases with temperature:

$$D \propto \frac{T}{\exp(E_a/RT)} \quad (2.8)$$

where E_a is activation energy and R the molar gas constant.

The Brownian motion of each individual particle does not follow the diffusion equation 2.7. However, many identical particles, each obeying the same boundary and initial

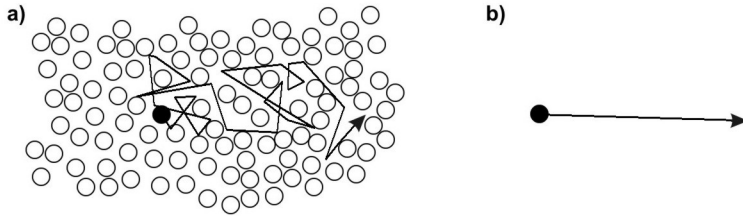


Figure 2.3: Molecular motion in a liquid. (a) Illustration of the real situation of a diffusing solute (in black) following a Brownian trajectory involving many interactions and vacancies. (b) Stokes-Einstein model of a solute sphere in a fluid continuum.

conditions, share some statistical properties regarding their spatial and temporal evolution; the diffusion equation captures these statistical properties. Figure 2.3a illustrates a possible Brownian way of a solute molecule (in black) surrounded by solvent molecules (in white) and figure 2.3b the expected trajectory using the Stokes-Einstein model.

2.3.2 Diffusion in concentrated solutions

Analogous to heat transport, when a spatial solute concentration gradient dc/dx exists in a solvent, the mass transport of the solute is directly influenced by its local concentration. Assuming that diffusion depends mainly on the gradient of concentration and not on temperature, pressure or electric fields, the main equations for mass diffusion are known as Fick's laws and can be written:

$$J = -D \frac{dc}{dx} \quad (2.9)$$

$$\frac{dc}{dt} = D \frac{d^2c}{dx^2} \quad (2.10)$$

Equation 2.9 relates the diffuse flux per unit area J to the concentration field, by postulating that the flux goes from regions of high concentration to regions of low concentration. Equation 2.10 states that after an infinite time $t \rightarrow \infty$, solute molecules will tend to move in order to homogenize the concentration in the domain. This equation was solved by Crank⁹⁵ in an infinite one-dimensional domain for the decay of an initial pulse of M total amount of solute divided by the cross-sectional area A , located in $x=0$ at time $t=0$:

$$c = \frac{M/A}{\sqrt{4\pi Dt}} \exp\left(-\frac{x^2}{4Dt}\right) \quad (2.11)$$

which is a Gaussian function with a variance $2Dt$.

When combining parallel diffusion and convection, for a constant flow velocity u , the mass balance to calculate the concentration profile is simply:

$$\frac{dc}{dt} = D \frac{d^2c}{dx^2} - \frac{dc}{dx} u \quad (2.12)$$

These equations will be used later in chapter 5 in order to verify if the concentration profiles in a nanoconfinement under different pressure conditions similar to those expected by this model.

2.4 Electrostatics in liquids

2.4.1 Surface charge density

The high surface to volume ratio of nanofluidic systems results in the dominance of surface effects on fluidic motion. Most solid surfaces acquire an electric surface charge when brought into contact with aqueous solutions with ions (electrolyte), because the surface chemical group can be protonated or unprotonated depending on the pH of the electrolyte. The nanochannels realized in this thesis were microfabricated in Pyrex substrates, with surfaces terminated by silanol groups (-Si-OH), and consequently are unprotonated at a pH higher than 2.⁹⁶ Therefore, at most pH conditions the nanochannel surfaces contain negative surface charges, and the positive ions in the solution develop a charge-screening layer called Debye layer.

2.4.2 Potential distribution and electrical double layer

In this work, I consider only the single aqueous phase case (*i.e.* the solution that fills the nanoconfinement), in the absence of electrical potential gradients and in which any number of solutes i are dissolved. In response to the surface charge generated at a liquid/solid interface (negative surface potential called zeta potential ζ), nearby ions of opposite charge in the electrolyte are attracted by the electric field produced by surface charge and ions of like charge are repelled. The spontaneous formed surface charge therefore forms a region near the surface called an electrical double layer (EDL) that supports a net excess of mobile ions (in comparison to the bulk) with an opposite polarity to that of the wall. Initially the EDL was described by Helmholtz as a simple capacitor. Although it can be used to derive some important electrokinetic relationships, the EDL has long been recognized as an inadequate representation of the situation. The theory for a diffuse double layer was developed independently by Gouy and by Chapman who treated one layer of charge smeared uniformly over a planar surface immersed in an electrolyte solution⁹⁷. They used the Boltzmann distribution of the i^{th} ion which describes the distribution of ions as a function of the electrical potential $\Psi(z)$:⁹⁸

$$c_i = c_{i0} \cdot \exp \left[-\frac{z_i e \Psi(z)}{k_B T} \right] \quad (2.13)$$

where k_B is the Boltzmann constant, T the temperature, e the electron charge, c_{i0} the ionic concentration away from the surface and z_i the valency of ion i . Since $F c_i = n_i e$

(F is the Faraday constant), equation 2.13 can be expressed in terms of the number density n_i as:

$$n_i = n_{i0} \cdot \exp \left[-\frac{z_i e \Psi(z)}{k_B T} \right] \quad (2.14)$$

Equation 2.14 gives the local concentration of each type of ion in the double layer region, provided that z_i has the correct sign attached to it. To determine the electric potential Ψ , the Poisson equation has to be introduced. The net charge density ρ_e in the EDL for any electrolyte can be written:

$$\rho_e = e \sum_{i=1}^N z_i n_i \quad (2.15)$$

which tends to zero for an electrically neutral bulk. The Poisson equation for the potential associated with the charges on the wall is:

$$\nabla^2 \Psi(z) = -\frac{\rho_e}{\varepsilon_0 \varepsilon_r} \quad (2.16)$$

where ε_0 and ε_r are respectively the permittivity of vacuum and the dielectric constant of the medium (assumed constant). Equation 2.16 is a non-linear differential equation, and although can be solved analytically by substituting equations 2.15, 2.16 and 2.14. The Poisson-Boltzmann equation is obtained:

$$\frac{d^2 \Psi(z)}{dz^2} = -\frac{e}{\varepsilon_0 \varepsilon_r} \sum_{i=1}^N z_{i0} \cdot \exp \left[-\frac{e z_i}{k_B T} \Psi(z) \right] \quad (2.17)$$

The Debye-Hückel approximation for describing the electrical potential in the EDL (called like this because these two workers used the same approximation in their theory) is a solution to the Poisson-Boltzmann equation 2.17 assuming that $(e z_i \Psi(z))/(kT) \ll 1$:

$$\frac{d^2 \Psi(z)}{dz^2} = \frac{\Psi(z)}{\lambda_D^2} \quad (2.18)$$

where λ_D is the Debye length (also called Debye thickness), which is defined as:

$$\lambda_D = \sqrt{\frac{\varepsilon_0 \varepsilon_r k_B T}{e^2 \sum_i n_{i0} z_i^2}} \quad (2.19)$$

2. TRANSPORT PHENOMENA IN NANOFUIDICS

By taking appropriate boundary conditions (when $\Psi(z) \rightarrow \zeta$ then $z \rightarrow 0$, and when $d\Psi(z)/dz=0$ then $z \rightarrow \infty$), the solution to equation 2.18 is:

$$\Psi(z) = \zeta \cdot \exp\left[-\frac{z}{\lambda_D}\right] \quad (2.20)$$

This solution shows the form of the potential distribution near the wall. However, it is based on the approximation $\zeta z_i < 25.7$ mV which is not always valid (as in colloid systems for example).

2.4.3 Electrical double layer in 1D nanochannels

In the last section, based on the simple flat plate model, the electrical potential near the surface was described. However, there is no analytical resolution of the Poisson-Boltzmann equation for two infinite charged plates. When linearizing equation 2.18 for a 1D nanochannel of height h_{nC} , the Debye-Hückel approximation becomes⁹⁸:

$$\Psi(z) = \zeta \frac{\cosh\left(\frac{(h_{nC}/2) - z}{\lambda_D}\right)}{\cosh\left[\frac{h_{nC}}{2\lambda_D}\right]} \quad (2.21)$$

As illustrated in figure 2.4, the counterions electro-migrate to the surface to screen the surface charge and maintain electro-neutrality Ψ_∞ .

In the experiments performed in this thesis, I always used symmetrical $z_i : z_i$ electrolytes (KCl or NaCl). By taking $\epsilon_r=80$ and $T=300$ K, equation 2.19 is reduced to:

$$\lambda_D = \frac{\kappa}{z_i \sqrt{c_i}} \quad (2.22)$$

where $\kappa = 3.04 \cdot 10^{-10} \text{ mol}^{0.5} \text{ m}^{-0.5}$ in these conditions.

At high ionic strength ($c_i=1$ M), the Debye length is calculated to be about 0.3 nm and the nanochannel is mostly composed of anions and cations which compensate each other and guarantee the electro-neutrality. Therefore, at very low buffer concentrations ($c_i=10^{-5}$ M), the Debye layer is 96 nm, which is almost twice the height of the nanochannel design in this work. In such conditions, there is an overlap of the EDL and the channel repulses' negatively charged molecules (depicted in figure 2.4c). The confined fluidic system behaves more and more similarly to a gel with homogeneously distributed fixed charges. The potential distribution remains high inside the nanochannel and never reaches the level that is at a large distance from the surface Ψ_∞ . I will

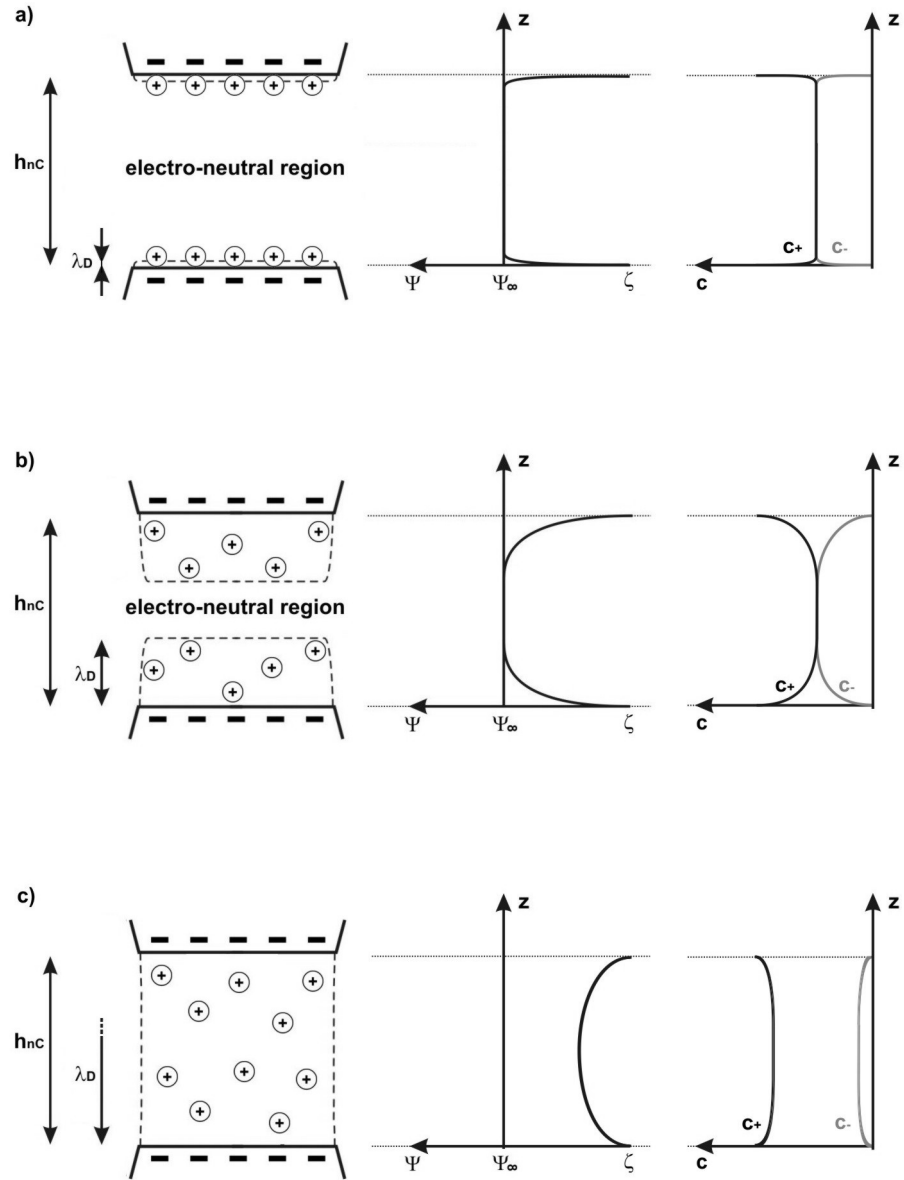


Figure 2.4: Charge screening and electrical double layer thickness (Debye length λ_D) inside a nanochannel of height h_{nC} when filled with (a) a high ionic strength solution, (b) a lower salt concentrated solution and (c) a very low ionic strength solution. When $\lambda_D > h_{nC}/2$, an overlap of the EDL appears (case c). Right to each schematic are plotted the electrical potential $\Psi(z)$ (equation 2.21) and the ions concentration c_z (equation 2.13, cations c_+ are depicted in black and anions c_- in grey).

2. TRANSPORT PHENOMENA IN NANOFUIDICS

discuss these conditions in detail and the way they affect protein diffusion in chapter 5, and I recommend the excellent recent review on the effect of chemical potential on transport in nanofluidics by Eijkel *et al.*⁹⁹.

2.5 Biomolecules and their environment

The previous sections have highlighted physical phenomena resulting from the introduction of fluids in nanofluidic structures. However, in biological and biomedical applications, fluids contain biomolecules, which are defined as biological components produced from a living organism. Table 2.2 summarizes some types of biomolecules that may be used in nanofluidics, and gives an order of magnitude of their size.

In this thesis, the interest goes to globular spherical proteins, which are water soluble and have specific functions in the immune system and metabolism. These proteins are not just randomly coiled chains of amino acids. A variety of intramolecular interactions enable the amino acid chain to fold in a specific way to give proteins a 3D structure and shape. This structure is critical for its activity and function.

Figure 2.5 illustrates the different way to describe the same protein. Case a) shows an all-atoms representation colored by atom type, case b) is the 3D backbone conformation colored by secondary structure and case c) represents the protein as an homogeneous sphere of radius r_s with 8 charges and its electrical double layer λ_D which compensate the charge distribution when the molecule is in aqueous solution. This last simple interpretation will be used for the theoretical models elaborated in this thesis.

Proteins are very sensitive to their chemical and physical environment. Among the earliest known agents affecting protein stability and aggregation are salts¹⁰⁰, acids and

Biomolecules	Size
Water molecule	0.3 nm
Amino acid	0.8 nm
DNA helix diameter	2 nm
Globular protein	4 nm
Ribosome	25 nm
Virus	40-250 nm

Table 2.2: Different size of biomolecules that can be of great interest for nanofluidics.

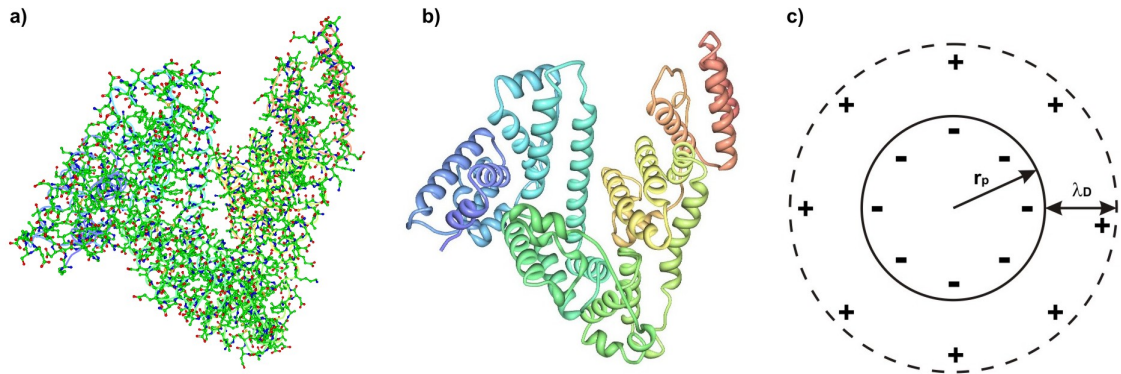


Figure 2.5: Representations of the Serum Albumin protein (from RCSB Protein Data Bank, 1O9X). (a) All-atom representation colored by atom type. (b) 3D backbone conformation, colored by secondary structure. (c) Simplified model showing an homogeneous sphere of radius r_p with $z=8$ charges and its electrical double layer λ_D which compensate the charge distribution (when in solution).

bases¹⁰¹. A change in pH, temperature or ionic strength may disrupt the interactions constituting the structure of the proteins and cause the protein to unfold. This process is called denaturation and change proteins conformation in two different states: one highly unfolded and the other one more compact, sometimes called «the molten globule»¹⁰². The protein loses activity once its normal shape is lost. In some cases, this denaturation is reversible and the protein can renature, although in most cases the activity loss is permanent.

Stigter *et al.*¹⁰² have elaborated a theory based on simple measurements which predict the conditions where proteins begin to denaturate. For example, figure 2.6 shows the folding transitions of myoglobin in aqueous solutions at different temperatures, pH and ionic strengths. Even though the pH range of «working» proteins is still large (from pH=4 to pH=12 at $T=25^\circ\text{C}$), one has to consider that changing pH and ionic strength significantly affects the effective charge and size of the proteins¹⁰³.

2.6 Conclusion

This chapter provided a general overview of some theories describing the transport phenomena in nanofluidics^{5:104}.

Several forces which are negligible at the human scale, but significant in nanofluidics, were introduced and their scaling was discussed. Fluid dynamics at the nanoscale was described, showing that for length scales higher than 3 nm, the continuum regime can be admitted and thus fluid flow in nanochannels is considered as strictly laminar

2. TRANSPORT PHENOMENA IN NANOFLUIDICS

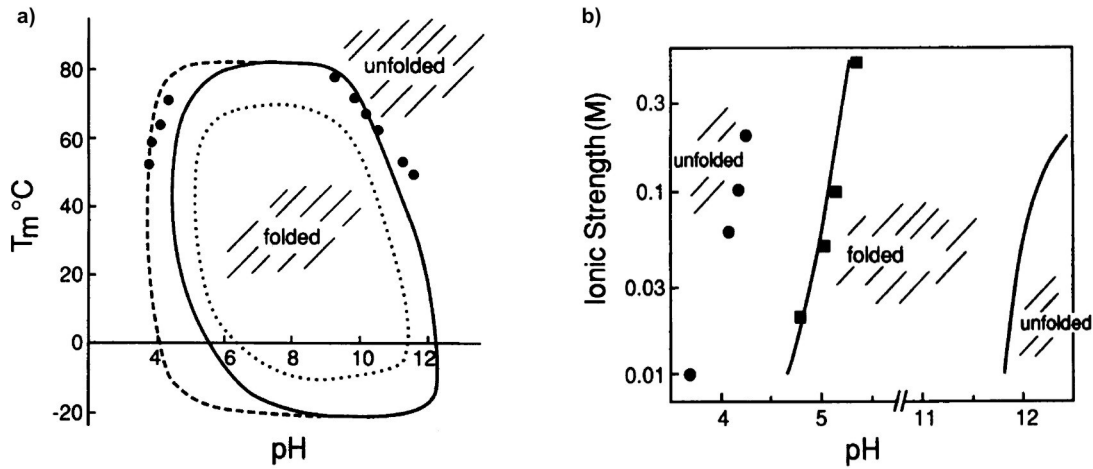


Figure 2.6: Folding transitions of myoglobin. (a) Denaturation temperature T_m in aqueous solutions of ionic strength 0.01 M versus pH. (b) Ionic strength versus pH at 25°C. Adapted from Stigter *et al.*¹⁰².

(low Reynolds number fluids). This simplifies greatly the Navier-Stokes equations governing the usual complex fluid mechanisms. The theory of fluid flow in nanochannels under pressure-driven flow conditions was also considered.

Different aspects of molecular diffusion were introduced. Random Brownian motion, finding its origin in the collisions of the molecules constituting the liquid on the particle surface, as well as the diffusion induced by a gradient concentration, were theoretically described, giving the basis of passive transport of biomolecules in liquids.

Electrostatics in liquids were also discussed, in particular surface charges appearing at glass surface when in contact with an aqueous solution which are compensated by counterions of the solution. This results in an electrical double layer at the solid-liquid interface. The potential distribution of the electrical double layer, which is described by the Poisson-Boltzmann equation, was solved with the Debye-Hückel approximation for 1D nanochannels.

Finally, models to simplify the description of biomolecules in liquids were commented, as well as their sensitivity when changing their environment conditions, such as the temperature, the pH or the ionic strength of the solution.

CHAPTER

3

FABRICATION AND EXPERIMENTAL SETUP

In this chapter, the design and the microfabrication process of the nanofluidic devices used in this thesis are introduced. The experimental setups for optical and electrical measurements are described as well as the fluidic and electrical interfaces that connect the fluidic device. Finally, the chip inner surface is characterized, and its equivalent electrical behavior is studied.

3. FABRICATION AND EXPERIMENTAL SETUP

3.1 System design and fabrication

Designing micro and nanosystems requires the extensive planning of operations because if a device function is not working properly, it is impossible to modify it directly on the chip and the whole process has to be repeated. Moreover, microsystems may be extremely difficult to manipulate by a user and intermediate supports have also to be designed. In the scope of this thesis, the specifications required to design and fabricate a system for detecting and manipulating proteins flowing and diffusing through nanoconfined channels, with one dimension (1D) below 100 nm are discussed. It was decided to design only 1D nanochannels (with a nanometer height) and not 2D nanochannels (with nanometer height and width) because of the higher probability to observe proteins passing through the channel and because the fabrication process is simpler. The concept of a nanochannel used later in this thesis is defined as a channel with a nanometer sized height and a finite micrometer sized width. The concept of nanoslit will be used when the nanochannel width is very large compared to its length or height (>100 times). Figure 3.1 presents an objectives tree aiming at detecting proteins in nanosized channels. The nanofluidic devices presented in the following sections have been designed by taking into account these requirements.

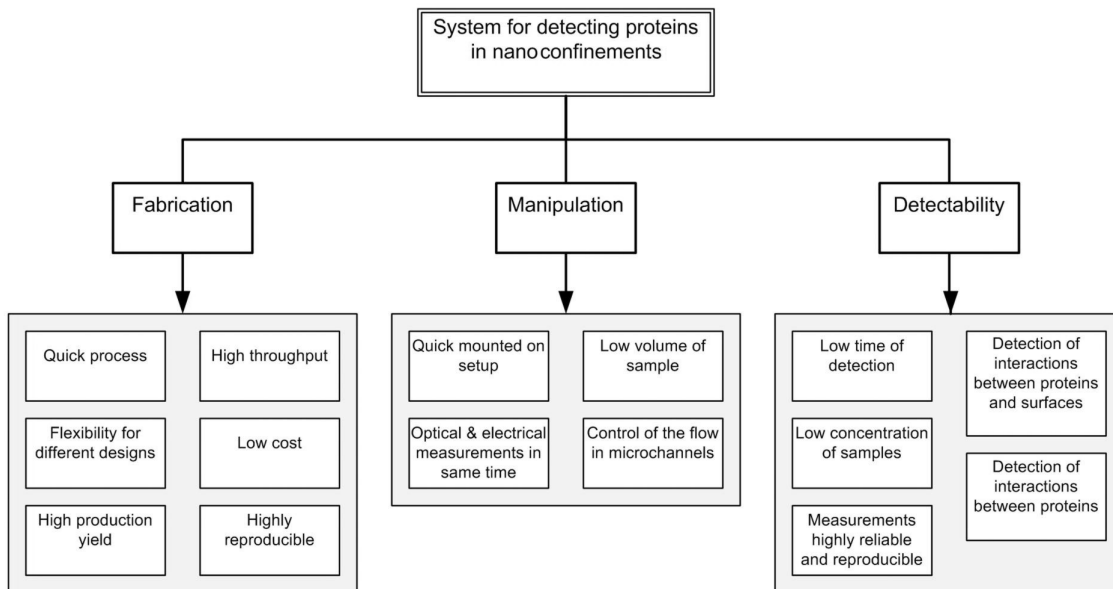


Figure 3.1: Objectives tree listing the initial requirements to design a system for detecting proteins in nanoconfinements.

3.1.1 Microfabrication process

Several kinds of glass substrates (float glass, BK7, Pyrex) with different values of refractive index were tested in order to evaluate which material was better matching with immersion objectives during single molecule tracking experiments. Pyrex was selected as the most appropriate substrate candidate because of its excellent quality over cost ratio. It has an excellent transparency to visible light and to UV, is a non-conductive material (allowing high electrical resistance measurements), and is rigid enough to be considered as non-deformable against high pressures existing within the nanochannels. Pyrex wafers with 100 mm diameter, 200 μm or 525 μm thickness and a roughness inferior to 1 nm were used. The microfabrication of the devices presented in this thesis was carried out at the EPFL Center of MicroNanoTechnology (CMI). The process which is based on a four-step process as illustrated in figure 3.2, was introduced by Schoch *et al.*²². Microchannels were firstly wet-etched on a Pyrex wafer by dissolution in HF solution (a). 50nm layer of titanium (Ti) and 150 nm thick platinum (Pt) electrodes were deposited and structured using standard evaporation and lift-off techniques (b). A 50 nm layer of amorphous silicon (aSi) was sputtered and structured by plasma etching (c). The thickness of this layer defines the height of the nanoslit. A second Pyrex wafer, in which access holes were drilled by sandblasting, was anodically bonded onto the first wafer (d). Afterwards, the wafers were diced into individual chips and were sometimes polished to reduce the bottom glass thickness to 170 μm , which assures a good matching with the standard glass slides used in microscopy. Standard microscopes can be used to observe the microchannels realized with this process, allowing simultaneous electrical and fluorescence measurements. In some of the following experiments, electrical measurements are not considered; microfabrication processes can then be simplified by ignoring the Ti-Pt deposition step.

3.1.2 Chip design

The layout was designed using CleWin 3.1 (WieWeb Software). A footprint of 10 mm x 12 mm was chosen which corresponds to a density of 48 chips per wafer. This is a good compromise between manipulation size, fragility of the glass wafer during the microfabrication and quantity of processed chips at the same time. The lateral dimensions are limited by the photolithography resolution which is about 1 μm at CMI. This means that our nanochannel cannot have a well defined width smaller than 1 μm , limiting the microfabrication process to a one-dimensional nanochannel or nanoslit. Focused ion beam (FIB) and electron beam lithography (EBL) are well-known tools

3. FABRICATION AND EXPERIMENTAL SETUP

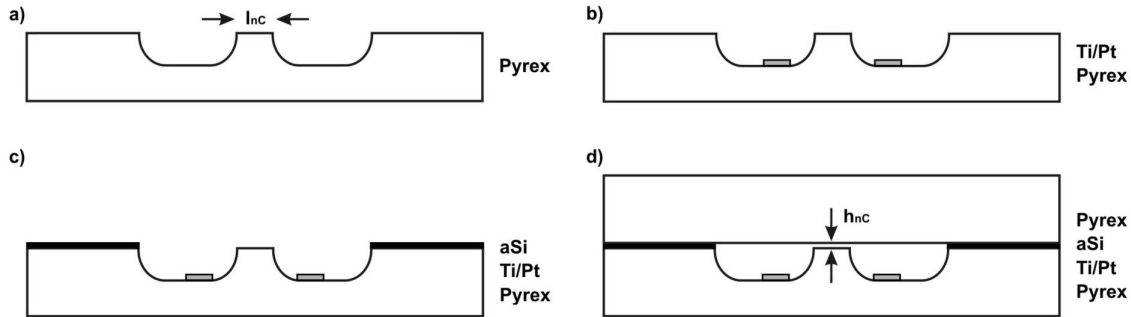


Figure 3.2: Cleanroom procedure for the fabrication of the nanochannels. (a) The microchannels are wet-etched on a Pyrex wafer. (b) 50nm Ti and 150nm Pt are evaporated and structured using a standard lift-off technique. (c) A 50nm layer of aSi is sputtered onto the wafer. This aSi layer defines the height h_{nC} of the nanochannels as it is used as a spacer between the Pyrex wafers. (d) Anodic bonding is performed in order to seal the structured wafer with another Pyrex wafer containing drilled access holes.

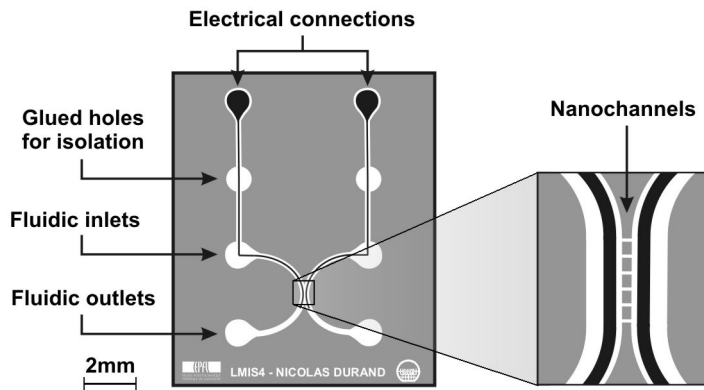


Figure 3.3: Design of the nanofluidic device constituted of two microchannels linked together by several nanochannels. Every microchannel contains at the bottom a platinum electrode (in black) which is connected to the measurement unit through the electrical connections access holes. Some access holes are filled with glue in order to avoid the external connectors coming in contact with the solution. The fluids are deposited in the inlets and are driven through the microchannels to the fluidic outlets by air pressure.

3.1 System design and fabrication

capable of obtaining two-dimensional nanochannels^{7;105;18}, but these techniques will not be used in the scope of this thesis and thus will not be discussed.

The height and width of the microchannels have to be large enough to allow efficient flow control with the air pressure regulator (from -0.8 to 4 bars), but they should also be thin enough to decrease the minimum sample volume (should be smaller than 1 ml/h). Moreover, deep microchannels imply that electrodes deposited at their bottom are far away from nanoslits, which inadequately increases the electrical impedance value of the microchannel.

The aSi layer defining the nanochannel height can be accurately defined due to sputtering resolution (inferior to 1 nm). A 50 nm thickness for aSi was chosen because it allows most proteins to pass through even if they are adsorbed on surfaces. Moreover, previous works^{22;106;107;108} have already used similar 50 nm height channels and the first measurements can be validated based on their results. Platinum electrodes have been designed large enough to decrease the parasitic capacitances due to the electrical double layer. However, they are not transparent and hide fluorescent molecules and parasitic air bubbles flowing at their top. Electrodes should also be located as close as possible to the nanochannels in order to decrease the electrical impedance.

Nanochannel length and width were designed to fit detection volumes in fluorescence experiments described in chapters 5 and 6. In chapter 4, the experiments are based on detecting electrical impedance which should be as low as possible when working with low ionic strength solutions in order to get readable values under 1 MΩ. Finally, in chapter 6, a novel concept of fluorescent measurements, based on the dispersion of proteins in an adjacent nanoslit situated at the end of the nanochannel is introduced. Table 3.1 presents the characteristics for the devices fabricated and used in the different chapters

		Electrical measurements (chap 4)	FCS measurements (chap 5)	Dispersion measurements (chap 6)
Microchannels	width $w_{\mu C}$	100 μm	100 μm	100 μm
	height $h_{\mu C}$	500 nm	5 μm	5 μm
Nanochannel	length l_{nC}		30 μm	15 μm
	width w_{nC}		10 μm	10 μm
	height h_{nC}		50 nm	50 nm
Adjacent nanoslit	length l_{nS}	3 μm		7 μm
	width w_{nS}	2.5 mm		1.4 mm
	height h_{nS}	50 nm		50 nm
Electrodes	width	15 μm		
	height	200 nm		

Table 3.1: Device characteristics

3. FABRICATION AND EXPERIMENTAL SETUP

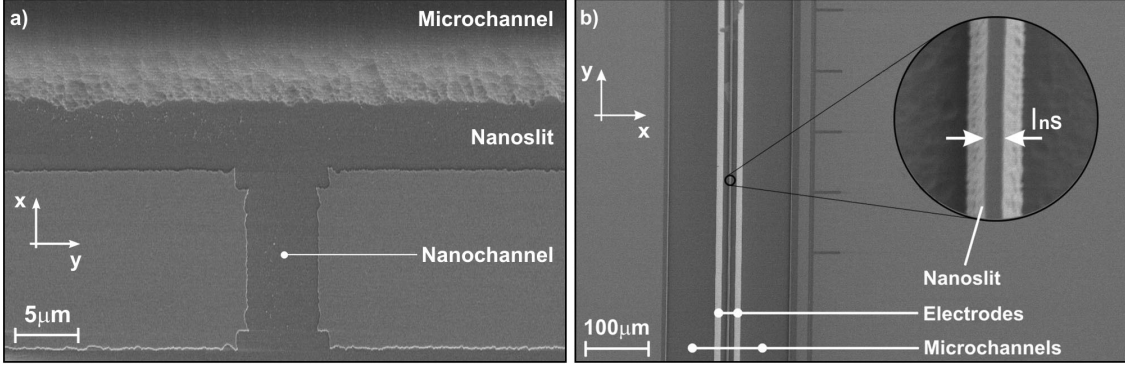


Figure 3.4: SEM images the nanofluidic system defined by the thickness of the aSi (top view). (a) Design adapted for optical measurements of chapters 4 and 6, showing a nanochannel of length $l_{nC}=15 \mu\text{m}$ and with $w_{nC}=5 \mu\text{m}$. A transversal nanoslit of length $l_{nS}=5 \mu\text{m}$ is present at the end of the nanochannel for dispersion measurements (chapter 6). (b) Design adapted for electrical measurements of chapter 5, showing a giant nanoslit of length $l_{nS}=3 \mu\text{m}$ and width $w_{nS}=2.5 \text{ mm}$. The inset picture represents the topography of the nanoslit.

of this thesis, and figure 3.4 shows an SEM picture of a manufactured nanochannel (a) and nanoslit (b).

Finally, UV photosensitive glue was used to isolate the electric connections from the fluidic part in order to prevent the liquid from filling the spring-loaded external electrodes, which render the impedance signal unsteady.

3.1.3 Experimental setup

To allow easy manipulation, control and detection of fluids inside the micro and nanochannels, an interconnection block made of poly-methyl-methacrylate (PMMA) was designed and fabricated. As illustrated in figure 3.5, the PMMA adapter allows a rapid mounting of the fluidic system in 2 steps: (a) after placing the o'rings (from Busak & Shamban) and the chip is added in their emplacements, with the adapter access holes overlapping with the chip tanks. Then the microscope mounting frame is placed and 4 screws restrain the chip aligned with the PMMA adapter and guarantee the dry conditions due to the o'rings. (b) the assembly is turned around and solutions are deposited into the adapter tanks with a syringe. By capillarity, the microchannels are filled and the absence of air bubbles can be optically confirmed. Finally, o'rings and a last PMMA cover with spring-loaded needles for electrical contact are added and constrained with 2 screws. For driving the liquids, an external air pressure in the lateral can be applied by lateral ports. The range of pressure actuation was from -0.8 to 4 bar.

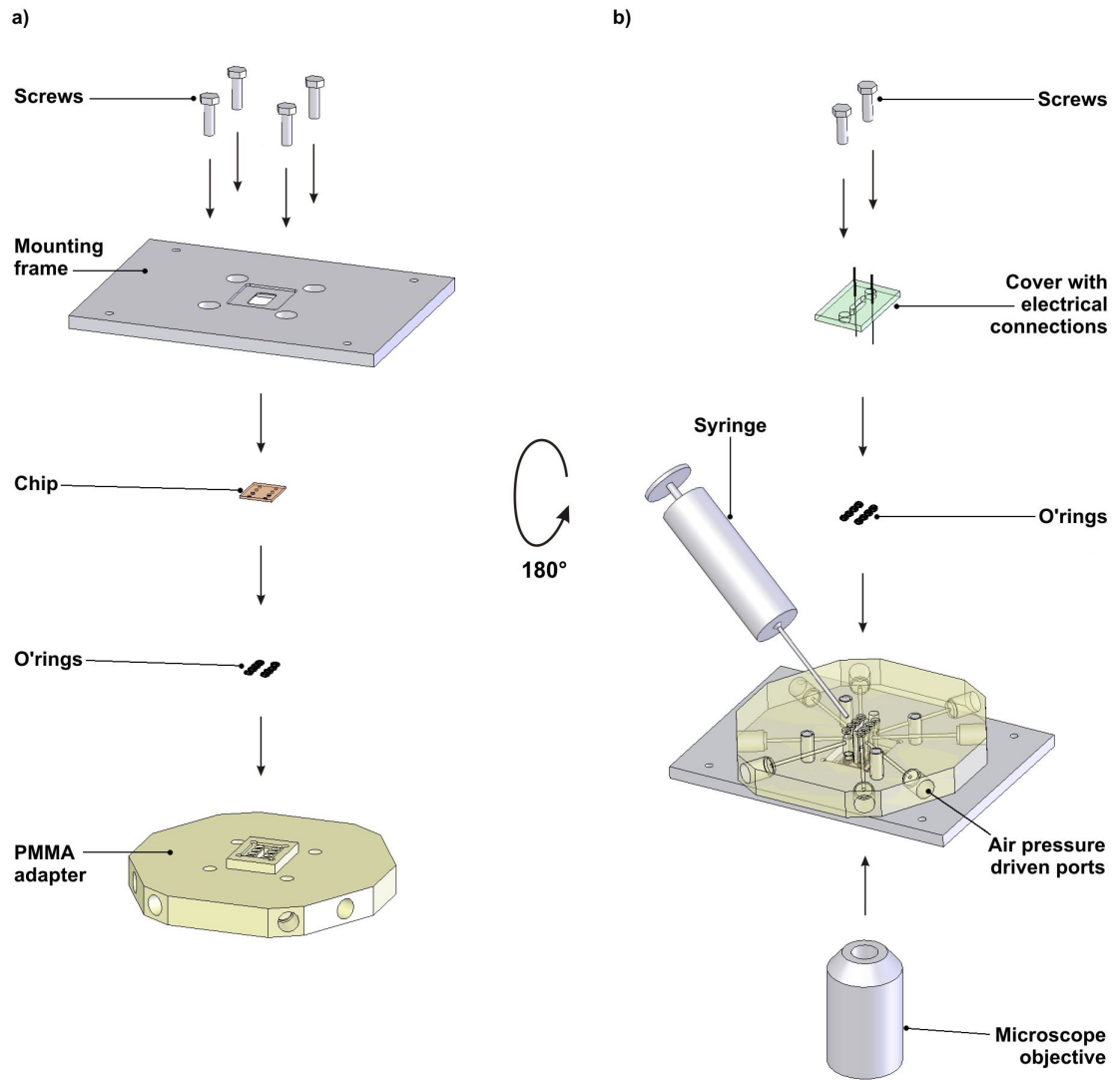


Figure 3.5: The setup for nanofluidic experiments allowing simultaneous electrical and fluorescence measurements. a) The chip is deposited onto a PMMA adapter containing o'rings for sealing. The microscope mounting frame maintains the chip in the right position and allows the microscope objective to be placed as close as possible to the bottom of the chip. (b) After turning up side down the assembled device, the solutions are injected by a syringe in the appropriate tanks. Only a small amount of the solution (<1ml) is needed. Finally a cover containing the electrical connections is added and the solutions are driven by air pressure through the lateral connections.

3. FABRICATION AND EXPERIMENTAL SETUP

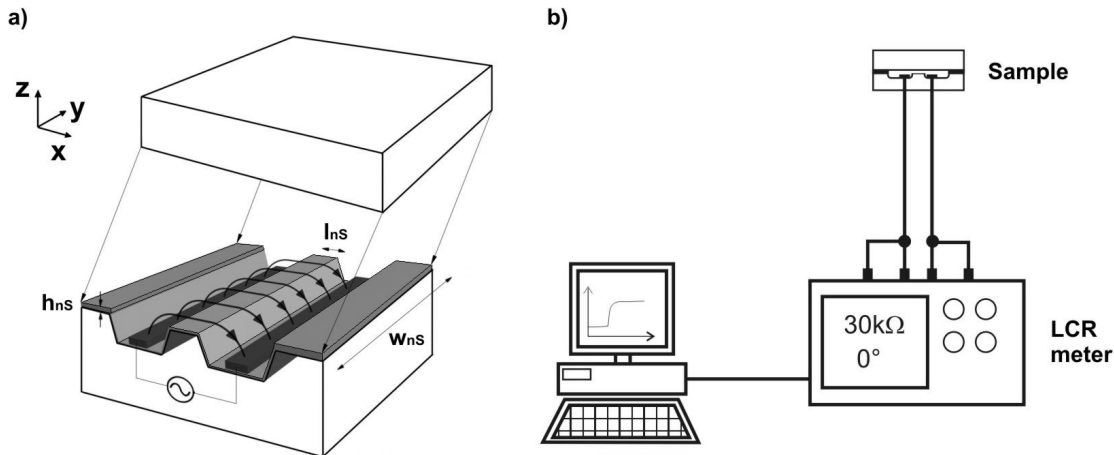


Figure 3.6: The nanofluidic device using electrical impedance measurement for the detection of proteins. (a) A 3D schematic of the nanofluidic system (not to scale). A driving voltage is applied to the electrodes, generating an electric field through the nanoslit (represented by lines with arrows). (b) Experimental setup for electrical measurements.

Electrical setup

For the electrical detection experiments which are reported in chapter 4, a precision LCR meter HP 4284A (from Agilent Technologies, Inc., Englewood) with a sinusoidal voltage of 100 mV peak-to-peak was used. Its principle is displayed in figure 3.6. Acquisition was controlled by a Matlab program, allowing recording measurements at a given frequency.

FCS setup

For the FCS experiments which are reported in chapter 5, a ConfoCor microscope (Carl Zeiss, Jena) has been used. Its principle is displayed in figure 3.7. The laser beam is generated by a 632.8 nm helium-neon laser and was enlarged by a beam shaper, filtered firstly through a clean-up filter and redirected to a 40x NA 1.15 water-immersion microscope objective by a dichroic mirror. The measured spot size inside the nanochannel, which was placed on a xyz table with a resolution of $1 \mu\text{m}$, was $r_{xy}=420 \text{ nm}$. Fluorescence emission from the sample was collected by the same objective and passed by the same dichroic mirror through a band-pass filter. Finally, the fluorescence emission was focused by a tube lens onto an avalanche photodiode (APD detector). The autocorrelation (from ALV correlator) is transferred to a computer and is analyzed with the FCS

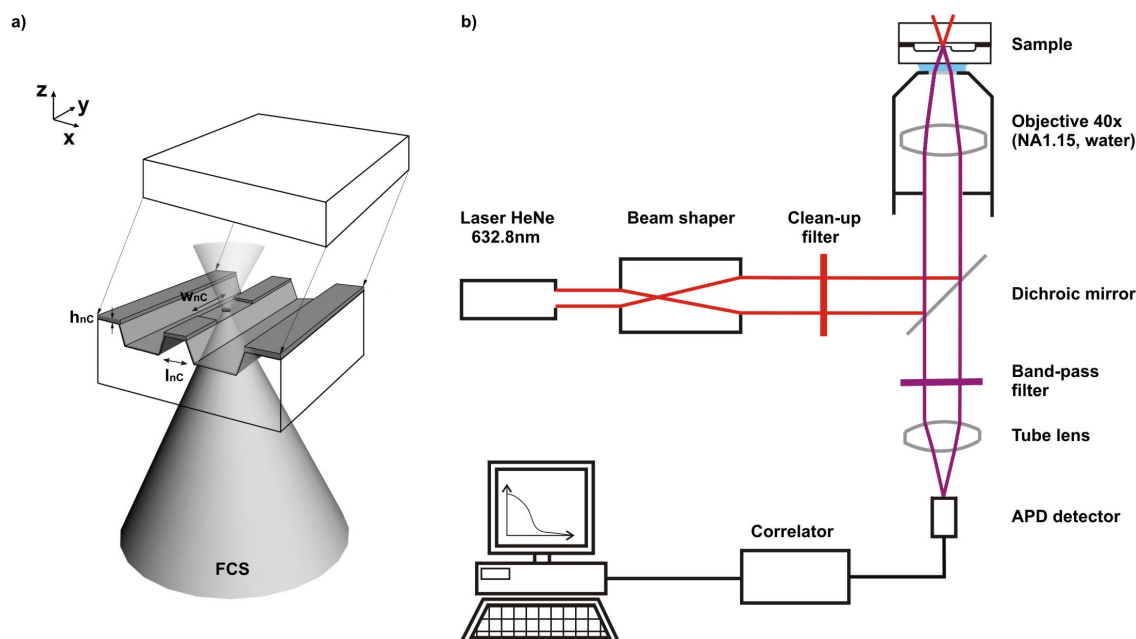


Figure 3.7: The nanofluidic device using fluorescence correlation spectroscopy (FCS) for the detection of proteins. (a) A 3D schematic of the nanofluidic system (not to scale). (b) Experimental setup for FCS measurements.

Access ConfoCor Control Program 1.2.1.1 (from Zeiss), as well as by a custom-made Matlab code R2006a (from MathWorks, Inc.).

Microscope setup

For the fluorescence experiments which are reported in chapter 6, an Axiovert S100 TV microscope (from Zeiss) was used. A first objective A-Plan 10x, NA 0.25 was used to get an overview of the area of interest and to control the absence of air bubbles, and a second water immersion Achroplan 40x, NA 0.8 objective was used for the detection.

3.2 Chip characterization

3.2.1 Surface roughness and glass dissolution

An important criterion of the quality of nanofluidic devices is the surface roughness, which can be in the same order of magnitude as the channel height. Atomic Force Microscopy (AFM) scanning was performed on chip before and after the microfabrication process. The measured averaged roughness of the initial Pyrex wafer was 1 ± 0.2 nm and 4.5 ± 0.2 nm after the multiple steps described in section 3.1.1. Several

3. FABRICATION AND EXPERIMENTAL SETUP

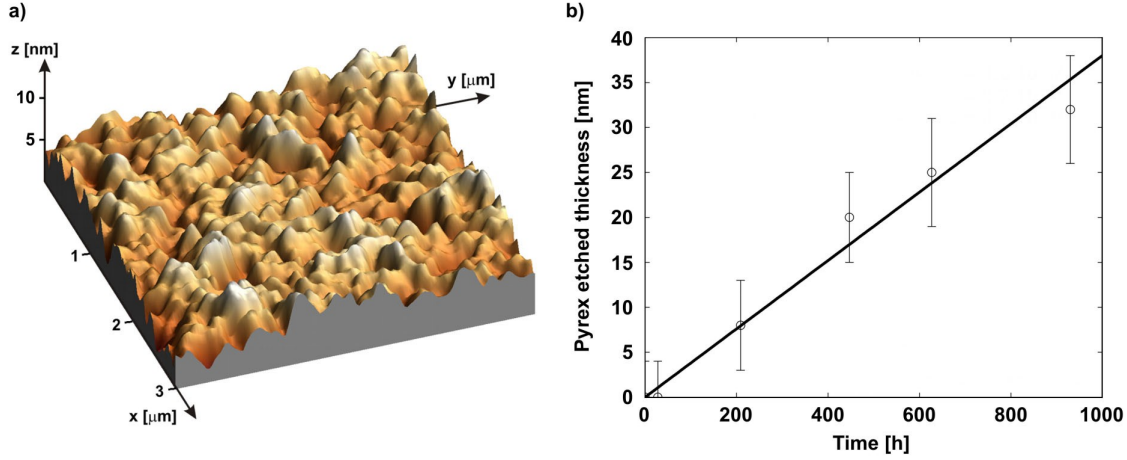


Figure 3.8: (a) AFM picture of a Pyrex surface ($3 \times 3 \mu\text{m}$) inside a nanochannel after microfabrication (just before the anodic bonding). The measured averaged roughness is $4.5 \pm 0.2 \text{ nm}$ in comparison with the initial value (Pyrex wafer before microfabrication) which is $1 \pm 0.2 \text{ nm}$. (b) The measurement of the Pyrex etch rate due to dissolution when the substrate is in deionized water during a long period.

analyses have highlighted that roughness peaks may be higher than 10 nm. This phenomenon is attributed to mask removal which is performed in different aggressive chemical baths (chromium etch, photoresist removal, etc.). Figure 3.8a highlights $3 \mu\text{m} \times 3 \mu\text{m}$ nanochannel surface topography as measured with an EasyScan AFM (from Nanosurf). A problematic limitation for a stable long-term use of a nanofluidic devices is the dissolution of glass when in contact with water; this is due mainly to ion exchange at the interface and to the diffusion of water into the glass¹⁰⁹. This phenomenon is increased when working with low ionic strength solutions. In order to measure the dissolution rate of the Pyrex used in the experiments of this thesis in low ionic strength conditions, several wafers coated with a structured gold layer were immersed in $18 \text{ M}\Omega\text{-cm}$ deionized water for 40 days. The difference in the level between the unetchable gold layer and the Pyrex surface was measured using a surface profiler Alpha-step 500 (from Tencor) with a resolution in height of 10 nm. The measured values are presented in figure 3.8b and a dissolution rate of $0.04 \pm 0.005 \text{ nm/h}$ is obtained. This value shows that our nanofluidic devices can be used multiple times before getting a strong difference of channel height due to glass dissolution.

3.2.2 Electrical characterization

The electrical model of the used system, in which electrodes are placed in the 2 microchannels linked together by a nanoslit, is presented in figure 3.9a. The equivalent

electrical circuit is composed by resistive elements and parasitic capacitances. R_{nS} and $R_{\mu C}$ correspond respectively to the electrical resistance of the nanoslit and microchannels. The value of the resistances of the microchannels, $R_{\mu C}$, is much lower than the resistance of the nanoslit. Its value is calculated using the electrical resistivity of the solution ρ_r :

$$R_{nS} = \rho_r \frac{l_{nS}}{w_{nS} h_{nS}} \quad (3.1)$$

$R_{\mu C}$ is calculated in the same way. The capacitances C_{EDL} result from the interface between the electrodes and the ionic solution. Its value is calculated using the permittivity of vacuum ε_0 , the dielectric constant of the solution ε_r , the area of the electrode A_{el} and the Debye length λ_D :

$$C_{EDL} = \frac{\varepsilon_0 \varepsilon_r A_{el}}{\lambda_D} \quad (3.2)$$

C_{stray} is the parasitic capacitance between the two electrodes through the glass. C_{stray} and can be measured when the chip does not contain solution and was measured to be 1.2 ± 0.2 pF. To avoid electrochemical reactions at the electrodes interface, a low AC voltage (100 mV) was chosen. The working frequency f_0 was tuned for the system to provide a resistive behavior, meaning a phase close to zero. Figures 3.9b and c

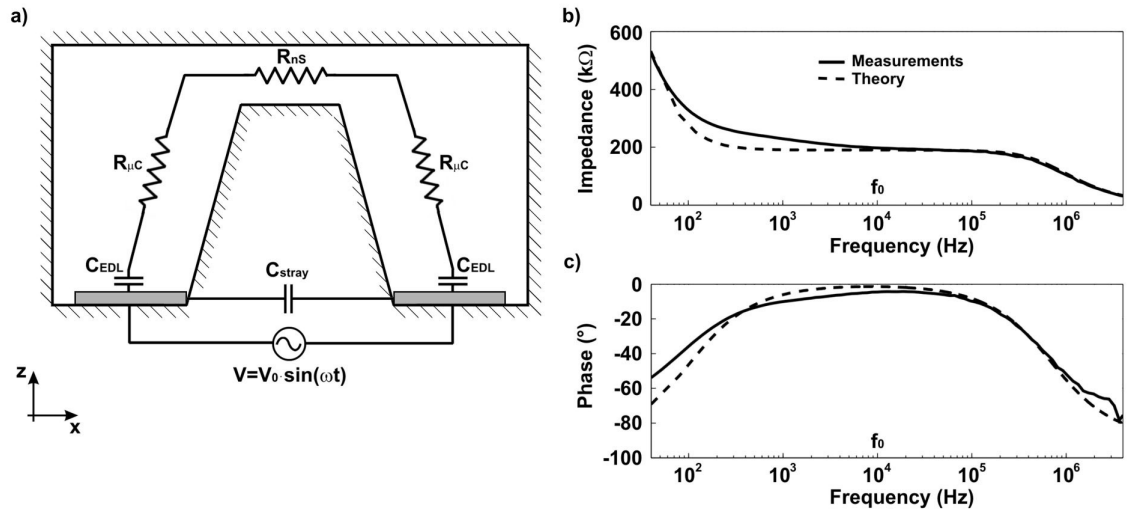


Figure 3.9: (a) Equivalent electrical model showing the electrical resistance of the channels, the capacitance due to the electrical double layer and the stray one. (b) Impedance measurement as a function of the frequency for a chip filled with a solution composed of 10% PBS and 90% deionized water. f_0 corresponds to the most resistive case, *i.e.* when the phase is close to zero as shown on plot (c).

3. FABRICATION AND EXPERIMENTAL SETUP

show the impedance and phase measurements for a large range of frequencies when the device is filled with a 10% phosphate buffered saline solution (PBS) and 90% deionized water. The equivalent electrical model for the working frequency f_0 and the value of the impedance in function of the frequency $|Z(f_0)|$, which were used for the fitting, were mathematically developed and are expressed as follows:

$$f_0 = \sqrt{\frac{0.5C_{EDL} + C_{stray}}{\pi^2 (2R_{\mu C} + R_{nS})^2 C_{stray} C_{EDL}^2}} \quad (3.3)$$

$$|Z(f_0)| \approx \frac{(2R_{\mu C} + R_{nS})C_{EDL}^2}{4\pi^2 C_{stray}^2 C_{EDL}^2 (2R_{\mu C} + R_{nS})^2 f_0^2 + (2C_{stray} + C_{EDL})^2} \quad (3.4)$$

3.3 Conclusion

The design and fabrication of microchannels linked together by 1D nanochannels and nanoslits was described. The different setups used for measuring the presence and diffusion of proteins in nanoconfinements using fluorescence correlation spectroscopy, by means of measuring the electrical impedance or using standard fluorescence microscopy, were introduced. Nanochannel surfaces roughness was measured by atomic force microscopy before and after microfabrication, and Pyrex dissolution during water immersion was also measured highlighting that a hundred hours are needed to significantly increase the nanochannel height. Finally, the electrical characterization of the system was performed, showing the presence of a stray capacitance between electrodes and capacitance effects due to electrical double layer at the interface between electrodes and liquid. Impedance measurements also highlighted the frequency range where the phase is close to zero and the channel behavior is mostly resistive.

CHAPTER

4

ELECTRICAL DETECTION OF PROTEINS KINETICS IN NANOCONFINEMENTS

This chapter reports on the electrical detection and characterization of protein kinetics in nanoconfinements. Firstly, I present a theoretical model describing the diffusion of biomolecules in nanoconfinement and taking into account the steric exclusion, the reversible surface adsorption of the biomolecules, and the exclusion-enrichment effect due to the charge of the proteins and to the ionic strength of the solution. Secondly, I investigate kinetic parameters for the adsorption and desorption of proteins on surfaces over a wide range of pH and at different ionic strengths; finally, adsorbed bovine serum albumin (BSA) protein was electrically detected with response times in the minute range.*

* Adapted from the journal article:

N. F. Y. Durand and P. Renaud, "Label-free determination of protein-surface interaction kinetics by ionic conductance inside a nanochannel", *Lab on a Chip*, **9**(2), 319-324, 2009.

4. ELECTRICAL DETECTION OF PROTEINS KINETICS IN NANOCONFINEMENTS

4.1 Motivation

In nanoconfinements, biomolecules transport is occurring close to surfaces and in some conditions, the solute is interacting with the surfaces and may be immobilized. This phenomenon, called adsorption, is extremely important in nanofluidics because it influences directly the diffusion and the concentration of biomolecules. The measurement of the kinetics of adsorption of proteins on surfaces and equilibrium adsorption isotherms have been reported using different techniques, including optical waveguide lightmode spectroscopy (OWLS)^{110;111}, ellipsometry¹¹², total internal reflectance fluorescence (TIRF)^{113;114;115;116;117} or surface plasmon resonance (SPR)^{118;119;120}. All these methods have shown that kinetic effects are often complex, dependant on salt concentration, protein charge or dipole moment, surface charge and hydrophobicity¹¹⁴.

Micro and nanofluidics¹²¹ applications have received much interest over the last 10 years, mainly because of the reduction in detection time due to the large surface to volume ratio and to the reduced sample volume. Diffusive transport at that length scale implies short diffusion times meaning an increase in the speed of the analysis. Recently Karnik *et al.*⁶¹ and Schoch *et al.*⁶² reported electrical detection possibilities of chemical binding inside nanoslits. They have demonstrated that molecules entering a confined area can change the volume conductance, which can be easily measured. Such electrical biosensors on a chip are promising due to the low-cost and the simplicity of the detection system.

In this chapter, I will firstly introduce a simple model describing the protein-surface interaction. Novel theoretical models for predicting the effect of the nanoconfinement on protein diffusion, taking into account the protein-surface interaction, are proposed. The effect of the protein adsorption on the electrical conductance across a nanoconfinement will also be discussed and based on simple adsorption experiments, the different regimes governed by the solution characteristics (ionic strength, pH, charge and concentration of molecules, etc.) will be described. This study is the preliminary step for understanding future immunological detection based on coupling nanofluidic devices with electrical measurements.

4.2 Adsorption and desorption kinetics

The Langmuir isotherm model¹²² is an adsorption kinetics theory accounting for reversible adsorption. The exponential model for the capture rate at constant concentration, which is governed by the rate of adsorption k_{on} and desorption k_{off} , is usually used to describe the behavior of molecules adsorption:

$$\Gamma(t) = \Gamma_0(1 - e^{-t/\tau}) \quad (4.1)$$

where the surface concentration $\Gamma(t)$ is a function of time t , and the effective surface coverage Γ_0 is a function of the full coverage surface concentration Γ_{max} :

$$\Gamma_0 = \Gamma_{max} \frac{k_{on}c_0}{k_{on}c_0 + k_{off}} \quad (4.2)$$

where c_0 is the protein concentration. The time constant τ to get the proteins adsorbed, is given by

$$\tau = \frac{1}{k_{on}c_0 + k_{off}} \quad (4.3)$$

After the injection of the proteins, when the equilibrium is reached, the effective surface coverage Γ_0 is reduced compared to the full coverage Γ_{max} due to the adsorption and desorption of proteins, as described by equation 4.2. The ratio of the rate of adsorption over the rate of desorption k_{on}/k_{off} determines the equilibrium constant K , which is constant for a given type of protein.

Norde *et al.*^{123;124} have investigated the adsorption of proteins in different pH conditions. As illustrated in figure 4.1, they simply demonstrated that when biomolecules are charged (pH away from pI), the intra- and inter-molecular electrostatic repulsion results in more expanded molecules and thus adsorb in a less dense layer.

4. ELECTRICAL DETECTION OF PROTEINS KINETICS IN NANOCONFINEMENTS

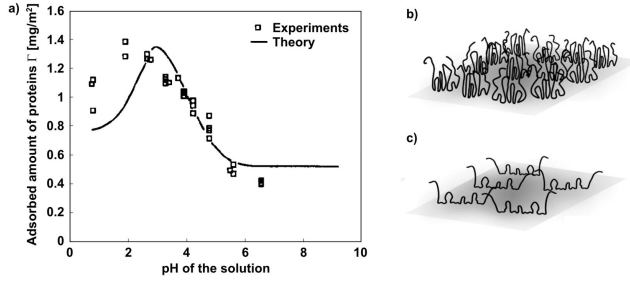


Figure 4.1: (a) Experimental adsorption of polyacrylic acid onto a cationic latex, from Stuart, *et al.*¹²⁵. Illustrations adapted from Norde¹²³ depicting that (b) in the isoelectrical state (pH=pI=2.5) intramolecular electrostatic interaction renders the molecules relatively compact and because of the overall electroneutrality, and thus they pack in a dense layer. (c) At pH values away from the isoelectric point, when the molecules possess a net amount of charge, intra- and inter-molecular electrostatic repulsion results in more expanded molecules that adsorb in a less dense layer.

4.3 Hindered diffusion of proteins in nanoconfined spaces

4.3.1 The partitioning effect

For solutes such as globular spherical proteins that are large enough to behave as hydrodynamic particles, the constrained space of a nanoconfinement causes the molecular friction coefficient to exceed its maximum value and leads to steric exclusion. This kind of hindered diffusion, has been extensively studied with neutral spheres in cylindrical nanopores^{126;127;128;129;130}. The equilibrium partitioning of solute concentration between inside and outside a nanoslit, assuming there is no surface close to the measurement volume outside the nanoconfinement, is given by^{126;131}:

$$\Phi = \frac{c_{nS}}{c_0} = \int_0^{(1-\lambda)} e^{-\frac{E(\beta)}{k_B T}} d\beta \quad (4.4)$$

where c_{nS} is the mean concentration of solute in the nanoslit and c_0 the concentration of solute in the bulk. λ is defined as the ratio of the solute diameter d_s to nanoslit height h_{nS} ($\lambda = d_s/h$) and $\beta = 2z/h - 1$ is the dimensionless z position (z is the projection axis parallel to the height). E is a potential describing long range interactions between the solute and the nanoslit walls which are here assumed to depend only on the z position, k_B is the Boltzmann constant and T the temperature in Kelvin. Equation 4.4 indicates that when the size of the particles is close to the height of the channel, a decrease of the solute concentration is expected within the nanoslit. The initial physical situation can therefore be depicted as in figure 4.2.

4.3 Hindered diffusion of proteins in nanoconfined spaces

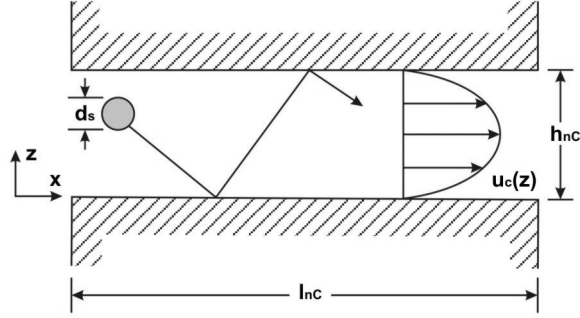


Figure 4.2: Spherical solute of diameter d_s in a nanoslit of height h_{nS} and length l_{nS} . A convective flow $u_c(z)$ is schematically depicted.

When the solute is not charged, as it is the case at the isoelectrical point (pI) for proteins, equation 4.4 is reduced to $\Phi = (1 - \lambda)$. If there is no adsorption, assuming that biomolecules are elastically bouncing on surfaces, the concentration of species inside the nanoconfinement is simply:

$$c_{nS} = (1 - \lambda)c_0 \quad (4.5)$$

However, the protein-surface interactions are almost always present and the total concentration inside the confined space must take into account the number of molecules in the bulk and of those adsorbed on the nanoslit surfaces. As presented in the previous section, the Langmuir isotherm model¹²², which describes reversible adsorption, can be coupled with equation 4.5 used to define the concentration in a nanoslit (mainly composed of 2 surfaces). The nanoslit concentration, taking into account both the molecules in the free-diffusion space (bulk) of the nanoslit and those adsorbed on the walls, is:

$$\Gamma_0 = \Gamma_{max} \frac{(1 - \lambda)k_{on}c_0}{(1 - \lambda)k_{on}c_0 + k_{off}} \quad (4.6)$$

$$c_{nS} = (1 - \lambda) \underbrace{\left[c_0 + \frac{\Gamma_0}{500N_A h} \right]}_{\chi \cdot c_0} \quad (4.7)$$

where N_A is the Avogadro constant.

4. ELECTRICAL DETECTION OF PROTEINS KINETICS IN NANOCONFINEMENTS

I defined the bulk-surface partitioning cofactor χ as:

$$\chi = 1 + \frac{\Gamma_0}{500N_A h c_0} = 1 + \frac{\Gamma_{max}}{500N_A h} \cdot \frac{(1-\lambda)k_{on}}{(1-\lambda)k_{on}c_0 + k_{off}} \quad (4.8)$$

To take into account the electrostatic interactions between charged molecules and charged surfaces as well as the interactions of the solute with the electrical double layer (EDL), depending on the ionic strength of the solution c_i , a model given by Plecis *et al.*¹⁰⁶ describing the exclusion-enrichment effect was used. This model introduces a partitioning coefficient ϕ_β , which takes into account the electrostatic effects and the interactions with the EDL, but ignores the steric exclusion due to the solute size, as well as the adsorption effect:

$$\Phi_\beta = \frac{1}{h} \int_0^h e^{-\frac{q\Psi(z)}{k_B T}} dz \quad (4.9)$$

where q is the net charge of the solute and $\Psi(z)$ is the Debye-Hückel approximation for the electrical potential between two infinite planar surfaces⁹⁸:

$$\Psi(z) = \zeta \frac{\cosh((h/2 - z)/\lambda_D)}{\cosh(h/2\lambda_D)} \quad (4.10)$$

where ζ is the zeta potential and λ_D the EDL thickness corresponding to the Debye screening length, in a 1:1 electrolyte solution¹⁰⁶:

$$\lambda_D = \sqrt{\frac{\varepsilon_0 \varepsilon_r R T}{2 F^2 c_i}} \quad (4.11)$$

where ε_0 is permittivity of vacuum, ε_r the dielectric constant of the medium, R the molar gas constant and F the Faraday constant. This model is appropriate for very small ratio molecules size over channel height ($\lambda \rightarrow 0$) such as those used in the experiment presented in figure 4.3.

Combining these contributions (adsorption, steric exclusion and electrostatic interactions) by combining equations 4.4, 4.8 and 4.9, the equilibrium partitioning coefficient for solute concentration between inside and outside a nanoslit Φ_{nS} can be defined as:

$$\Phi_{nS} = \frac{c_{nS}}{c_0} = \frac{\chi}{h} \int_0^{h(1-\lambda)} e^{-\frac{q\Psi(z)}{k_B T}} dz \quad (4.12)$$

4.4 Effect of the presence of proteins on the nanoslit conductance

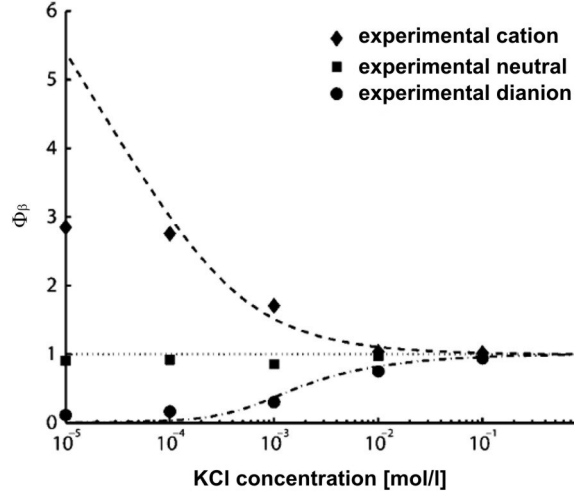


Figure 4.3: Variation of the partitioning coefficient (relative permeability) of a $3\mu\text{m}$ long nanoslit versus ionic strength for different probe charges. Marks represent experimental measurements whereas dotted lines are theoretical fittings obtained with equation 4.9. Native Pyrex surface is negatively charged which excludes anions (fluorescein) when EDL overlap occurs at low KCl concentrations. On the contrary, cations (rhodamine 6G) are attracted in the channel, which enhances their transport to the other microchannel. Neutral rhodamine B is not influenced by the electrical double layer thickness. Adapted from Plecis *et al.*¹⁰⁶.

When the solute is neutral, the charge q is zero and the exclusion-enrichment effect is no longer affecting the partitioning coefficient. Equation 4.12 is then reduced to:

$$\Phi_{nS} = (1 - \lambda) \left[1 + \frac{\Gamma_{max}}{500N_A h} \cdot \frac{(1 - \lambda)k_{on}}{(1 - \lambda)k_{on}c_0 + k_{off}} \right] \quad (4.13)$$

Equation 4.13 is also valid at very high ionic strength whatever the molecules charge, because $\Psi(z) \rightarrow 0$ in this case for almost every z (except $z \rightarrow 0$ or $z \rightarrow h$, but this can be neglected in very high ionic conditions).

4.4 Effect of the presence of proteins on the nanoslit conductance

In the absence of adsorbed biomolecules on the nanoslit walls, the nanoslit conductance is governed by the surface charges at low ionic concentration, resulting in an offset conductance as observed by Stein¹³² and showed in figure 4.4. At high ionic concentration, the nanoslit conductance is governed by the channel geometry. The nanoslit conductance G in steady-state conditions of a bare nanoslit before protein adsorption, when

4. ELECTRICAL DETECTION OF PROTEINS KINETICS IN NANOCONFINEMENTS

filled with a 1:1 electrolyte solution, has been proposed by Schoch *et al.*¹⁰⁸ and is given by

$$G = \underbrace{(\mu_+ + \mu_-)c_i N_A e \frac{wh}{l}}_{G_V} + \underbrace{2\mu_{\text{opposite}} |\sigma_0| \frac{w}{l}}_{G_S} \quad (4.14)$$

where μ is the ionic mobility (subscripts denote cation/anion and “opposite” indicates counterions of opposite charge to the surface charge), σ_0 the surface charge density in the diffuse layer (assuming that the species in the inner Helmholtz plane are immobile), N_A the Avogadro constant, e the electron charge and c_i the electrolyte ionic concentration. The conductance G in the nanoslit is obtained through the addition of the bulk conductance G_V and the conductance G_S due to excess counterions equilibrating surface charges. In this model, it is assumed that the protein concentration along the nanoslit is constant and that the presence of biomolecules adsorbed to the channel surfaces can change the nanoslit conductance mainly for 2 reasons: i) the decrease of the effective volume of the nanoslit due to the presence of the proteins, and ii) the change of the surface charges because of the charged absorbed biomolecules and thus of the counterions concentration. Constant properties of proteins and no lateral interactions between adsorbed molecules are assumed. The immobilized proteins contribute to the

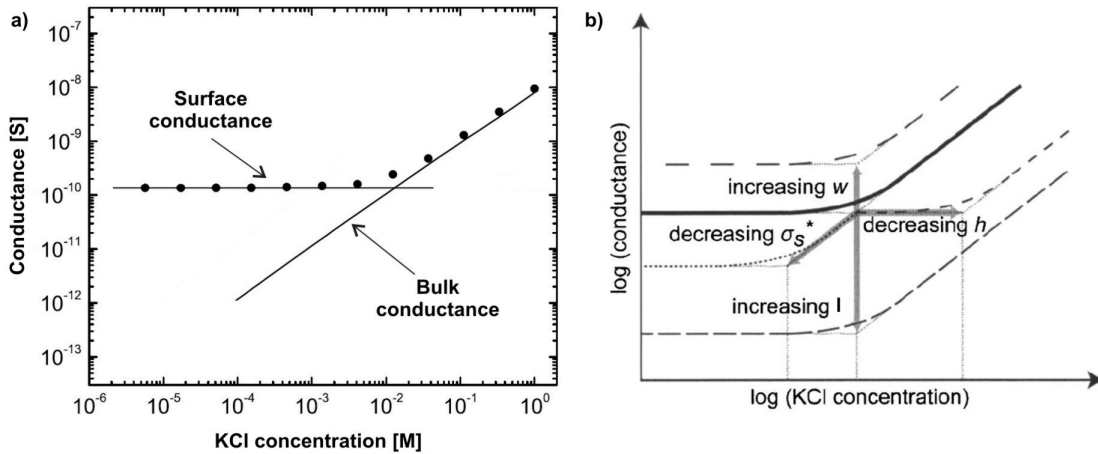


Figure 4.4: a) Electrical conductance of 70 nm high aqueous-filled, fused silica channel as a function of the ionic strength of the KCl solution. The lines depict the conductance expected in each channel from the conductivity of the bulk solution, and the observed surface conductance for low ionic strength solutions. Adapted from Stein, *et al.*¹³² b) Impact of the characteristic effective surface charge density σ_s , the width w , the length l , and the height h of the nanoslits on the nanoslits conductance. Adapted from Schoch, *et al.*¹⁰⁸

4.4 Effect of the presence of proteins on the nanoslit conductance

change of conductance related to the channel geometry. As the volume of the proteins decreases the nanoslit section, a resulting decrease in nanoslit conductance occurs:

$$\frac{\Delta G_V}{G_V} = -\frac{\Delta V}{V_0} = -\frac{2V_p}{h}\Gamma(t) \quad (4.15)$$

where $\Delta G_V/G_V$ is the normalized conductance change of the nanoslit relatively to G_V , ΔV is the decrease of volume of the nanoslit, V_0 the initial volume of the channel and $\Gamma(t)$ is the surface concentration of bound molecules. The adsorbed proteins also change the nanoslit conductance G_S because of the change of the effective surface charge density σ_S . In this model, it is assumed that the initial surface charges are progressively replaced by every protein adsorbing on the surface. Each protein also brings new counterions to the surface:

$$\sigma_S = \left(1 - \frac{\Gamma(t)}{\Gamma_{max}}\right)\sigma_0 + n_p e \Gamma(t) \quad (4.16)$$

where n_p is the charge of one protein, depending on pH. The normalized conductance change of the nanoslit relative to G_S can be written as follows:

$$\frac{\Delta G_S}{G_S} = \frac{|\sigma_S| - |\sigma_0|}{|\sigma_0|} \quad (4.17)$$

The total normalized conductance change $\Delta G/G$ is obtained through the combination of equations 4.14, 4.15 and 4.17:

$$\frac{\Delta G}{G} = \frac{G_V}{G} \frac{\Delta G_V}{G_V} + \frac{G_S}{G} \frac{\Delta G_S}{G_S} \quad (4.18)$$

With high ionic strength solutions, conductance changes in the nanoslit are dominated by the channel geometry and the first term of equation 4.18 is dominant. However, at low salt concentration, conductance becomes increasingly dominated by surface charges and the second term of equation 4.18 becomes dominant. This last term gives a positive conductance change upon protein adsorption and is characterized by the protein charge. A strong dependence on the pH is therefore expected since protein charge n_p will change with pH. The protein charge is positive below the isoelectric point (pI) and is negative at pH above pI.

4. ELECTRICAL DETECTION OF PROTEINS KINETICS IN NANOCONFINEMENTS

4.5 Electrical measurements

As presented in figure 3.6, the device used in the experiment consists of 2 microchannels linked together by a short but wide nanoslit (height $h_{nS}=50$ nm, length $l_{nS}=3$ μm , width $w_{nS}=2.5$ mm). The width of the nanoslit is large in order to decrease the measured impedance and allows measurement when the solution has a low ionic concentration. External positive and negative pressures allow driving the flow in each 500 nm deep microchannel. Platinum electrodes placed on each side near the nanoslit allow the measurement of the nanoslit impedance.

Experiments were carried out to evaluate the conductance changes of the nanoslit due to the adsorption and desorption of bovine serum albumin (BSA, 66 kDa, from Sigma-Aldrich) on its walls: first the microchannels and the nanoslit were filled with a clean phosphate buffered saline solution (PBS, from Sigma-Aldrich, containing 137 mM sodium chloride, 10 mM phosphate buffer and 2.7 mM potassium chloride) by establishing a flow between the inlet and the outlet ports. When the PBS solution fills the whole device, the measurement of the impedance is started. After being inserted, BSA diluted in PBS diffuses in the nanoslit, resulting in a change of the impedance of the nanoslit. The impedance reaches an asymptotic value when BSA molecules have reached the maximum effective coverage.

4.5.1 Adsorption kinetics at high ionic strength

At high ionic strength, the conductance of the nanoslit is decreasing with time due to the dominance of first term in equation 4.14. Figure 4.5 shows an adsorption experiment where a 600 μM BSA solution was injected in the nanofluidic system containing high ionic concentrated PBS solution (137 mM NaCl). The curve shows a typical behavior of adsorption kinetics at surfaces.

The adsorption experiment was reproduced with different initial values of the BSA concentration c_0 (from 600 nM to 600 μM) in high ionic strength conditions. The surface conductance G_S is negligible at high ionic concentration and the kinetics curve can be fitted using equation 4.15. Figure 4.6 shows the temporal evolution of the normalized conductance change during the adsorption of the proteins on the Pyrex nanoslit walls for various initial concentrations of BSA injected in the microchannel. When reducing the protein concentration, the time constant of the adsorption phenomenon increases strongly, in accordance with equation 4.3, and the saturated conductance change value decreases. As presented in figure 4.7, the same experiment was reproduced when a

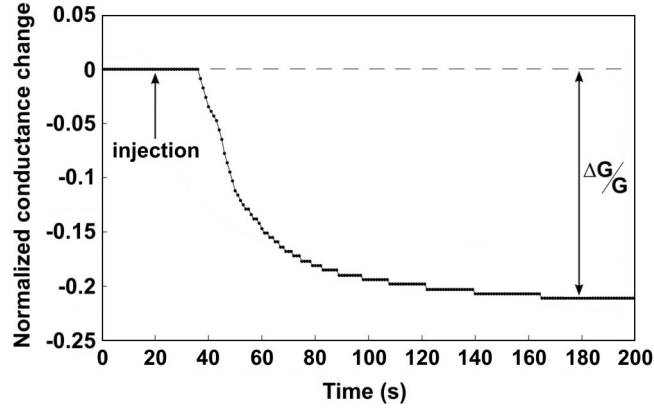


Figure 4.5: Nanoslit conductance response of BSA adsorbed at Pyrex surfaces when channels are filled with PBS solution corrected to pH=6 by addition of HCl. The 600 μM BSA solution was injected at $t=20$ s and adsorbed on the nanoslit's walls. The value $\Delta G/G$ is measured when the normalized conductance change reaches an asymptote. The delay observed between injection and start of change is due to the time to reach the nanoslit.

negative or positive differential pressure is applied across the nanoslit. A negative pressure pushes clean PBS solution across the aperture and clearly decreases the speed of diffusion of the proteins in the aperture. When a positive value of the pressure is used, the proteins are pushed across the aperture such that the flow conditions in the nanoslit allow for small increases in the maximum effective adsorption sites compared to purely diffusive conditions.

In order to model the adsorption kinetics, a simplified geometrical model of a spherical BSA molecule with a radius $r_s=4$ nm (from Yoon, *et al.*¹³³) is used to calculate V_p . The assumption of full surface coverage Γ_{max} is made with the same model, postulating a compact hexagonal packing on surface:

$$\Gamma_{max} = \frac{1}{2\sqrt{3}r_s^2} \quad (4.19)$$

With this model, equation 4.6 and 4.15 become:

$$\Gamma_0 = \frac{1}{2\sqrt{3}r_s^2} \cdot \frac{(1-\lambda)k_{on}c_0}{(1-\lambda)k_{on}c_0 + k_{off}} \quad (4.20)$$

$$\frac{\Delta G}{G} = -\frac{8\pi r_s^3}{3h} \Gamma_0 \quad (4.21)$$

4. ELECTRICAL DETECTION OF PROTEINS KINETICS IN NANOCONFINEMENTS

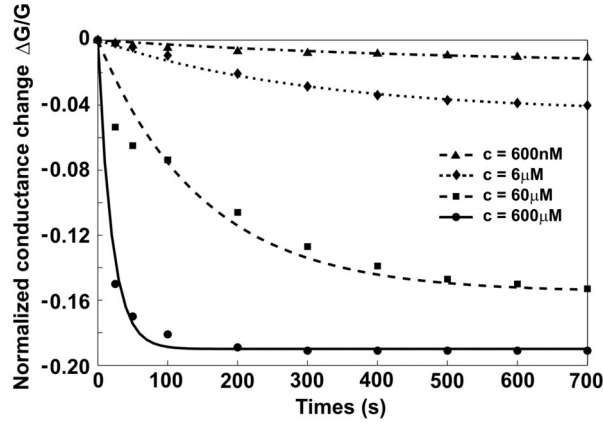


Figure 4.6: Evolution of the normalized conductance change with time for various initial concentrations of BSA. The time constant of the adsorption phenomena decreases with increasing BSA concentration. The experiments are realized in PBS solution with pH of 4.9 corresponding to the isoelectric point of BSA. Points represent measurements and lines are exponential fit from which experimental adsorption kinetic values $\Delta G/G$ and τ are extracted (second column, table 4.1).

The equilibrium coverage ratio of the surface can be expressed by:

$$\frac{\Gamma_0}{\Gamma_{max}} = -\frac{3\sqrt{3} h \Delta G}{4\pi r_s G} \quad (4.22)$$

The maximum surface coverage $\Gamma_{max}=1.8 \cdot 10^{16}$ mol/m² obtained with equation 4.19 is close to the measured value in similar conditions by Duncan, *et al.*¹³⁴ of $2.6 \cdot 10^{16}$ mol/m².

The values of measured time constants and normalized conductance changes are presented in table 4.1 and compared to the calculated ones. Calculations are best fittings of experimental data, using $k_{on}=100$ M⁻¹s⁻¹, $k_{off}=0.002$ s⁻¹ and $r_s=4$ nm. Remarkably

c_0 (μ M)	Experimental data extracted from figure 4.6a		Calculated data with equations 4.3, 4.20 and 4.21		
	$\Delta G/G$	τ (s)	$\Delta G/G$	τ (s)	Γ_0 (mol/m ²)
600	-0.19 ± 0.02	20 ± 5	-0.19	16	$1.75 \cdot 10^{16}$
60	-0.16 ± 0.01	150 ± 30	-0.15	125	$1.35 \cdot 10^{16}$
6	-0.04 ± 0.005	300 ± 80	-0.04	385	$4.15 \cdot 10^{15}$
0.6	-0.01 ± 0.005	500 ± 120	-0.01	485	$5.41 \cdot 10^{14}$

Table 4.1: Comparison between measured and calculated conductance changes due to BSA adsorption in a nanoslit. The experimental values $\Delta G/G$ and τ are extracted from the data shown in figure 4.6a with an exponential fit. The calculated values have been obtained using equations 4.21, 4.3 and 4.20 with the following values: $k_{on}=100$ M⁻¹s⁻¹, $k_{off}=0.002$ s⁻¹, $r_s=4$ nm and $h=50$ nm. The relative surface coverage is calculated with the same parameters and displayed in the last column.

good fits are obtained considering the simplicity of the model. This allows direct determination of the rate of adsorption k_{on} and desorption k_{off} of label-free proteins on surface interactions.

Effect of an induced flow on the electrical conductance

Schoch *et al.*⁶² have studied the influence of an induced flow on the nanoslit conductance, and have shown that a positive flow strongly decreases the coating time t_c . Assuming pressure-driven transport is more influent on proteins than diffusion, they proposed a simple equation describing the coating time of proteins that I adapted in order to take into account the steric exclusion (in the case of non-charged species):

$$t_c = \frac{\Gamma_0 l}{500 N_A (1 - \lambda) h u_c c_0} \quad (4.23)$$

However, this equation no longer functions if the pressure-driven flow is too low compared to the displacements induced by the Brownian diffusion. It is also not valid if the protein solution is injected only in one of the microchannels. I measured the change of conductance of 60 μM BSA transport from microchannel A-C to B-D via the nanoslit, when applying pressure difference ranging from $\Delta P = -400$ mbar to $\Delta P = 400$ mbar. As presented in figure 4.7, a positive induced flow increased the surface concentration, and

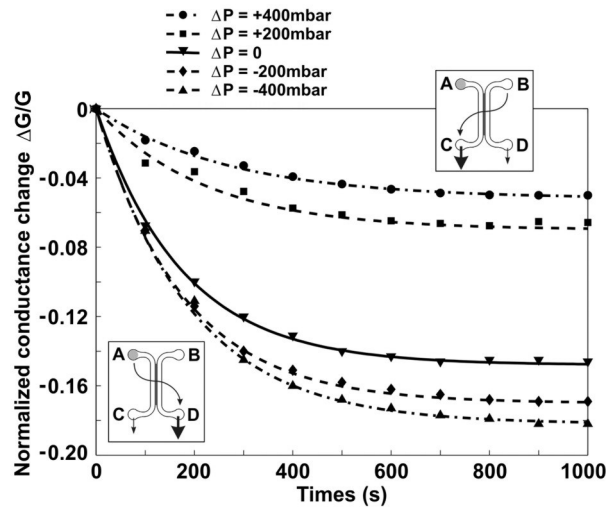


Figure 4.7: Evolution of the normalized conductance change with time for different differential pressures. The time constant of the adsorption phenomena increases or decreases when applying a negative or positive differential pressure $\Delta P = P_C - P_D$. 60 μM BSA in PBS solution (with pH of 4.9 corresponding to the isoelectric point of BSA) are injected in the first microchannel A-C.

4. ELECTRICAL DETECTION OF PROTEINS KINETICS IN NANOCONFINEMENTS

in an opposite way, a counter-flow decreased this surface concentration, resulting in a change of the nanoslit conductance.

A simple explanation is found in the change of the protein concentration profile across the nanoslit. In the no-flow case ($\Delta P=0$), the non-charged protein concentration profile is a linear profile starting from the concentration at the nanoslit entry ($c=c_0(1-\lambda)$), and the concentration value at the output of the nanoslit ($c=0$). When adding a positive pressure-driven flow across the nanoslit, the protein concentration profile is changed giving a higher quantity of proteins inside the nanoslit, leading to a stronger decrease of the electrical conductance. The opposite effect is observed for a negative pressure-driven flow. The concentration profile under similar conditions will be measured and studied in the section 5.4 of the next chapter with a single molecule detection system.

Effect of pH and ionic strength variations

The adsorption experiment was repeated for various values of pH, and for various ionic concentrations of PBS solution. Figure 4.8 shows the normalized conductance change of the nanoslit when 600 μM BSA proteins are injected in the system and have adsorbed on the nanoslit walls, as a function of the pH of the PBS solution. The points are representing the measurements and in order to plot equation 4.18, various parameters have been measured or are taken from the literature: the effective charge of BSA as a function of pH has been taken from nuclear magnetic resonance (NMR) measurements of Böhme *et al.*¹⁰³. The initial surface density was measured to be $\sigma_0 = -1.4 \cdot 10^{-2} \text{ C/m}^2$ using the second term of equation 4.14, which is very close with the value $\sigma_0 = -2.5 \cdot 10^{-2} \text{ C/m}^2$ reported by Schoch *et al.*¹⁰⁸. The ions' mobility $\mu_{Na} = 5.19 \cdot 10^{-8} \text{ m}^2 \text{V}^{-1} \text{s}^{-1}$ and $\mu_{Cl} = 7.91 \cdot 10^{-8} \text{ m}^2 \text{V}^{-1} \text{s}^{-1}$ were found in the literature¹³⁵ and an average value $\mu_{\pm} = 6.5 \cdot 10^{-8} \text{ m}^2 \text{V}^{-1} \text{s}^{-1}$ was used for all values of pH in order to avoid singularities.

The BSA surface coverage as a function of pH, $\Gamma(\text{pH})/\Gamma(\text{pI})$ has been taken from measurements of Clark *et al.*¹³⁵. They also reported that at high ionic strength, the surface coverage remains constant as a function of pH.

Figure 4.8 highlights that for solutions of high ionic concentrations, the changes of conductivity $\Delta G/G$ are almost independent of the pH, and the conductance of the nanoslit is mostly related to the apparent section of the nanoslit, and consequently to the number of proteins adsorbed on the nanoslit walls. The measurement of the normalized conductance change $\Delta G/G$ at high ionic concentrations can be used to detect the presence of biomolecules in the slit or the binding between species, as these phenomena are inducing changes of the apparent section of the nanoaperture. Schoch *et al.*⁶², recently

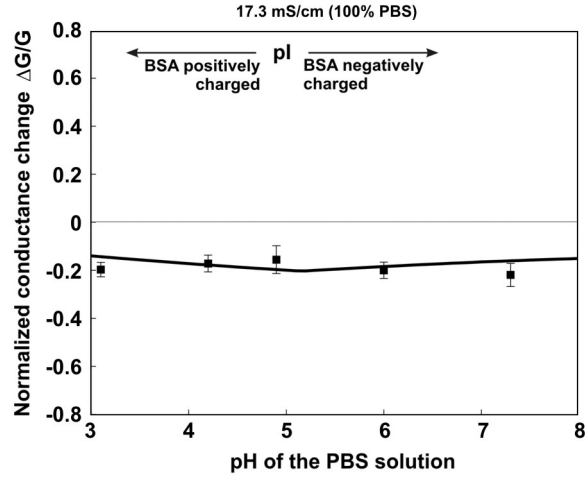


Figure 4.8: Normalized conductance change of the nanoslit as a function of the pH of the PBS solution when injecting 600 μM BSA. Points are the measurements and the line is plotted using equation 4.18, with n_p from Böhme *et al.*¹⁰³, $\Gamma(\text{pH})/\Gamma(\text{pI})$ from Clark *et al.*¹³⁵, $r_s=4$ nm, $\mu_{\pm}=6.5\cdot 10^{-8}$ $\text{m}^2\text{V}^{-1}\text{s}^{-1}$, $k_{on}=100$ $\text{M}^{-1}\text{s}^{-1}$, $k_{off}=0.002$ s^{-1} , $\sigma_0=-1.4\cdot 10^{-2}$ C/m^2 .

highlighted the possibility to detect binding between biotin and streptavidin in similar nanoslits. In a similar way, it can be imagined to attach a primary antibody to the nanoslit walls, to quantify the binding with a specific antigen and compare it with other species. This may lead to immunological applications based on electrical detection of label-free antigens.

4.5.2 Adsorption kinetics at low ionic strength

At low ionic strength, the conductance of the nanoslit is increasing due to the dominance of surface charge effects, described by the second term of equation 4.14. Figure 4.9 shows an adsorption experiment where a 600 μM BSA solution was injected in the nanofluidic system containing PBS solution diluted 100x in deionized water (1.37 mM NaCl) in order to reduce the ionic concentration. The kinetic behavior is different, however, from the expected adsorption kinetic curve because of a systemic overshoot followed by a slower decay to the equilibrium value $\Delta G/G$. Similar behaviour was also observed by Malmsten *et al.*^{112;136} with ellipsometry and by Wertz *et al.*¹¹⁵ with TIRF measurements. They explain this phenomenon by the occurrence of competitive spreading, in which initially adsorbed proteins undergo interfacial spreading, thereby occupying a larger interfacial area, and causing desorption of a fraction of the protein molecules. This is a possible explanation for the overshoot, assuming that high ionic strength solutions alter protein desorption due to competitive spreading.

4. ELECTRICAL DETECTION OF PROTEINS KINETICS IN NANOCONFINEMENTS

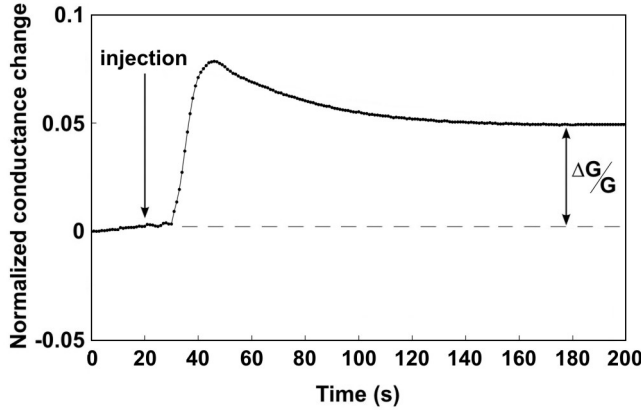


Figure 4.9: Nanoslit conductance response of BSA adsorbed at Pyrex surfaces when channels are filled with PBS diluted in deionized water (1%PBS) corrected to pH=6 by addition of HCl. The 600 μM BSA solution was injected at $t=20$ s and adsorbed on the nanoslit's walls. The value $\Delta G/G$ is measured when the normalized conductance change reaches an asymptote. The delay observed between injection and start of change is due to the time to reach the nanoslit.

Illustrations of figure 4.10 highlight that the effective surface charge may completely change as a function of adsorbed proteins. When the negatively charged surface is covered by adsorbed neutral proteins (at $\text{pH}=\text{pI}$), the effective surface charge tends to zero (figure 4.10b). If the proteins are charged (at $\text{pH}\neq\text{pI}$), each protein brings new counterions which participate in the surface conductance (figures 4.10c & d). Figure 4.10e presents the nanoslit conductance changes for solutions of low ionic concentrations. As for high ionic strength measurements (figure 4.8), the points are representing the measurements and the fitting line is plotted using equation 4.18. The same fitting parameters were used ($n_p(\text{pH})$ from Böhme *et al.*¹⁰³, $\sigma_0=-1.4\cdot 10^{-2}$ C/m², $\mu_{\pm}=6.5\cdot 10^{-8}$ m²V⁻¹s⁻¹ and $\Gamma(\text{pH})/\Gamma(\text{pI})$ from Clark *et al.*¹³⁵). Finally, Shibata *et al.*¹¹⁶ and Duncan *et al.*¹³⁴ highlighted an increase of the adsorption of proteins on surfaces when reducing the ionic strength of the solution. According to their measurements, the surface coverage $\Gamma(\text{pH})$ was increased by a factor 1.6 in our 1% PBS model relative to the 100% PBS model.

There are three different regimes which can be distinguished: i) close to the pI of the proteins, when BSA proteins are not charged and, the surface conductance change $\Delta G_S/G_S$ is low and tends to -1 when all initial surface charges are covered by globally uncharged molecules (according to equation 4.17). The model does not match the measurements when the pH is close to the pI because it is over-simplified and does not take into account the local inhomogeneity of the pH in the electrical double layer as reported by Van der Wouden *et al.*¹³⁷ and Bousse *et al.*¹³⁸. However the overall

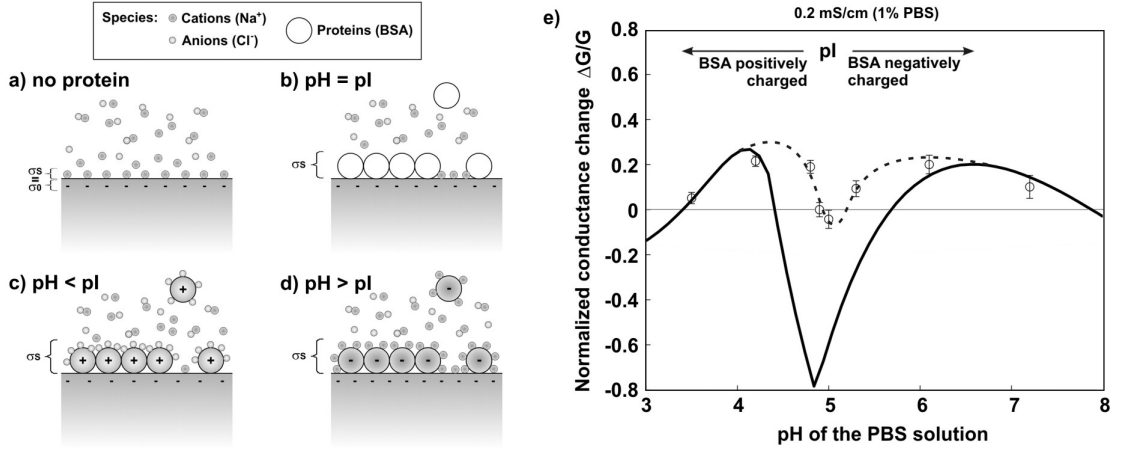


Figure 4.10: Typical glass-solution interface with its effective surface charge and its counterions layer for (a) no proteins, (b) neutral, (c) positively and (d) negatively charged absorbed proteins. (e) Normalized conductance change of the nanoslit as a function of the pH 1%PBS diluted in deionized water when injecting 600 μM BSA. Low ionic concentration solution is mainly dominated by nanoslit charge effects. The conductance difference due to protein charges and protein adsorption is more significant than for high ionic strength. Points are the measurements and line is plotted using equation 8, with n_p from Böhme *et al.*¹⁰³, $\Gamma(\text{pH})/\Gamma(\text{pI})$ from Clark *et al.*¹³⁵, $\Gamma(\text{pI})_{1\%PBS}/\Gamma(\text{pI})_{100\%PBS}=1.6$, $r_s=4$ nm, $\mu_{\pm}=6.5\cdot 10^{-8}$ $\text{m}^2\text{V}^{-1}\text{s}^{-1}$, $k_{on}=100$ $\text{M}^{-1}\text{s}^{-1}$, $k_{off}=0.002$ s^{-1} , $\sigma_0=-1.4\cdot 10^{-2}$ C/m^2 .

evolution of the model and experimental data are similar for values of the pH away from pI. ii) when going away from the pI value, the global number of charge of the proteins increases, which also increases the conductance of the nanoslit. iii) finally, when working with pH far away from pI, the surface coverage decreases too much and becomes the limiting factor, leading to a decrease in the conductance change.

4.6 Outlook and conclusions

A model was proposed to predict the biomolecular concentration in a nanochannel taking into account the steric exclusion as well as interactions of biomolecules with the surfaces and the exclusion-enrichment effect due to the electrical double layer and to the charge of the proteins.

Protein adsorption kinetics directly measured in a nanoslit were performed. In order to avoid electrical signal instability and derive, the electrical contacts were isolated from the fluidic channels by glueing intermediate apertures. It allowed us to perform quality measurements of high concentrated protein solutions. Another simple improvement that I strongly recommend for further lower concentrated protein experiments consists

4. ELECTRICAL DETECTION OF PROTEINS KINETICS IN NANOCONFINEMENTS

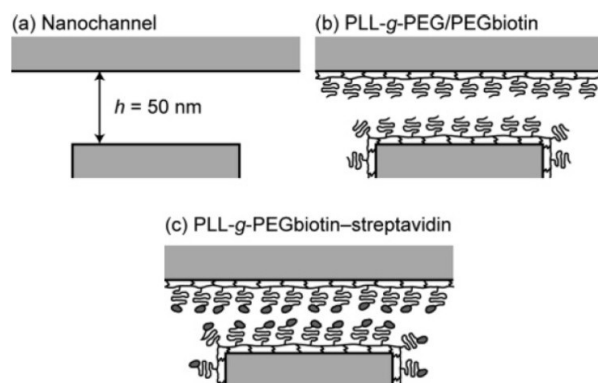


Figure 4.11: Schematic drawing of sequential surface modifications for streptavidin sensing. (a) A 50 nm high nanoslit in Pyrex before surface modification. (b) Channel after coating with PLL-g-PEG/PEGbiotin. (c) Final assembly after the streptavidin-biotin reaction, which binding can be sensed by a conductance change of the nanoslit. Adapted from Schoch *et al.*⁶².

of designing a third microchannel in parallel to the others, serving as a reference channel. The proteins would only be injected in the first channel, and a buffer solution would rinse the others. In that case, the first electrical conductance can be subtracted to the second one, leading to the removal of the signal derive and potentially to increase the sensitivity detection of low concentrated protein solutions.

The experiments performed in this chapter have shown that when the ionic strength of the solution is high, the conductance change is dominated by volume effects due to the adsorbed or bound proteins and the conductance is independent of the protein's charge. As illustrated in figure 4.11, Schoch *et al.* proposed to electrically detect binding kinetics between biotin and streptavidin. Applications in immunology and biomolecule detection requiring fast detection time could benefit from the development of a method based on similar conditions. Additionally, the adsorption and desorption kinetic parameters for a given protein-interaction condition can be easily deduced from the experiment.

When working with low ionic strength solutions, the sensitivity to protein charge was demonstrated and the behavior of the nanoslit conductance was described. The detection time of this device is however limited by the kinetics of the adsorption and desorption of molecules, as in the case with SPR immunosensors. However, the technique presented in this chapter has several advantages such as the simplicity of the measurements, the portability, low cost of production, suitability for fast multiplexing label-free detection of biomolecules on-chip and can become a powerful biophysical alternative in determining kinetic and equilibrium constants of molecular interactions.

CHAPTER

5

DIRECT MEASUREMENTS OF DIFFUSING SPECIES USING FCS

The following chapter describes the diffusion of charged proteins in nanometer-sized apertures with charged surfaces which has been investigated with fluorescence correlation spectroscopy (FCS). Based on a 2D multi-component diffusion model, key parameters like the number of molecules diffusing freely inside the nanochannel or interacting with the surfaces, together with the specific diffusion parameters, have been extracted. Different regimes of diffusion have been observed and described by a model which takes into account the steric exclusion, the reversible surface adsorption of the biomolecules, and the exclusion-enrichment effect due to the charge of the proteins and to the ionic strength of the solution. Conditions where the diffusion of proteins through nano confined spaces can be of the same magnitude as in the bulk were both predicted and experimentally verified.*

* Adapted from the journal articles:

N. F. Y. Durand, C. Dellagiacoia, R. Goetschmann, A. Bertsch, I. Märki, T. Lasser and P. Renaud, "Direct observation of transitions between surface-dominated and bulk diffusion regimes in nanochannels", *Analytical Chemistry*, **81**, 5407-5412, 2009.

N. F. Y. Durand, C. Dellagiacoia, R. Goetschmann, A. Bertsch, I. Märki, T. Lasser and P. Renaud, "Direct measurement of diffusing proteins in nanochannels using fluorescence correlation spectroscopy", *Procedia Chemistry*, **1**(1), 1343-1346, 2009.

5. DIRECT MEASUREMENTS OF DIFFUSING SPECIES USING FCS

5.1 Single molecule detection in nanochannels using FCS

Fluorescence Correlation Spectroscopy (FCS) is a very well-known and widely used microscopy method, allowing access across the fluctuation analysis of fluorescently-labeled single biomolecule's static and dynamic molecular parameters, such as the mean number of molecules and their diffusion behaviour^{139;140;141;142}. The classical FCS model for a free 3D diffusion of a single molecular component (ignoring the triplet population) is given by¹⁴³:

$$G(\tau) = \frac{1}{N} \left(1 - \frac{I_B}{I_{tot}}\right)^2 \frac{1}{1 + \frac{\tau}{\tau_D}} \sqrt{\frac{1}{1 + \omega^2 \frac{\tau}{\tau_D}}} + 1 \quad (5.1)$$

Where $G(\tau)$ is the autocorrelation function (ACF), N is the number of molecules in the measurement volume and τ_D the characteristic time of diffusion across the illuminated sampling volume. The factor $(1 - I_B/I_{tot})^2$ corrects for an uncorrelated background intensity I_B , with I_{tot} being the total intensity¹⁴⁴ including I_B . The aspect ratio ω of the sampling volume is defined as the ratio between the height $2r_z$ and the width $2r_{xy}$ of the FCS ellipsoidal detection volume ($\omega = r_z/r_{xy}$). In our nanochannel, the intersecting detection volume is approximated by a cylinder of small height compared to its diameter. Consequently $r_z \ll r_{xy}$ and ω tends to zero: the square-root term can then be neglected leading to the approximation of a 2D FCS model¹⁴⁰. Figure 5.1 shows the difference between the FCS detection volumes of freely 3D diffusing particles (figure 5.1a) and of confined 2D diffusing particles inside a nanochannel (figure 5.1b).

The Einstein theory for brownian movement⁹⁴, introduced in section 2.3.1, can be used to estimate the bulk diffusion coefficient D_{bulk} of spherical particles of radius r_s (and by extension of globular proteins) in aqueous solutions. The FCS measured diffusion time τ_{bulk} of freely diffusing biomolecules, is then related to the bulk diffusion coefficient D_{bulk} by¹³⁹:

$$\tau_{bulk} = \frac{r_{xy}^2}{4D_{bulk}} \quad (5.2)$$

As discussed in the previous chapter, in nanoconfined spaces, solute molecules undergo diffusion due to Brownian motion and can also adsorb at the channel walls due to the high surface to volume ratio, and thus the high probability to interact with a surface. Protein adsorption results in a consequent increase of the diffusion time through nanoconfined volume.

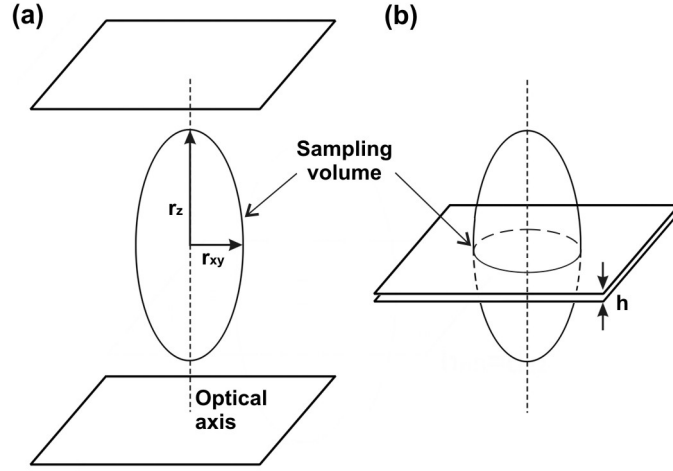


Figure 5.1: (a) FCS detection volume in the case of 3D freely diffusing biomolecules. (b) FCS detection volume of 2D confined diffusing molecules between two walls (when $h_{nC} \ll 2r_z$), such as in the case of the nanochannel. The ellipsoidal detection volume, of height $2r_z$ and width $2r_{xy}$, is approximated by a cylindrical volume of height h and radius r_{xy} in case b.

The total population of biomolecules diffusing through the nanochannel is composed of molecules which interact i -times with surfaces (with i ranging from 0 to n interactions).

I propose to express the effective diffusion time of the averaged population as a weighted arithmetic mean of the diffusion times of freely diffusing molecules in the bulk and at reversibly adsorbed molecules on the surfaces:

$$\tau_{eff} = \frac{\sum_{i=0}^n N_i \tau_i}{\sum_{i=0}^n N_i} \quad (5.3)$$

As FCS measurements are performed under a finite measurement time t_m , molecules which are remaining inside the detection volume during the measurement time lap will not be represented in the autocorrelation function. In order to correctly quantify the effective diffusion, t_m should be large enough to measure most different populations of proteins crossing the detection volume (all n -interacting populations).

5. DIRECT MEASUREMENTS OF DIFFUSING SPECIES USING FCS

In order to identify all of the n -interacting populations, the fitting of FCS measurements for different n values based on the following 2D multi-component model¹⁴⁰ was performed:

$$G(\tau) = \left(1 - \frac{I_B}{I_{tot}}\right)^2 \sum_{i=0}^n \left[\frac{N_i}{\left(\sum_{j=0}^n N_j\right)^2} \frac{1}{1 + \left(\frac{\tau}{\tau_i}\right)^{\alpha_i}} \right] + 1 \quad (5.4)$$

where coefficient α_i is a constant retention parameter, depending mainly on the geometry of the nanoconfinement. This phenomenological retention parameter takes into account the modified diffusion behavior of reversibly adsorbed particles. Best fittings of autocorrelation curves have allowed for the determination of α_i , which is an exponential term, in a similar way to the obstruction diffusion parameter, which is widely used in anomalous diffusion in biology^{145;146}. Due to the low concentration of charged biomolecules, interactions between particles have been neglected.

Interestingly, I have already obtained very good fits for $n=1$, meaning that 2 different populations of molecules can be distinguished: (a) the molecules that directly diffuse across the detection volume without any interaction ($i=0$) and (b) the molecules which interact only once with surfaces during the travel across the detection volume ($i=1$). Fits with higher n have resulted in $N_{i>1}$ tending to 0, meaning that in these specific conditions (depending on pH, ionic strength, surface charge, molecule conformity and charge, etc.), most of the biomolecules diffusing through the measurement volume interact only once or not at all.

The adaptation of equation 5.4 in these conditions leads to the following FCS model taking into account two different populations of particles: biomolecules diffusing freely through the detection volume ($i=0 \rightarrow N_{bulk}, \tau_{bulk}$) and biomolecules interacting once with the channel surfaces ($i=1 \rightarrow N_{surf}, \tau_{surf}$):

$$G(\tau) = \left(1 - \frac{I_B}{I_{tot}}\right)^2 \left[\frac{N_{bulk}}{(N_{bulk} + N_{surf})^2} \frac{1}{1 + \frac{\tau}{\tau_{bulk}}} + \frac{N_{surf}}{(N_{bulk} + N_{surf})^2} \frac{1}{1 + \left(\frac{\tau}{\tau_{surf}}\right)^{\alpha}} \right] + 1 \quad (5.5)$$

Equation 5.3 with $n=1$ is also simplified to:

$$\tau_{eff} = \frac{N_{bulk}\tau_{bulk} + N_{surf}\tau_{surf}}{N_{bulk} + N_{surf}} \quad (5.6)$$

The averaged time of interaction τ_{surf} of biomolecules with surfaces is expressed by the Langmuir isotherm model^{147;148}:

$$\tau_{surf} = \frac{1}{k_{off}} \quad (5.7)$$

Finally, the effective diffusion coefficient D_{eff} is related to τ_{eff} as for equation 5.2:

$$D_{eff} = \frac{r_{xy}^2}{4\tau_{eff}} \quad (5.8)$$

This gives a first clue for explaining why in nanoconfinements, the apparent diffusion coefficient may be strongly decreased compared to its bulk value^{149;150;29}. This phenomena will be discussed in greater detail in chapter 6.

5.2 Materials and methods

As explained in chapter 3, the solutions containing proteins are injected into the microchannels through the inlets. The liquids are driven by air aspiration controlled by using air-pressure regulators (Bellofram Corp., Newell, WV) from 0 to -800mbar.

The experimental set-up is depicted in figure 3.7a, and the nanochannel-device used in the experiment consists of 2 microchannels crosslinked by a thin nanochannel (height $h_{nC}=50$ nm, width $w=10$ μm , length $l_{nC}=30$ μm). Solutions containing fluorescently labeled proteins are injected in both microchannels and measurements are performed as soon as the system is in equilibrium, meaning that all channels are completely filled. External, negative pressure applied to the outlet ports allow for precise, fine tuning of the flows in each microchannel as well as in the nanochannel.

To investigate and characterize the hindered diffusion of proteins, I used wheat germ agglutinin proteins labeled with Alexa Fluor® 633 (WGA, from Molecular Probes). WGA has a molecular mass of 38 kDa, an isoelectric point (pI) around 4, and a free diffusion coefficient in water⁸⁴ $D_{bulk}=7.6(\pm 0.3)\cdot 10^{-11}$ m^2/s .

These WGA proteins have been added to potassium chloride (KCl) solutions, which have been prepared with different dilutions (10^{-5} M to 10^{-1} M) by addition of deionized water (18M Ω -cm). The concentration of the WGA proteins is 50 nM in all prepared solutions, which were adjusted to pH=7 by adding a small amount of HCl. For all experiments, no pre-treatment was performed on the chip in which the solutions have been directly injected. All solutions were prepared and degassed before use at room temperature $T=25^\circ\text{C}$.

5. DIRECT MEASUREMENTS OF DIFFUSING SPECIES USING FCS

5.3 Results and discussion

A series of experiments were carried out to evaluate the number of molecules and the diffusion time of the WGA proteins at two different locations: i) inside the reservoirs for measuring the bulk values (away from chip surfaces), and ii) inside the nanoconfinements for measuring the diffusion parameters inside the channel. After filling the microchannels, the solution entered the nanochannel by capillarity, resulting in a slow change of fluorescence intensity inside the nanochannel. All measurements were started once the fluorescence intensity reached a steady-state.

5.3.1 3D diffusion of WGA

As illustrated in figure 5.1a, the FCS detection volume in the bulk is an ellipsoid with an equatorial radii $r_{xy}=420$ nm and a polar radius $r_z=4$ μm . The number of molecules present in this volume N_{3D} is given by:

$$N_{3D} = 1000 \frac{4}{3} \pi N_A r_{xy}^2 r_z c_0 \quad (5.9)$$

For a $c_0=50$ nM concentrated solution of WGA proteins, $N_{3D}=178$ molecules is found, which corresponds very well with the measured value of 180 ± 2 molecules measured in the chip's reservoirs.

With the same fluorescence fluctuation measurements, a diffusion time of $\tau_{bulk}=0.6 \pm 0.02$ ms was obtained by fitting the experimental data to equation 5.1, as this bulk experiment corresponds to standard 3D free diffusion of a single component. From this value of τ_{bulk} , the diffusion coefficient $D_{bulk}=7.35(\pm 0.3) \cdot 10^{-11}$ m²/s was obtained from equation 5.8 with $r_{xy}=420$ nm, which corresponds to the radius of the detection area. This value is very close to the diffusion coefficient of WGA in water reported by Munson *et al.*⁸⁴ of $D_{bulk}=7.6(\pm 0.3) \cdot 10^{-11}$ m²/s.

5.3.2 Exclusion of proteins from the nanochannel at low ionic strength

As illustrated in figure 5.1b, the detection volume in a nanoconfinement is the intersection of the FCS ellipsoid measurement volume and the inner volume of the nanochannel. This volume is approximated by a cylinder of radius r_{ry} and the nanochannel's height

h. The expected number of molecules present in the detection volume for a given concentration c_0 is:

$$N_{nS} = 1000\pi N_A r_{xy}^2 h c_0 \Phi_{nS} \quad (5.10)$$

with Φ_{nS} the equilibrium partitioning coefficient for solute concentration between inside and outside a nanochannel defined in equation 4.12. From best fits with 50 nM WGA experiments at high ionic strength ($c_i=3.6 \cdot 10^{-1}$ M), I obtained $N_{nS}=6$ molecules in the detection volume (with $\Phi_{nS}=7$). Interestingly, in this case $\Phi_{nS}>1$, meaning there is an increase of the nanochannel concentration compared to the bulk value c_0 . As the steric effect always tends to decrease the nanoconfinement concentration, and as we are under an exclusion regime which also tends to reduce Φ_{nS} , it means that the nanochannel concentration is important because of the adsorption of proteins on surfaces.

The curve in figure 5.2 shows the mean fluorescent intensity I_{tot} measured in different ionic conditions in the 50 nm high nanochannel. Pyrex surfaces in contact with aqueous solutions are negatively charged, which electrostatically repulses negatively charged WGA proteins (pH=7 \gg pI=4). A strong decrease of I_{tot} is observed when increasing the EDL by reducing the ionic concentration in the nanochannel, which is coherent with equation 4.12 and with results of Plecis *et al.*¹⁰⁶. In figure 5.2, equation 4.12 is

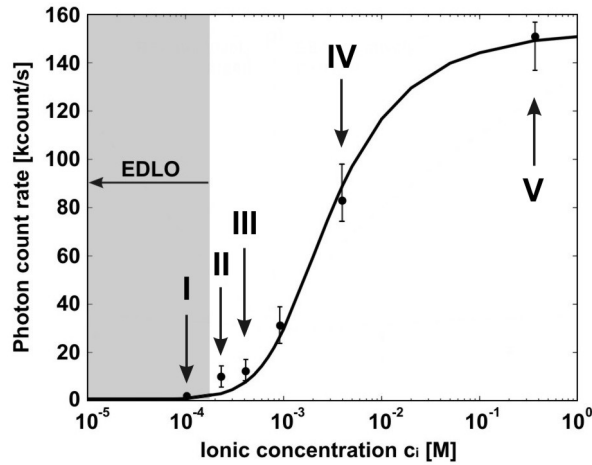


Figure 5.2: Measurements of fluorescent proteins showing photon count rate of 50 nM WGA at different ionic strengths c_i in a 50 nm high nanochannel. The dots are experimental measurements whereas the line is a fitting obtained with equation 4.12. Pyrex surfaces are negatively charged, which excludes negatively charged WGA proteins from the nanochannel. When electrical double layer overlap (EDLO) occurs, a total exclusion of proteins from the nanochannel can be seen. Cases I to V correspond to the schematics in figure 5.4.

5. DIRECT MEASUREMENTS OF DIFFUSING SPECIES USING FCS

fitted on the experimental data points with $r_p=4$ nm, $q=-e$ and $\zeta=30\cdot 10^{-3}\cdot \log(c_i)$ as measured by Kosmulski *et al.*¹⁵¹. By best fitting all measurements, I extracted $K=k_{on}/k_{off}=7.28\cdot 10^3$ M⁻¹. For values of the ionic concentration lower than 10^{-4} M, the EDL overlap (EDLO) is observed; only the uncorrelated background intensity was measured, which corresponds to the exclusion of the proteins from the nanochannel.

5.3.3 Confined diffusion of negatively charged proteins

The autocorrelation curves obtained when WGA proteins are diffusing inside the nanochannel for different values of the ionic strength of the solution are presented in figure 5.3. As all experiments are performed with identical nanochannels, at a constant value of pH=7 and using solutions of 50 nM WGA proteins, while ionic concentration is changed, equation 5.5 can be used to fit each set of experimental data points with τ_{bulk} , τ_{surf} and α being constant parameters. The values of $\tau_{bulk}=0.6(\pm 0.02)$ ms were measured independently as presented in section 5.3.1 and $\tau_{surf}=10(\pm 2)$ ms and $\alpha=0.45\pm 0.1$ were obtained from fitting of all FCS measurements inside the nanochannel. All other parameters being kept constant in equation 5.5, the fit of the data to the autocorrelation function allows the estimation of the values of N_{bulk} and N_{surf} , which correspond to the average number of WGA proteins diffusing freely or interacting with the nanochannel walls, respectively. A good agreement between the measurements and equation 5.5 was obtained in all cases, as shown in figure 5.3 for different values of the ionic concentration.

This experiment has highlighted several different diffusion behaviors in function of the ionic strength of the solution. Table 5.1 summarizes the typical values of 50 nM WGA proteins diffusing in a 50 nm high nanochannel in function of these different cases. As depicted in figure 5.4a, there is an exclusion of the proteins from the nanochannel for solutions with an ionic strength lower than 10^{-4} M (there is an overlap of the EDL).

Case	c_i (M)	N_{bulk}	N_{surf}	I_{tot} (kHz)	D_{eff} (m ² /s)	Φ_{nS}
I	$1.0\pm 0.3\cdot 10^{-4}$	0 ± 0.1	0 ± 0.1	$I_B=13\pm 2$	-	0
II	$2.3\pm 0.2\cdot 10^{-4}$	0 ± 0.1	0.8 ± 0.1	19 ± 2	$7.6\cdot 10^{-12}$	1
III	$4.1\pm 0.1\cdot 10^{-4}$	0.9 ± 0.1	0.1 ± 0.1	25 ± 2	$2.7\cdot 10^{-11}$	1.2
IV	$9.2\pm 0.05\cdot 10^{-4}$	0.5 ± 0.1	0.6 ± 0.1	46 ± 2	$5.01\cdot 10^{-12}$	1.3
V	$3.6\pm 0.01\cdot 10^{-1}$	0.2 ± 0.1	5.4 ± 0.8	165 ± 5	$4.4\cdot 10^{-12}$	7

Table 5.1: Typical values of 50 nM WGA proteins diffusing in a 50 nm high nanochannel, at different ionic strengths at pH=7 (corresponding to the main cases illustrated in figure 5.4). c_i , N_{bulk} , N_{surf} and I_{tot} are extracted from measurements. D_{eff} and Φ_{nS} are calculated from equation 5.8 and 4.12. Parameters were extracted using $\tau_{bulk}=0.6$ ms, $\tau_{surf}=10$ ms and $\alpha=0.45$ as fixed parameters.

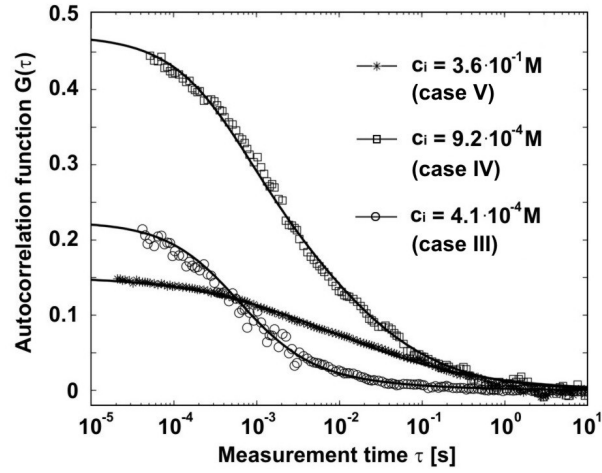


Figure 5.3: Measurements of fluorescent proteins showing autocorrelation functions of fluorescence fluctuations of 38 kDa wheat germ agglutinin with Alexa Fluor® 633 in a 50 nm high nanochannel for solutions of different ionic concentration at pH=7. Fitting using equation 5.5 with parameters of table 5.1.

Figure 5.4b shows that when increasing further the ionic strength to a case where there is not yet an overlap of the EDL, the small number of proteins which enter the nanochannel are not confined to the center by electrostatic forces and consequently interact with the surfaces. In that case, the autocorrelation functions measured were similar to the ones measured for high ionic strength. For values of the ionic strength close to $4 \cdot 10^{-4}$ M, the number of molecules interacting with the walls is close to zero. As presented in figure 5.4c, the proteins are maintained away from the channel walls by the large dimension of the EDL. However, as there is no EDL overlap, a small, but significant number of proteins enter the nanochannel. When the ionic strength of the solution increases from $4 \cdot 10^{-4}$ M to 10^{-1} M, the number of proteins present in the nanochannel increases strongly. The electrostatic repulsion of the negatively charged WGA proteins due to EDL is decreasing. As depicted in figure 5.4d, the number of proteins reaching the walls increases while the number of molecules diffusing freely in the bulk of the nanochannel decreases. Finally, at high ionic strength (for $c_i > 10^{-1}$ M) a large number of proteins are present in the nanochannel and most of them interact with the walls (N_{bulk} is close to zero). This situation is schematically described in figure 5.4e: As the ionic concentration is high, the EDL is small and does not prevent the interaction between the proteins and the walls.

Figures 5.5a and 5.5b show the evolution of respectively the extracted values N_{bulk} and N_{surf} , and of the effective times of diffusion τ_{eff} which have been calculated

5. DIRECT MEASUREMENTS OF DIFFUSING SPECIES USING FCS

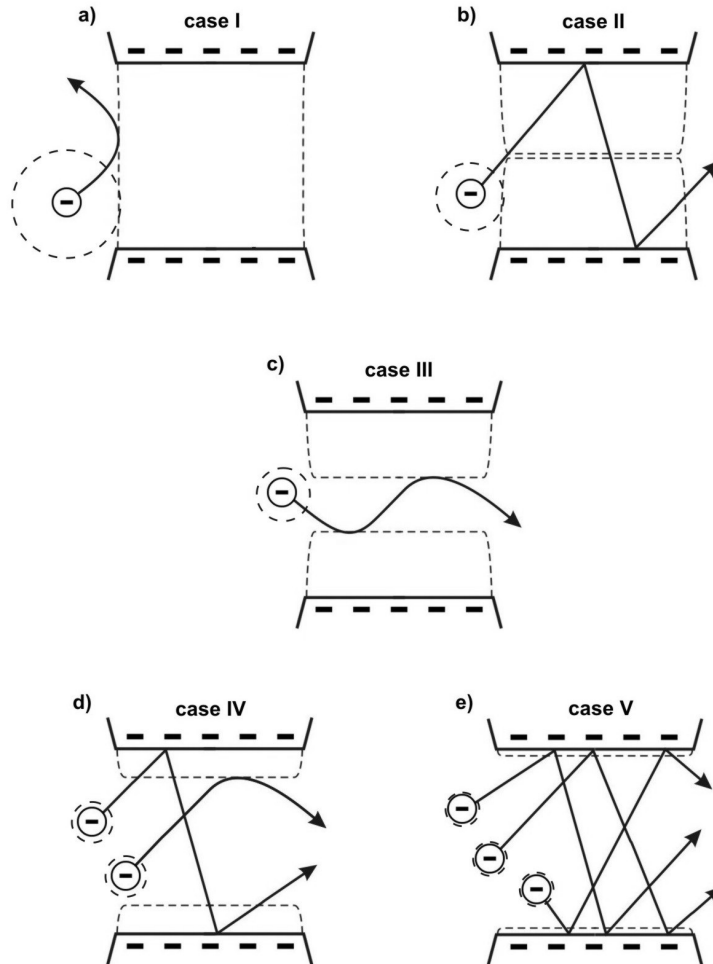


Figure 5.4: Schematics of the typical behavior of negatively charged biomolecules inside a nanochannel with negatively charged surfaces, at different ionic strengths. Our model is based on 2 different populations of molecules: the molecules which never touch the pore walls (N_{bulk}, τ_{bulk}) and those which adsorb on the surfaces and get retarded (N_{surf}, τ_{surf}). (a) at low ionic concentration, the channel is closed by the electrical double layer (EDL, represented by a dashed line) and no negatively charged molecules enter in the channel. (b) When increasing the ionic strength, very few molecules enter and interact with the surfaces. (c) When the channel is sufficiently open, most of the molecules do not interact with the surfaces ($N_{surf} \rightarrow 0$). (d) when the ionic concentration increases, the EDL decreases and some molecules do interact with the surfaces again. (e) Finally, at high ionic concentrations, the EDL is thin and does not prevent most molecules to interact with the surfaces ($N_{bulk} \rightarrow 0$).

5.4 Gradient profile across a nanochannel

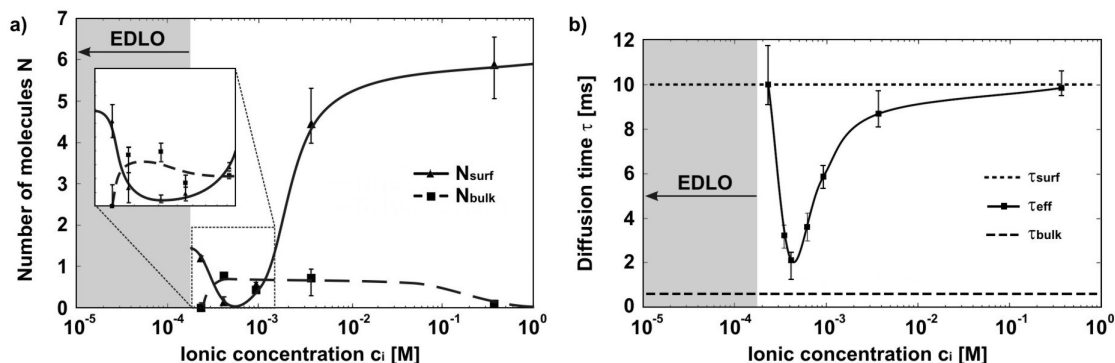


Figure 5.5: WGA proteins diffusing in a 50 nm high nanochannel, at different ionic strengths. (a) Number of *bulk* and *surf* molecules, obtained by fitting the autocorrelation functions with equation 5.5, using the fixed parameters $\tau_{bulk}=0.6$ ms, $\tau_{surf}=10$ ms and $\alpha=0.45$. Experimental data were performed at pH=7 and are represented by marks. (b) Effective diffusion times for WGA proteins in a 50 nm high nanochannel at different ionic strengths. Marks represent the effective diffusion times calculated with equation 5.6 from measurements of figure 5.5. All lines are plotted by interpolating the data in order to guide the eye of the reader.

with equation 5.6, as a function of the ionic strength of the solution. As expected, at very low ionic strength, no fluorescent protein was detected in the nanochannel. After increasing slightly the ionic concentration, a few proteins enter the nanochannel; they have a diffusion time close to τ_{surf} and correspond to case II (figure 5.4b). When going on increasing the ionic strength, the effective time of diffusion decreases until reaching a minimal value close to τ_{bulk} . This corresponds to the case III depicted in figure 5.4c where the proteins no longer reach the walls of the nanochannel due to size of the EDL, and resulting in a population exclusively composed of freely diffusing molecules compared to interacting ones. In such specific ionic conditions, the effective diffusion of proteins is almost as fast as in the bulk. Finally, at higher ionic strengths, τ_{eff} increases until getting a value close to τ_{surf} , just as all proteins interact with the walls of the nanochannel due to the limited extension of the EDL and the large surface to volume ratio of the channel (case V, figure 5.4e).

5.4 Gradient profile across a nanochannel

5.4.1 Simple diffusive case

Theoretical models describing the concentration profile of proteins inside large channels have been extensively studied for the purpose of membrane science and interested readers are invited to have a look at the book by Cussler¹⁵². In this section, in order

5. DIRECT MEASUREMENTS OF DIFFUSING SPECIES USING FCS

to verify the validity of the standard theoretical models, the transport of negatively-charged proteins in liquid-filled nanometer-sized apertures with negatively-charged surfaces based on both gradient of diffusion and convective flow is investigated with the use of fluorescence correlation spectroscopy. FCS is a perfect tool for this purpose because of its small lateral detection area ($r_{xy}=420$ nm) compared to the nanochannel length ($l_{nC}=30$ μm), and thus can be considered as punctual measurements along the nanochannel length. As previously highlighted, the measured fluctuations of fluorescence allow the evaluation of the diffusion of molecules directly inside the nanochannel, as well as their concentration in the measured focal volume.

The steady diffusion across a nanochannel is schematically sketched in figure 5.6a. The channel initially contains a uniform concentration of solute $c=0$. At some time, the concentration in the first microchannel is increased by injecting the proteins solution at a concentration c_0 . Assuming that output microchannel concentration remains at zero (by rinsing with initial solution for example), a steady-state concentration profile is obtained when proteins have crossed the channel. Assuming no convective flow and using boundary conditions ($x=0 \rightarrow c=c_0\Phi_{nC}$ and $x=l_{nC} \rightarrow c=0$), the concentration profile inside the nanochannel can be expressed as:

$$c(x) = c_0\Phi_{nC} \left(1 - \frac{x}{l_{nC}}\right) \quad (5.11)$$

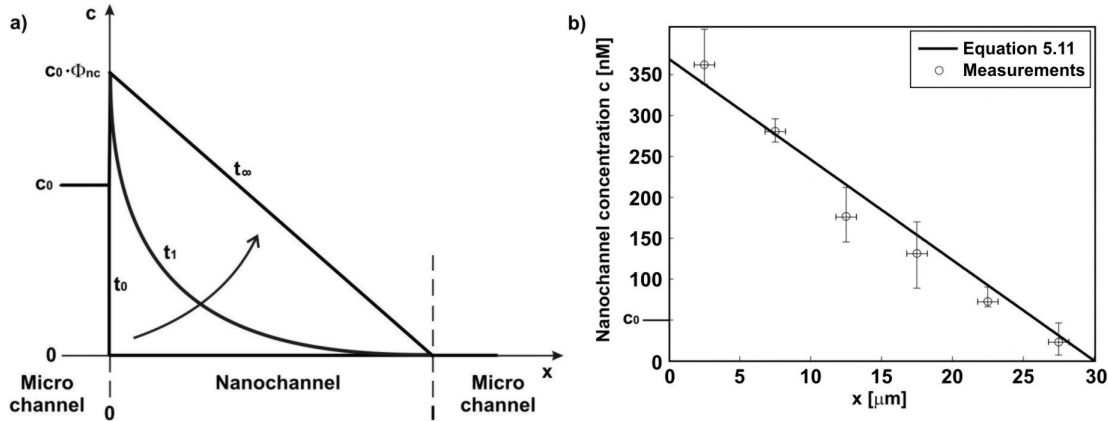


Figure 5.6: (a) Principle and (b) measured concentration profile of WGA proteins diffusing from a first microchannel (filled with 50 nM WGA proteins in PBS at pH=7) through a 50 nm high nanochannel of length $l_{nC}=30$ μm into another microchannel filled only with PBS. No convective flow is applied across the nanochannel. The line calculation is based on equation 5.11 with $\Phi_{nC}=7$. The steady-state concentration profile is independent of the diffusion coefficient.

5.4 Gradient profile across a nanochannel

As presented in figure 5.6b, the concentration gradient of 50 nM WGA proteins was measured directly inside the nanochannel. The same pressure of 100 mbar were applied in both microchannels in order that no convective flow ($u_c=0$) is induced across the nanochannel, but solutions are renewed in both microchannels for remaining concentration levels to c_0 , respectively 0. The measurements were performed at high ionic strength (for $c_i=10^{-1}$ M) in order to avoid interactions with the EDL, and at pH=7 in order to compare results with those in the previous section. The measurements fit very well equation 5.11, highlighting that the standard diffusion theory is also valid in nanoconfinements. The steric exclusion, the presence of reversibly adsorbed molecules on surfaces, and the exclusion-enrichment effect due to interaction with the electrical double layer, were all taken into account in this model and they do not appear to influence the concentration profile. As expected, these effects directly change the initial concentration $c(x=0)=c_0\Phi_{nS}$ which is strongly increased because of the adsorption of the proteins on surfaces. Without any convective flow, this diffusion case is independent of the value of the effective diffusion coefficient.

The theoretical model was plotted using equation 5.11 with $\Phi_{nS}=7$ as measured in experiments of section 5.3.2 in high ionic strength conditions. Using equation 4.13 with $r_p=4$ nm and $k_{off}=1/\tau_{surf}=100$ s $^{-1}$, I extracted $k_{on}=7.28\cdot 10^5$ M $^{-1}$ s $^{-1}$. In comparison with values obtained with BSA proteins interacting with surfaces (see chapter 4, section 4.5.1) where I extracted $k_{on}=100$ M $^{-1}$ s $^{-1}$ and $k_{off}=0.002$ s $^{-1}$, WGA proteins have a higher k_{on} value, meaning a higher number of binding events per unit of time. Similarly, the WGA proteins have a value for the dissociation constant k_{off} , that is higher by 5 orders of magnitude, meaning a higher number of dissociation events per unit of time, and that WGA proteins will unbind very quickly compared to BSA proteins that have a very sticky reputation with surfaces.

5.4.2 Diffusion and convection

The same experiment was conducted under different pressure-driven flow conditions. In order to measure the correct concentration of molecules, the FCS model had to be modified taking into account the convective flow. In high ionic strength solutions, the population of *bulk* molecules is tending to 0 and equation 5.5 is reduced to *surf*

5. DIRECT MEASUREMENTS OF DIFFUSING SPECIES USING FCS

population. The proposed FCS model including the convective flow in an exponential term is:

$$G(\tau) = \left(1 - \frac{I_B}{I_{tot}}\right)^2 \left[\frac{1}{N_{surf}} \cdot \frac{1}{1 + \left(\frac{\tau}{\tau_{surf}}\right)^\alpha} \cdot e \left[-\left(\frac{\tau}{\tau_f}\right)^2 \left(1 + \left(\frac{\tau}{\tau_{surf}}\right)^\alpha\right)^{-1} \right] \right] + 1 \quad (5.12)$$

where $\tau_f = \omega_{xy}/u_c$ is the average residence time if there is only a flow (no diffusion).

When adding an external pressure difference ΔP , the protein transport is still dominated by diffusion but also by the convective flow u_c induced by the external pressure. The concentration profile along the nanochannel can be deduced by writing a mass balance taking into account both diffusion and convective flow $u_c \neq 0$:

$$\frac{\partial c}{\partial t} = D_{eff} \frac{\partial^2 c}{\partial x^2} - u_c \frac{\partial c}{\partial x} = 0 \quad (5.13)$$

By integrating equation 5.13 and using the boundary conditions $x=0 \rightarrow c=c_0\Phi_{nC}$ and $x=l_{nC} \rightarrow c=0$, the steady-state concentration profile inside the nanochannel is calculated to be:

$$c(x) = c_0\Phi_{nC} \frac{\left(e^{\frac{u_c}{D_{eff}}x} - e^{\frac{u_c}{D_{eff}}l_{nC}} \right)}{\left(1 - e^{\frac{u_c}{D_{eff}}l_{nC}} \right)} \quad (5.14)$$

Figures 5.7a and b show the concentration profile of 50nM WGA inside a nanochannel, when external pressure differences of $\Delta P = \pm 100$ mbar are applied. This roughly corresponds to a constant convective flow inside the nanochannel of $u_c = 500$ nm/s, and $u_c = -500$ nm/s, respectively. Line plots were calculated based on equation 5.14 using the effective diffusion coefficient $D_{eff} = 4.4 \cdot 10^{-12}$ m²/s measured in the previous section in similar ionic strength conditions (see table 5.1). $\Phi_{nS} = 14$ was the only parameter to be tuned in order to get the best fit.

Interestingly, under a positive convective flow (figure 5.7a), the value Φ_{nS} is increasing (in comparison with the value $\Phi_{nS} = 7$ obtained in no-flow conditions), when it would be expected that it remains constant. The steric effect should still be present with flow, and at high ionic strength, the exclusion effect is negligible. A first possible explanation for this phenomenon is that the convective flow is changing the adsorption and/or desorption kinetic parameters k_{on} and k_{off} . As introduced in section 2.2.2, the flow inside the nanochannel is parabolic in the z-direction and thus should be

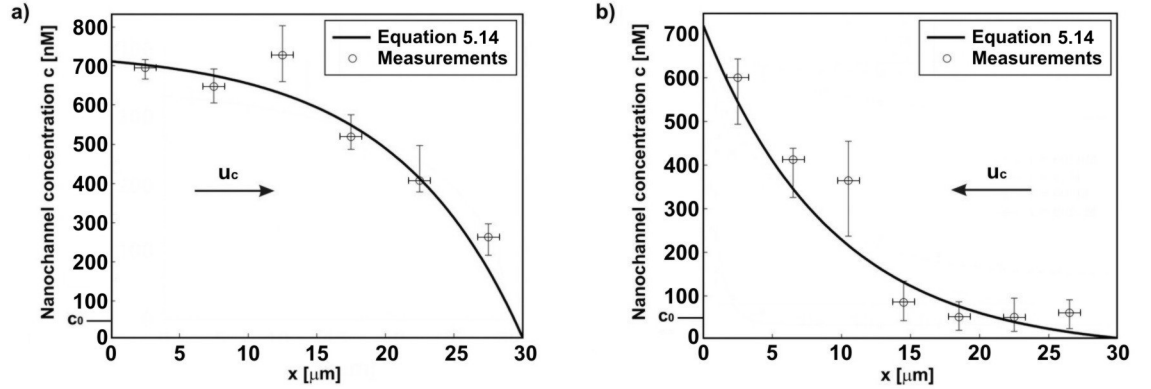


Figure 5.7: Concentration profile of WGA proteins diffusing from a first microchannel (filled with 50 nM WGA proteins in PBS at pH=7) through a 50 nm high nanochannel of length $l_{nC}=30 \mu\text{m}$ into another microchannel filled only with PBS. An external pressure of ± 100 mbar is applied, corresponding to (a) $u_c=500$ nm/s and (b) $u_c=-500$ nm/s. Marks are measurements ($\tau_f=0.84$ s), and lines are calculated using equation 5.14 with $D_{eff}=4.4\cdot 10^{-12}$ m²/s. Φ_{nS} were adjusted in order to fit the measurements.

negligible close to the surfaces, but it can perhaps be strong enough to increase k_{on} and/or decrease k_{off} , leading to an increase of the surface concentration. I extracted from measurements of figure 5.7 the equilibrium constant $K=k_{on}/k_{off}=1.5\cdot 10^4$ M⁻¹, which would mean that convective flow increased the number of binding events per unit of time, or that WGA molecules were adsorbed stronger to surfaces.

As highlighted by Green *et al.*¹⁵³, the rate of adsorption is dependent on two factors: mass transport and intrinsic kinetics. They observed that the binding rate of a protein to a surface often initially reflects the mass transfer characteristics of the protein components under prevailing flow conditions¹⁵⁴. By varying the flow rate, mass transport limitation can be identified since mass transport is influenced by flow rate, whereas the intrinsic kinetics are independent of the flow rate¹⁵⁵.

Another possible explanation is found in a potential streaming effect due to the flow in the lateral microchannels. However, boundary effects should be present, and this is not the case in measurements of figure 5.7a.

5.5 Outlook and conclusions

In this chapter, I have demonstrated that hindered protein concentration and diffusion can be measured directly inside a nanochannel with an FCS measurement unit. FCS autocorrelation functions have been used to identify different populations of molecules

5. DIRECT MEASUREMENTS OF DIFFUSING SPECIES USING FCS

diffusing in the nanoconfinement. The proposed model allowed for the estimation of the number of molecules diffusing freely inside the nanochannel and the number of molecules interacting with the surfaces. The measurements performed at different ionic strengths showed different regimes of diffusion and highlighted that for a specific EDL thickness, the diffusion of proteins through a nanochannel can be almost as high as in the bulk. Finally, the concentration gradients for different diffusion and convection conditions have been measured and characterized, showing that theories describing diffusion at the macroscale are also valid in nanoconfinements in high ionic strength conditions.

Many future complementary experiments can bring deeper understanding of molecular transport in nanofluidics. For example, the transport of neutral and positively-charged proteins through nanochannels should be performed in order to validate our model in these conditions. It would also make sense to investigate different types of proteins, with different binding and dissociation constants. Changing the nanochannel height would also bring complementary interesting data.

From the biomicroscopy point of view, a promising experiment is the triplet-state analysis of the protein-surface interaction of the experiment conducted in section 5.3.3. For example, one can also expect to observe a change in the triplet-state in function of the ionic strength.

Models presented in this thesis to predict protein concentration and diffusion in nanoconfined spaces can be easily used to get a good idea of molecular transport in order to design and develop future nanofluidic devices for biological and biomedical applications.

CHAPTER

6

APPARENT DIFFUSION MEASUREMENT USING STEADY-STATE DISPERSION

In this chapter a novel method to measure apparent diffusion coefficients of fluorescently labeled molecules inside a nanofluidic system is presented. Based on the decrease of the apparent diffusion of biomolecules in confined spaces, the binding affinity between proteins and surfaces is directly measured. Furthermore, theoretical and experimental studies of nanofluidic channels as potential biosensors for measuring rapid protein complex formation is presented.*

* Adapted from the journal articles:

N. F. Y. Durand, A. Bertsch, M. Todorova and P. Renaud, "Direct measurement of effective diffusion coefficients in nanochannels using steady-state dispersion effects", *Applied Physics Letters*, **91**, 203106, 2007.

N.F.Y. Durand, E. Saveriades and P. Renaud, "Detecting proteins complex formation using steady-state diffusion in a nanochannel", *Analytical Bioanalytical Chemistry*, **394**(2), 421-425, 2009.

6. APPARENT DIFFUSION MEASUREMENT USING STEADY-STATE DISPERSION

6.1 Apparent diffusion in nanoconfinements

In the first simple experiment described in chapter 1 and depicted in figure 1.15, the extracted value for the diffusion coefficient of the WGA protein was in the order of magnitude of 10^{-14} m²/s or below. This value was extracted from the advance of the fluorescent front, which was mostly limited by the pressure-driven flow that was applied from the external reservoirs, and not by the diffusion caused by the concentration gradient. However, this diffusion coefficient value is in contradiction to the one obtained with fluorescence correlation spectroscopy in the previous chapter (see table 5.1) where I measured $D_{eff}=4.7 \cdot 10^{-12}$ m²/s in similar ionic conditions.

Both are correct values and their strong difference can be explained by the way of interpreting their meaning: in the case of the FCS measurements, the "effective diffusion coefficient" D_{eff} is taking into account the complete trip of molecules, but in the case of the top-view fluorescence measurements, only the lateral displacement is taken into account even if the molecules are also displacing in the z-direction. Then, they seem to diffuse slower. I named this lower diffusion coefficient the "apparent diffusion coefficient" D_{app} .

The paper from Pappaert, *et al.*¹⁵⁰ reports the measurement of diffusion coefficients in micron and sub-micron channels. They also consistently observe a decay of the effective diffusion coefficient in small channels. However, they were limited to a minimal channel height of 260 nm which is about 5 times larger than our experiment. From their data, similar coefficients as our measurements could be expected if they would have gone down to 50 nm.

They proposed a theoretical model for describing the apparent diffusion coefficient in a confined slit:

$$t_{col} = \frac{h^2}{12D_{app}} \quad (6.1)$$

where t_{col} is the mean time between two successive analyte-wall collisions, taking into account the retardation time $\tau_{surf}=1/k_{off}$:

$$t_{col} = \frac{h^2}{2D_{bulk}} + \frac{1}{k_{off}} \quad (6.2)$$

6.1 Apparent diffusion in nanoconfinements

By adapting equation 6.1, the apparent diffusion coefficient in the nanoslit configuration is:

$$D_{app} = \frac{h^2}{12t_{col}} = \frac{h^2}{12 \left(\frac{h^2}{2D_{bulk}} + \frac{1}{k_{off}} \right)} \quad (6.3)$$

And, as for WGA proteins $k_{off}=100 \text{ s}^{-1}$ is relatively high compared to D_{bulk}/h^2 value, equation 6.3 can be approximated by:

$$D_{app} \approx \frac{h^2}{12} k_{off} \quad (6.4)$$

giving the theoretical value $D_{app}=2 \cdot 10^{-14} \text{ m}^2/\text{s}$ for WGA proteins in 50 nm high nanochannels, which matches precisely the measured value of figure 1.15.

The problem with measuring the apparent diffusion coefficient of fluorescently-labeled species when they are filling a simple straight 1D nanochannel (as for the experiment of figure 1.15), is that the user has only one chance to measure the apparent diffusion: once the channels are filled with the solution containing the proteins, the surfaces may be contaminated by protein adsorption and the device has to be cleaned before injecting a novel plug of concentrated solution.

Several other methods for measuring diffusion of species in a liquid solvent have been elaborated during the last decades, such as a diaphragm cell¹⁵⁶, Taylor dispersion¹⁵⁷, stationary phases by frontal chromatography¹⁵⁸, spin echo nuclear magnetic resonance¹⁵⁹, transient grating light¹⁶⁰, and wedge interferometer¹⁶¹. The diffusions of proteins through membranes^{129;162;163} and nanochannels^{107;106} have also been widely reported, but take into account overall transport across a nanoconfinement (by reading the difference of protein concentration from the areas outside the nanochannel input and output). However, as highlighted in chapter 5 with FCS which is also a great method for measuring diffusion of biomolecules, the internal diffusion factor often has a considerable influence on transport in nanopores.

Another simple possibility is to measure the apparent diffusion coefficient based on the steady-state diffusion profile along the nanochannel with a global top-view concentration measurement. Figure 6.1 is illustrating such a system composed of 2 microchannels linked together by a 1D nanochannel. The solution containing fluorescently-labeled protein concentration c_0 is injected in microchannel 1 and enters in the nanochannel. A clean solution is flowing in the microchannel 2 in order to maintain $c=0$. As highlighted in figure 5.7, a steady-state diffusion profile is obtained. It is still possible to extract

6. APPARENT DIFFUSION MEASUREMENT USING STEADY-STATE DISPERSION

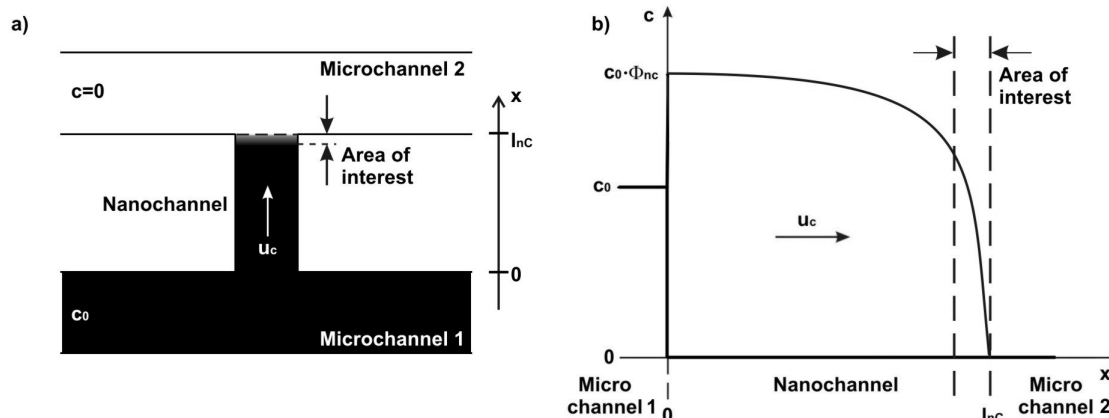


Figure 6.1: (a) Illustration of the solution containing the fluorescently-labeled proteins (in black) flowing from microchannel 1 into the nanochannel. A clean solution $c=0$ is rinsing microchannel 2. (b) Concentration profile inside the nanochannel. The area of interest is defined as the length inside which 80% of the concentration change is included.

the apparent diffusion from this profile, but this method lacks accuracy due to the difficulties of precisely tuning the flow in the nanochannel u_c . This is important in order to increase the area of interest, *i.e.* the area in the diffusion profile inside which 80% of the concentration change is included.

In order to facilitate the extraction of the apparent diffusion coefficient of biomolecules in nanoconfinements from the diffusion profile, a novel simple technique based on measuring the steady-state dispersion of fluorescent species in an adjacent nanoslit is developed in the following sections.

6.2 Steady-state dispersion effects

Our device, shown in figure 6.2, consists of a narrow nanochannel which is opening to a wide and short nanoslit area of the same nanometer dimension height. The nanoslit is adjacent to a much deeper microchannel. The experimental procedure is the following: fluorescently labeled molecules are injected in the nanochannel at a constant pressure difference. In the lateral nanoslit standing at the end of the nanochannel the 1D flow of fluorescent molecules is transformed into a 2D spreading flow. The lateral spreading distance of the molecules in the nanoslit is used to extract the value of the apparent diffusion coefficient.

6.2.1 Theory

As depicted in figure 6.2a, the fluid dynamics inside the nanoslit are quite difficult to express mathematically, due to complex flow line directions and varying flow velocity. Finite element method (FEM) simulations allow for the simulation of this problem in a complex geometrical environment and FEM results will be compared to measurements in further sections of this chapter. However, I will firstly provide a very simplified mathematical model in order to highlight why big molecules with a small diffusion coefficient seem to disperse longer inside the nanoslit compared to small molecules with a high diffusion coefficient.

In this model, I assume that solutions are dilute and incompressible, there are no chemical reactions except between proteins, that external forces and mass transport are only due to apparent diffusion (including molecules-surfaces interactions) and convection, and that local electrical phenomena due to streaming potential are negligible. I assume that biomolecules are drawn into the nanochannel from a large reservoir, keeping the concentration $c_{nC} = c_0 \Phi_{nC}$ in the nanochannel constant (with $\Phi_{nC}=7$ the equilibrium partitioning coefficient as defined in equation 4.12, with $c_0=2 \mu\text{M}$, $r_p=4 \text{ nm}$, $k_{on}=7.28 \cdot 10^5 \text{ M}^{-1}\text{s}^{-1}$ and $k_{off}=100 \text{ s}^{-1}$). As the nanochannel height is two hundred times lower than its width, a flat velocity profile is obtained for the injected florescent plug in the x-y plan. As demonstrated in the previous section, apparent diffusion coef-

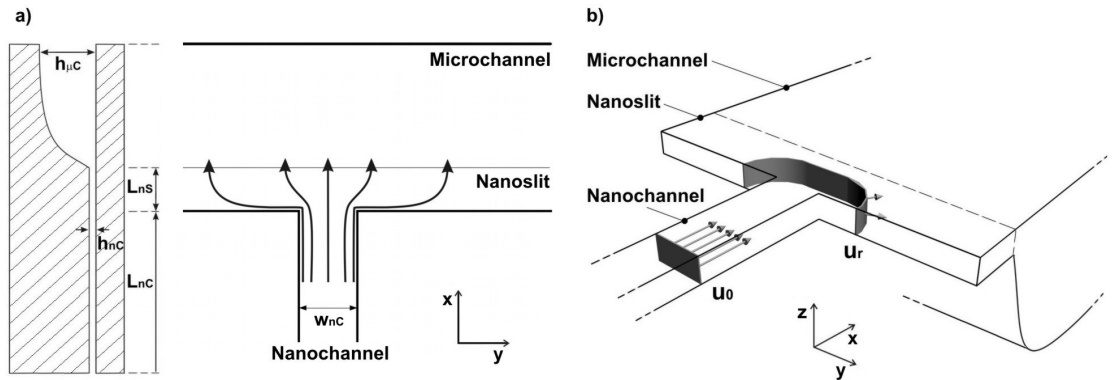


Figure 6.2: (a) Illustration of the flow direction in the nanochannel, in the nanoslit area and finally ending in the microchannel. The left scheme represents cross-sections of the nanoslit and the microchannel (not to scale). The flow lines expand laterally in the nanoslit area. (b) 3D schematic of the nanofluidic system (not to scale) showing the principle of the simplified model. Flow directions in the nanochannel and in the nanoslit are illustrated by 3D arrows. In the nanochannel, the flow velocity u_0 remains constant, whereas the flow front is expanding in the nanoslit, leading to a decrease of the average flow velocity $u_r(x, y)$.

6. APPARENT DIFFUSION MEASUREMENT USING STEADY-STATE DISPERSION

ficients of molecules in the nanochannel are much smaller than in bulk diffusion and consequently, mass transport is primarily convective rather than diffusive.

When the plug front enters the nanoslit located at the end of the nanochannel, it expands in a “flat half-circle” shape before flowing into the microchannel as illustrated in figure 6.2. This simplified description of the front profile of the biomolecules is valid for an infinitely thin nanochannel ($w_{nC} \rightarrow 0$) and infinitely long nanoslit ($l_{nS} \rightarrow \infty$), which are acceptable approximations in our case. By simplifying the validity of the equation of continuity¹⁶⁴, from the nanochannel-slit transition, a decrease of the average flow velocity u_r is observed along the semi-circular flow front at the $r = (x^2 + y^2)^{0.5}$ position as the biomolecule plug front moves away from the nanochannel:

$$u_r(r) \approx u_0 \frac{w}{\pi r + w} \quad (6.5)$$

where u_0 is the initial flow velocity in the nanochannel and w_{nC} the nanochannel width. Integrating equation 6.5 with respect to r gives:

$$t(r) = \frac{\pi r^2}{2u_0 w} + \frac{r}{u_0} \quad (6.6)$$

Next, I assume that the liquid passing through the nanochannel-nanoslit transition from the nanochannel has a fixed concentration c_{nC} . The output microchannel serves as a sink, where the concentration of proteins is maintained closed to zero by slow microchannel flow of pure buffer solution. The concentration profile of the proteins along the nanochannel and the nanoslit is derived for the three principle cases: (i) diffusion is the only transport mechanism for proteins, *i.e.* no flow velocity through the nanochannel is applied, a steady-state diffusion profile is obtained, which is independent of the diffusion coefficient; (ii) the diffusion coefficient is null or the velocity in the nanochannel u_0 is infinite, then a constant concentration c_{nC} along the nanochannel and the nanoslit is obtained; (iii) the intermediate case for finite diffusion coefficient. The theory developed in section 5.4.2 can be used here. However, another interesting model of unsteady diffusion in a semi infinite slab was developed by Cussler¹⁵² and will be used here. Finally, the concentration profile $c(r)$ in the nanoslit in this last case is:

$$c(r) = c_{nC} \cdot erf \left(\frac{r_{nS} - r}{\sqrt{4Dt}} \right) \quad (6.7)$$

where $r_{nS} = l_{nS}/\sin\theta$ is the distance inside the nanoslit between the channel-slit transition and the microchannel. θ is the angle between the chosen radial velocity u_r and the lateral velocity u_y . erf the error function is defined by:

$$erf\zeta = \frac{2}{\sqrt{\pi}} \int_0^\zeta e^{-s^2} ds \quad (6.8)$$

The nanochannel and nanoslit lengths l_{nC} and l_{nS} should be designed large enough so that the biomolecule concentration is close to c_{nC} when entering the nanoslit. Assuming an infinite source of biomolecules at concentration c_{nC} , the diffusion profile achieves a steady-state and equations 6.6 and 6.7 can be combined:

$$c(r) = c_{nC} \cdot erf \left(\frac{r_{nS} - r}{\sqrt{\frac{D}{u_0} \cdot \left(\frac{2\pi(r_{nS}-r)^2}{w} + 4(r_{nS} - r) \right)}} \right) \quad (6.9)$$

Figure 6.3 illustrates the concentration profile as a function of the distance in the nanoslit from the nanochannel-slit transition as described by equation 6.9, for different values of the diffusion coefficient ($D_1 > D_2 > D_3$). For a given nanochannel velocity u_0 , large molecules with low diffusion coefficients take longer to pass through the nanochannel than small ones with higher diffusion coefficients, resulting in a larger dispersion distance in the lateral nanoslit. This effect is used to locally measure the diffusion coefficients, thus resulting in the formation of protein complexes.

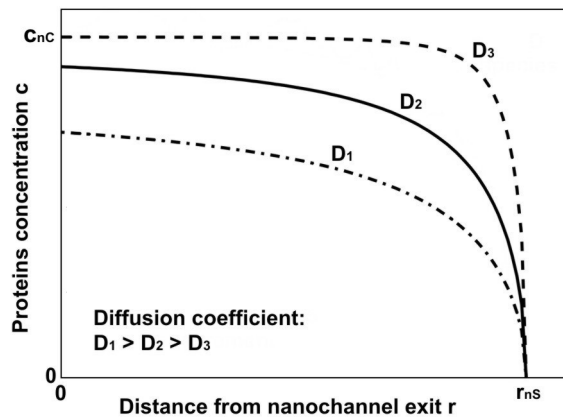


Figure 6.3: Steady diffusion of proteins through a 2D nanoslit from the nanochannel exit ($r=0$) into the exit microchannel ($r=r_{nS}$) when a constant fluid velocity u_0 is applied. The curves are plotted using equation 6.9 and show that higher diffusion coefficients decrease the concentration profile.

6. APPARENT DIFFUSION MEASUREMENT USING STEADY-STATE DISPERSION

6.2.2 Finite element analysis

In order to extract the diffusion coefficient from the experiments, Finite element analysis was performed with COMSOL Multiphysics using Incompressible Navier-Stokes physics from the MEMS Module coupled with Convection and Diffusion physics from the Chemical Engineering Module. A 2D geometry with a thickness of 50nm was used, creating a shallow channel approximation. All subdomains were assigned a density of $\rho=1000 \text{ kg/m}^3$ and a dynamic viscosity of $\eta=0.001 \text{ Pa}\cdot\text{s}$. The diffusion coefficient in the microchannel was set to $10^{-10} \text{ m}^2/\text{s}$ and consequently the microchannel acted as a well. An inflow boundary condition with y-velocity is applied to the input of the nanochannel. No-slip boundary conditions were applied to the walls of the nanoslit and nanochannel, and outflow boundary conditions were applied to the sides of the nanoslit as well as to the walls of the microchannel. The input and output boundaries of the nanochannel had a constant concentration of $14\mu\text{M}$, whereas the concentration in the microchannel was assigned to 0. Insulation conditions were applied to the walls of the nanoslit, as well as to the sides of the nanochannel. Adapted meshings were used for the nanoslit, nanochannel and microchannel. The maximum element size for the nanoslit and the nanochannel was $5\cdot 10^{-7}$ and 10^{-5} for the microchannel, giving a total of 6373 elements. The UMFPACK linear system was used to solve the problem as a function of diffusion coefficients and input velocities. The spatial repartition of concentrations is presented in steady-state conditions in figure 6.4a. It should be noted that a lateral flow in the microchannel does not influence the flow conditions (*i.e.* the chemical dispersion) within the nanoslit because of a large difference in hydraulic resistance.

The numerical simulations show that the lateral dispersion in the nanoslit area depends mainly on two parameters (for a given channel height): (1) the apparent diffusivity of the molecules (comprising the molecules-surfaces interactions) and (2) the flow speed in the nanochannel. The distance of dispersion r can be plotted as a function of the diffusion coefficients for different input velocities, as presented in figure 6.4b. It can be observed that the lateral dispersion is decreasing at increasing diffusion coefficients. This behavior is rather counter intuitive at first glance because higher lateral diffusion should be expected for more diffusive molecules. However, this effect can be easily explained by the fact that highly diffusive molecules will quickly fall in the adjacent microchannel (which acts as a sink) whereas low diffusive molecules will follow the flow lines for longer, which are spreading laterally along the nanoslit. Consequently, the lateral dispersion increases when flow speed in the nanochannel (*i.e.* pressure) is

6.3 Single-component dispersion experiments

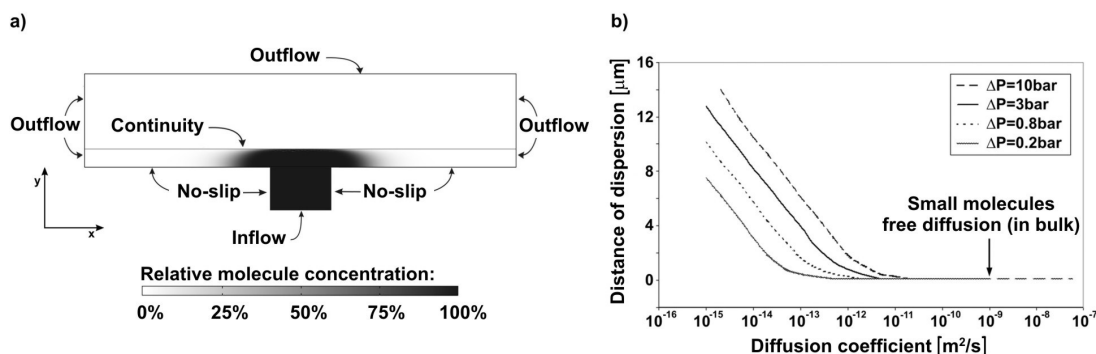


Figure 6.4: Finite element simulation (a) of the protein concentration repartition in the nanoslit area after exiting the nanochannel. The boundary conditions are indicated on the figure. A lateral dispersion, related to the diffusion coefficient of the molecules, is observed in the nanoslit area. Conditions: $u=130$ nm/s, $D_{app}=8 \cdot 10^{-15}$ m²/s, $w_{nC}=10$ μm, $l_{nC}=7$ μm, $l_{nS}=3$ μm, $h=50$ nm, $\rho=1000$ kg/m³, $\eta=10^{-3}$ Pa·s. (b) Distance of dispersion r as a function of the diffusion coefficient for different values of the input pressures (*i.e.* flow velocities). Increased diffusion coefficient decreases the lateral dispersion.

augmented. Highly diffusive molecules are no longer laterally dispersed in this device and thus cannot be measured. When molecules having low apparent diffusion coefficients are used, the distance of dispersion is a function of the flow velocity in the nanochannel, and can be easily detected over a large range of flow velocities. Conversely, when molecules have high apparent diffusion coefficients, changes in the lateral distance of dispersion can only be detected at high nanochannel flow speeds. The numerical simulations of molecule concentration can then be used to fit experimental data obtained with fluorescently labeled species and then extract the apparent diffusion coefficient of the molecule of interest.

6.3 Single-component dispersion experiments

Materials and methods

Figure 3.4a shows a SEM picture of a manufactured device. 10 mM Potassium chloride (KCl) solutions were prepared at different values of the pH fixed by adding small amounts of diluted HCl or KOH, in deionized water (18 MΩ·cm). An air-pressure regulator (from Bellofram) from -0.8 to 3 bar was used to drive every port in the nanofluidic device. The motion of fluorescently-labeled proteins through the nanochannel was recorded by a single-photon counting camera connected to a Zeiss Axiovert confocal microscope. The effects of any disparities in the optical system (lens aberration, filter quality and lamp intensity fluctuations) were ignored. In this experiment, the same

6. APPARENT DIFFUSION MEASUREMENT USING STEADY-STATE DISPERSION

fluorescent WGA proteins as in the previous chapter (with Alexa Fluor® 633 from Molecular Probes, 38,000 Da of molecular weight and $k_{off}=100 \text{ s}^{-1}$), and fluorescein molecules (FITC from Sigma-Aldrich, 380 Da of molecular weight and $k_{off}>10^5 \text{ s}^{-1}$) were used. The free diffusion coefficient of WGA proteins in water has been reported by Munson, *et al.*⁸⁴ to be $D_{WGA,bulk}=7.6 (\pm 0.3) \cdot 10^{-11} \text{ m}^2/\text{s}$, and FITC in same conditions to be $D_{FITC,bulk}=4.2 (\pm 0.1) \cdot 10^{-10} \text{ m}^2/\text{s}$ as reported by Pappaert, *et al.*¹⁵⁰.

Results and discussion

A first experiment was performed in order to compare the apparent diffusion of big molecules (WGA proteins) interacting slightly with surfaces, and small molecules (fluorescein dyes) that do not interact with surfaces. Results are shown in figure 6.5a and figure 6.5c respectively for the same flow conditions. The measurements clearly confirm the expected behavior from the model and the FEM simulation which predicts lateral dispersion for low diffusive molecules (WGA) and practically no dispersion for highly diffusive molecules (fluorescein). When a lateral flow is set in the microchannel, the dispersion in the nanoslit is not changed as shown in figure 6.5b and figure 6.5d.

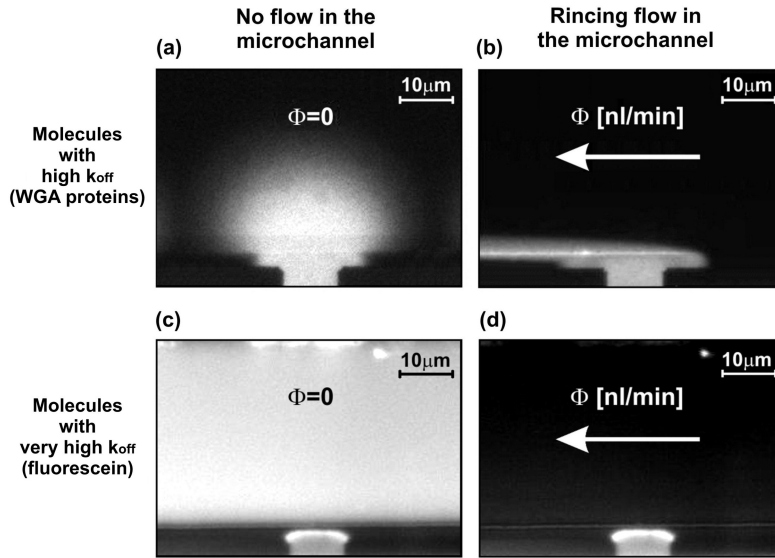


Figure 6.5: Video images showing the diffusion of fluorescent species through the nanochannel, the nanoslit and the microchannel. WGA proteins were pushed in the nanochannel and no flow was applied at the output microchannel in the case (a), and a flow of several nl/min in case (b). Proteins (WGA, $D_{app} \approx 10^{-14} \text{ m}^2/\text{s}$, $k_{off}=100 \text{ s}^{-1}$) are replaced with fluorescein (FITC, $D_{app} \approx 10^{-11} \text{ m}^2/\text{s}$, $k_{off}>10^5 \text{ s}^{-1}$) in case (c) and (d) under same conditions as (a) and (b).

6.4 Detecting proteins complex formation

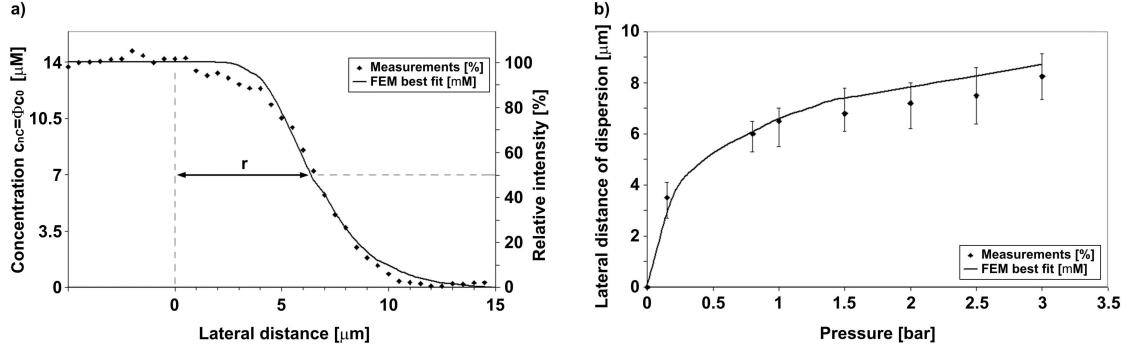


Figure 6.6: (a) Plotline representing the experimental normalized intensity of fluorescently-labeled WGA, measured by the camera at $y=1 \mu\text{m}$ compared with the simulated value (fitted with $D_{WGA,app}=8 \cdot 10^{-15} \text{ m}^2/\text{s}$). Conditions: Diffusion of $c_0=2 \mu\text{M}$ WGA into 10mM KCl and deionized water, $\text{pH}=7.7$, $u_{init}=130 \text{ nm/s}$, $T=300 \text{ K}$. (b) Variation of measured lateral dispersion versus the pressure applied to the system. The continuous curve represents a COMSOL Multiphysics simulation and the dots are the measurements acquired with the camera in the same conditions. 1 bar of applied pressure corresponds approximately to a 3 fl/min flow.

Figure 6.6a shows the dispersion profile of $c_0=2 \mu\text{M}$ fluorescently-labeled protein WGA in a solution of 10 mM KCl in DI water ($\text{pH}=7$). The plotline is located at $1 \mu\text{m}$ from the nanochannel in the y -direction ($\theta=0$) and the applied fluid velocity in the nanochannel is $u_0=130 \text{ nm/s}$. A shutter was used in order to avoid photobleaching of the dyes. Based on the fitting of experimental data, an apparent diffusion coefficient of $D_{WGA,app}=8.0 (\pm 2) \cdot 10^{-15} \text{ m}^2/\text{s}$ was obtained in the nanoslit area, which is in the same order of magnitude as the theoretical value of $2 \cdot 10^{-14} \text{ m}^2/\text{s}$ obtained with equation 6.4.

Alternatively, the lateral dispersion effect can also be used as a measure of the extremely low flow rate in the nanochannel in steady-state conditions. The mass flow of solution in the nanochannel is given by the ratio between the pressure variation and the hydrodynamic resistance of a channel. Figure 6.6b is the measured lateral distance r of dispersion of $c_0=2 \mu\text{M}$ WGA proteins in our previously described nanochannel for different pressures (*i.e.* flow rates). Flow rates down to 1 fl/min can be measured with this device.

6.4 Detecting proteins complex formation

Williams *et al.*¹⁶⁵ have demonstrated the possibility to detect solute concentration by measuring diffusion change in a microfluidic T-sensor and Hatch *et al.*¹⁶⁶ have reused this principle to detect immunobinding. In this section, I exploit the apparent diffusion

6. APPARENT DIFFUSION MEASUREMENT USING STEADY-STATE DISPERSION

effect and present a protein binding affinity bioassay based on steady-state diffusion in a nanochannel.

As reported in equation 6.3, when biomolecules enter a nanoslit from an adjacent nanochannel, they disperse laterally in function of their affinity mainly with surfaces, and in some conditions as a function of their size. The lateral dispersion is affected by apparent diffusion of molecules: decreasing apparent diffusion extends lateral dispersion because molecules stay longer along their flow line before diffusing into the main microchannel. This phenomenon is used here to measure protein complex formation, which changes the molecular adsorption kinetics.

Materials and methods

In this experiment I used fluorescent streptavidin proteins (with Alexa Fluor® 633 from Molecular Probes, 53 kDa of molecular weight) and biotin-dextran (from Sigma-Aldrich, 10 kDa of molecular weight) because of their strong affinity ($K > 10^{14} \text{ M}^{-1}$)¹⁶⁷. WGA was used as a non-specific control protein. PBS solution of pH 7.1 diluted with deionized water was used as a solution buffer.

Results and discussion

Streptavidin is a protein comparable to WGA protein: they are both similar in size at around 8 nm, have a similar bulk diffusion coefficient around $10^{-10} \text{ m}^2/\text{s}$, and similar adsorption kinetic parameters with glass surfaces¹⁶⁸. As predicted in equation 6.4, the apparent diffusion coefficient was then assumed to be exclusively proportional to the desorption constant k_{off} . Each streptavidin molecule has 4 potential sites of affinity with biotin. So when adding the biotinylated dextran proteins, it forms a streptavidin-biotin-dextran complex which doubles its size and may change its affinity to surfaces, and thus its apparent diffusion coefficient.

Figure 6.7 shows fluorescent biomolecules diffusing in the nanoslit area as observed through a standard fluorescence microscope. First streptavidin proteins were injected and driven by air pressure until the steady-state diffusion profile observed in figure 6.7a was obtained. Then biotinylated dextran was injected in order to investigate if a change in the apparent diffusion coefficient occurs. Figure 6.7b shows the steady-state dispersion profile of the streptavidin-biotin-dextran complex after adding biotinylated dextran: an increase of fluorescence steady-state diffusion is clearly observed. The same experiment was reproduced with WGA proteins as non-specific control, instead

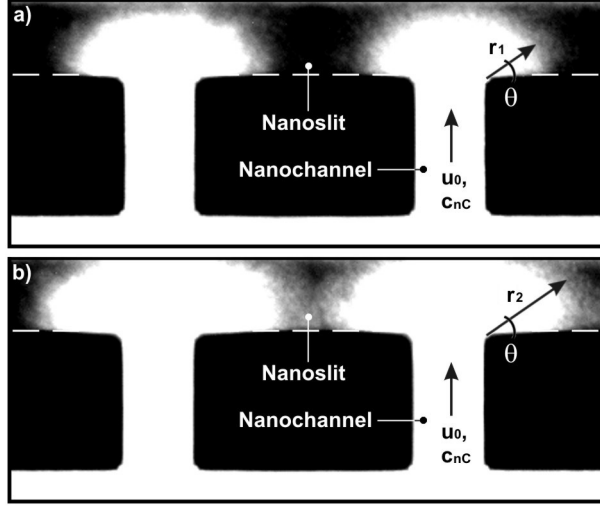


Figure 6.7: Video images showing the steady-state dispersion of fluorescent species through the nanoslits ($w_{nC}=10 \mu\text{m}$, $l_{nS}=10 \mu\text{m}$, $l_{nC}=20 \mu\text{m}$). (a) $2 \mu\text{M}$ fluorescent streptavidin proteins were injected in the nanochannels by applying a pressure difference $\Delta P=0.3 \text{ bar}$ (corresponding to $u_0=120 \text{ nm/s}$) and measured the distance r_1 from the exit of the nanochannel to half fluorescence intensity $c_{nC}/2$ for $\theta=45^\circ$ angle. (b) $6 \mu\text{M}$ non-fluorescent biotinylated dextran was added and the increased length r_2 was measured (at the same ΔP and θ). The experiments are realized in PBS solution with pH of 7.1.

of biotin-dextran. As expected, there was no significant change in the apparent diffusion profile.

Plotted in figure 6.8 is the recorded fluorescence intensity in the nanoslit along r before and after adding the biotin-dextran solution. From the best fits using equation 6.9, the apparent diffusion coefficients $D_1=1.6 \cdot 10^{-13} \text{ m}^2/\text{s}$ and $D_2=8 \cdot 10^{-14} \text{ m}^2/\text{s}$ were calculated for streptavidin and the streptavidin-biotin-dextran complex respectively, The experiment was repeated several times with different flow velocities in the nanochannel. From these apparent diffusion coefficients, I extracted k_{off} values of 770 s^{-1} for streptavidin, respectively 380 s^{-1} for the complex. This decrease of dissociation constant value means that the complex molecule remains adsorbed on the surface ($\tau_{surf}=2.6 \text{ ms}$) twice the time of the streptavidin alone ($\tau_{surf}=1.3 \text{ ms}$).

Figure 6.9 shows the strong difference of the apparent diffusion profile between fluorescent primary proteins alone and fluorescent primary proteins bounded with a corresponding protein complex, is visible over a large range of actuation pressures (from 0.1 to 0.6 bar).

The principle of detecting complexing species in nanoconfinements by differential apparent diffusion rates as described in this section can be applied to a wide range of

6. APPARENT DIFFUSION MEASUREMENT USING STEADY-STATE DISPERSION

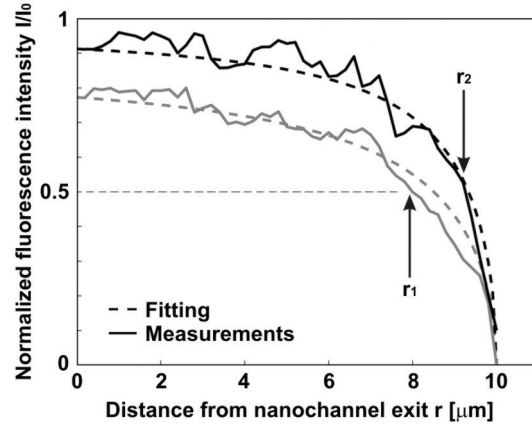


Figure 6.8: Evolution of the concentration profile of proteins with the distance from nanochannel exit. The measurements were performed on video images with $\theta=90^\circ$, in the same conditions as figure 6.7. Gray lines represent fluorescent streptavidin proteins (higher D_{app}) diffusion profile and black lines fluorescent streptavidin with biotin-dextran complex (lower D_{app}). Lines represent measurements and dotted lines are best fits using equation 6.9 with $u_0=120$ nm/s, $l_{nS}=10$ μm , $l_{nC}=20$ μm , $D_1=1.6\cdot 10^{-13}$ m^2/s and $D_2=8\cdot 10^{-14}$ m^2/s .

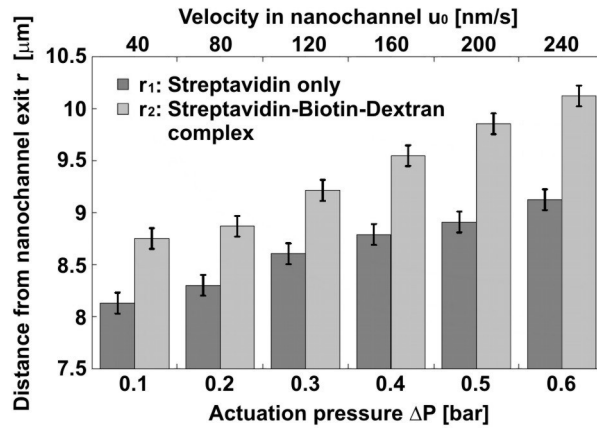


Figure 6.9: Measured distances from nanochannel exit to half fluorescence intensity before (in dark gray) and after (in light gray) adding biotinylated dextran to fluorescent streptavidin diffusing in a nanoslit for different actuation pressure. The error bars indicate the error of reading when injecting the proteins. Conditions: $\theta=45^\circ$, $w_{nC}=10$ μm , $l_{nS}=10$ μm , $l_{nC}=20$ μm and $c_0=2$ μM .

biomolecules: (i) proteins with high k_{off} (not sticky) are particularly well suited as in the case of WGA proteins, streptavidin or biotinylated dextran. However, for very small molecules with very high k_{off} like fluorescein, the flow velocity in the nanochannel u_c should be strongly increased in order to make the dispersion appear. (ii) Biomolecules with low k_{off} (very sticky) participate in the decrease of the apparent diffusion coefficient value and then the flow velocity in the nanochannel has to be decreased in order to limit the dispersion effect in the detection spot, depending on the microscope objective.

6.5 Outlook and conclusions

The possibility to measure the apparent diffusion coefficients of fluorescently labeled species inside nanofluidic channels by using the dispersion effect in a nanoslit was demonstrated. Concentration profiles over flow velocity, diffusion coefficients, and positions were calculated by using a simple flat front model, leading to the prediction of changes of adsorption time of biomolecules on the nanochannel surfaces. I showed that molecules with a high apparent diffusion coefficient (molecules with very high k_{off}) diffuse quickly from the nanochannel into the microchannel through the nanoslit, whereas molecules with smaller apparent diffusion coefficients (molecules with lower k_{off}) follow the fluid flow lines for longer, which results in a larger lateral dispersion in the nanoslit. I performed measurements with WGA proteins and obtained, under specific conditions, an apparent diffusion coefficient which is 4 orders of magnitude lower than the free diffusion coefficient. This novel technique which is a direct and relatively simple measurement of the apparent diffusion coefficients inside nanochannels of well controlled dimensions could also be used as a complexing affinity biosensor. Fluorescent streptavidin proteins were injected in the system and the concentration profile was measured for different nanochannel flow velocities. Specific biotinylated dextran proteins were added and an important increase of the dispersion length was measured, which was not observed when injecting non-specific wheat germ agglutinin proteins. This nanofluidic device provides an interesting solution for simple and rapid measurement of adsorption kinetic changes.

6. APPARENT DIFFUSION MEASUREMENT USING STEADY-STATE DISPERSION

CHAPTER

7

CONCLUSION AND OUTLOOK

This last chapter summarizes the main achievements presented in the scope of this thesis. I will come back to the different experiments, such as the protein-surface interaction kinetic measurements by electrical detection, by fluorescence correlation spectroscopy, and by steady-state dispersion technique. Finally, I will provide insight into the passive transport of biomolecules in nanoconfined areas and how this offers future opportunities in biomedical and biological applications.

7. CONCLUSION AND OUTLOOK

7.1 Summary of achievements and recommendations

The main objective of this thesis was to gain a deeper understanding of phenomena influencing the transport of biomolecules diffusing through nanoconfinements, and indeed, new theoretical models describing the diffusive transport of biomolecules were elaborated and verified experimentally in different environmental conditions. Electrical and optical measurements were performed in order to measure interactions between the proteins and the nanochannel surfaces, as well as diffusivity of proteins in different ionic and pH conditions. This research has highlighted novel phenomena that were successfully predicted, observed and quantified, but has also opened many novel questions. The main findings are quickly summarized in this section.

7.1.1 Electrical detection of protein-surface interaction

One of the first achievements of this thesis was the conception of a nanofluidic platform designed for electrically measuring protein adsorption kinetics. Based on fully integrated on-chip electrodes, this label-free detection method is a very interesting candidate for future low-cost industrial analysis devices. The reading of the electrical impedance, at optimal frequency, has allowed for the verification of two fundamental regimes acting on the electrical conductance:

- In high ionic strength solutions, electrical conductance is mainly defined by the intrinsic conductance of the solution and limited by the nanoconfinement geometry. Proteins are then obstructing the nanochannels section, and thus participating to reduce the electrical conductance value;
- In low ionic strength solutions, electrical conductance is mainly defined by the surface charges of the nanoconfinement. Proteins are still obstructing the nanochannel section but are also bringing counter-ions inside the nanochannels, which strongly participate to increase the electrical conductance value.

A simple model for calculating the effect of protein adsorption-desorption on electrical conductance was elaborated. Based on the measurements of different protein charges in the different ionic regimes, several important parameters were extracted, such as:

- the adsorption and desorption constants;
- the direct measurement of the kinetics of adsorption and extraction of the time constant;

7.1 Summary of achievements and recommendations

- the effective surface coverage;
- the effective protein concentration;
- the effective surface charge equilibrium.

This technique has shown to have several advantages compared to existing methods, such as the simplicity of measurement, potential to integrate the detection unit, low cost of production, suitability for fast multiplexing label-free detection of biomolecules on-chip and can become a powerful biophysical alternative for surface plasmon resonance devices in determining kinetic and equilibrium constants of molecular interactions. However, only one type of protein has been tested in the scope of this experiment, it will be of great value to test several different biomolecules in order to confirm that the theory is valid in all cases.

Another very interesting potential investigation, which is strongly related to the theory of this chapter, is about pH shift phenomenon in the nanoconfinements. As demonstrated by Veenhuis *et al.*¹⁶⁹, a pH shift up to 1.6 pH units may be present in nanochannels due to the release or uptake of protons from the surface. Future experiments for characterizing this pH shift would be very useful, especially in low ionic strength solutions, in order to improve accuracy of the theoretical models. It will also help to predict effective surface and biomolecule charges inside the electrical double layer.

When measuring low ionic strength solutions, I frequently observed a signal derive that was a function of the pressure-driven flow in the microchannels. For future experiments, I would recommend to perform differential measurements using a third channel. As depicted in figure 7.1, the first nanochannel conductance measurement will provide information of the biomolecular diffusion when the second one will only bring information about the change of surface charge with time and flow speed. In this configuration, the differential measurement is no longer sensitive to the pressure-driven liquid flow.

Coupling a FCS detection system with electrical measurements will also be of great interest to measure simultaneously global and local binding kinetics between biomolecules and surfaces. With such a method, it would be possible to directly measure and extract from a solution with unknown ionic and pH conditions all parameters to predict the effective diffusive transport of the biomolecules of interest.

7. CONCLUSION AND OUTLOOK

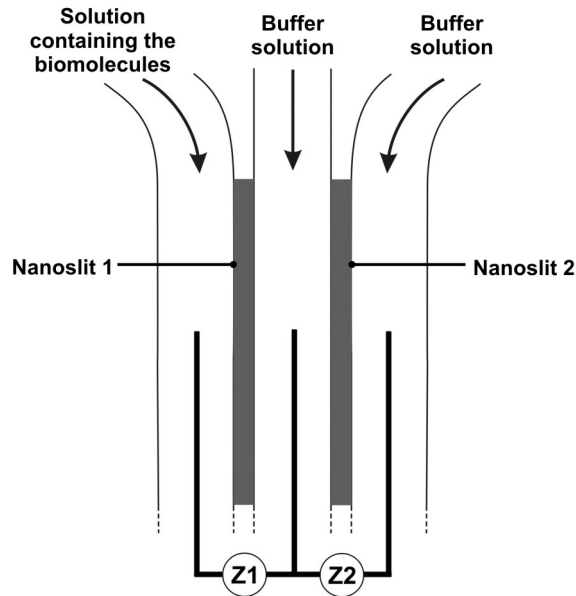


Figure 7.1: Principle of the differential measurement configuration designed to avoid signal derive due to pressure-driven flow (especially in low ionic strength conditions). The illustration represents 3 microchannels, linked together by 2 nanoslits. The solution containing the biomolecules is injected in the first microchannel. $Z1$ measures the conductance change due to the biomolecules presence in the nanoslit 1, when $Z2$ is measuring the derive of nanoslit 2 conductance due to liquid flow in microchannels.

7.1.2 Transition between surface-dominated and bulk diffusion regimes

The second main achievement of this work is the coupling of a FCS microscope with a nanofluidic setup. Based on this powerful tool, hindered diffusion of single charged proteins through nanochannels was measured and characterized in different ionic and pH conditions.

From the nanofluidic point of view, these experiments have highlighted:

- new theoretical models for hindered diffusion, taking into account the steric exclusion, the adsorption and desorption of biomolecules on surfaces, and the exclusion-enrichment effects;
- the presence of different populations of biomolecules (*i.e.* those which diffuse without wall interactions, and those which adsorb and desorb once or more);
- evidence of different diffusion regimes occurring from interactions between charged proteins and the electrical double layer;

7.1 Summary of achievements and recommendations

- ionic conditions where charged proteins never interact with surfaces and thus where their effective diffusion coefficient tends to be the same value as the bulk diffusion coefficient;
- the biomolecular diffusion profile directly inside the nanochannels, with and without convective flow across the channel.

And from the optic point of view:

- novel autocorrelation functions describing biomolecules diffusing inside highly confined slits, taking into account the different populations of interacting proteins;
- the possibility to estimate the number of molecules present in the nanoslits for different ionic regimes;

This technique to predict concentration and interactions of single proteins diffusing in nanometer slits can be easily used to get a better understanding of on-chip, membranes separation or proteomic processes. It also supplies new elements of theoretical models to better understand fundamental nanofluidic physics in order to develop further biomedical and biological diagnostics devices. However, further experiments have still to be performed. For example, testing WGA proteins at $\text{pH} < \text{pI}$ and $\text{pH} = \text{pI}$ would verify the theory for diffusing positively-charged and non-charged biomolecules in nanoconfinements. Experiments with different types of biomolecules would also be of great interest for controlling the validity of the diffusion theories elaborated in this thesis. Changing the nanochannel's height would also be interesting, especially for testing the steric effect and the limits of continuum models ($h < 10$ nm).

From the measurements performed in chapter 5, the FCS autocorrelation curves can be reanalyzed at shorter diffusion times, in order to investigate a potential change of triplet-state function when the biomolecules are interacting with surfaces or not. It can bring a deeper understanding on triplet-state physics.

An interesting alternative to FCS is the Total Internal Reflection FCS (TIR-FCS), which is a technique especially efficient for measuring biomolecules with surface interactions. As depicted in figure 7.2, a laser beam with vacuum wavelength λ_0 travelling from a high refractive index medium into a lower refractive index medium is totally internally reflected at the interface when its incidence angle is greater than the critical angle, creating an evanescent field that penetrates into the lower refractive index medium. The measured fluorescence fluctuates with time as biomolecules diffuse into the volume, bind to surface, desorb, and diffuse out of the volume. These fluorescence

7. CONCLUSION AND OUTLOOK

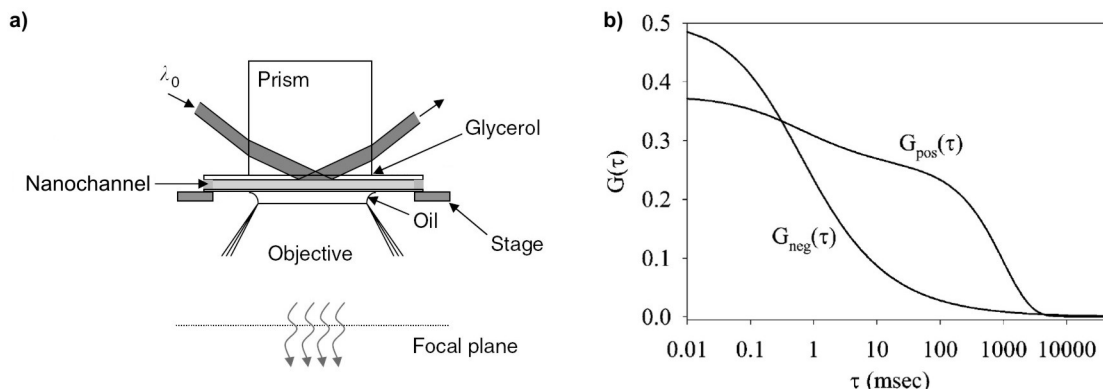


Figure 7.2: (a) Illustration of the TIR-FCS principle: the nanochannel is mounted onto an inverted microscope such that the prism is optically coupled with glycerol to the nanochannel substrate. Internal reflection is generated by focusing a laser beam through the prism onto the sample and the evanescently excited fluorescence is collected through the objective. Adapted from Thompson *et al.*¹⁷⁰. (b) Theoretically predicted TIR-FCS autocorrelation functions shown for samples with adsorbing molecules and without any adsorbing molecules. Adapted from Lieto *et al.*¹⁷¹

fluctuations are autocorrelated and fit to theoretical expressions to obtain information about the dynamics at or near the surface. Using this method in nanochannels would likely improve the differentiation of the different populations of biomolecules interacting with the surfaces (*i.e.* the number adsorbed when crossing the measurement volume).

Finally, a very promising emerging detection technology is to use functionalized nanoparticles¹⁷². Unlike fluorophores, nanoparticles are chemically very stable (the emitting signal does not change in function of pH, for example), they don't photobleach and they don't denature. I am persuaded that nanoparticles smaller than biomolecules of interest would definitely make them better candidates than fluorophore for single molecules detection.

7.1.3 Measurement of apparent diffusion coefficient

The FCS experiments have shown evidences of a strongly reduced value of the diffusion coefficients in nanochannels due to the interactions of single proteins with the surfaces. In chapter 6, a novel concept of a simple nanofluidic device able to measure the apparent diffusion of fluorescent biomolecules was introduced. A theoretical model describing the concentration profile of proteins dispersing in a nanoslit was also presented. Observations showed that the lateral dispersion was increasing at decreasing diffusion coefficients, which can appear counterintuitive but can be easily explained by the fact that highly diffusive molecules diffuse faster and thus quickly join the adjacent

microchannel. However, low diffusive molecules follow for a longer period the flow lines which are spreading laterally in the nanoslit. Based on the measurements of this lateral steady-state dispersion, apparent diffusion coefficient values were obtained that were four orders of magnitude lower than their values in the bulk.

This very simple technique can be easily integrated in future micro- and nanofluidic systems for measuring apparent diffusion coefficients of fluorescently-labeled proteins and thus may help fundamental studies in membranes and separation sciences, for example.

As for the previous sections, different types of proteins, with different values of dissociation constants k_{off} , should be tested in different conditions in order to confirm the theory elaborated in chapter 6.

7.1.4 Detection of protein complex formation

The last main achievement of this thesis consists in direct measurements of protein complex formation using the steady-state dispersion effect. In order to validate the model experimentally, the increase of fluorescent dispersion profile when adding specific biotinylated dextran to fluorescent streptavidin was measured in different conditions, showing that when complexing streptavidin with biotin-dextran, the complex adsorb longer to surfaces than streptavidin protein alone.

This novel technique is very interesting because of its simplicity to quickly measure affinity between proteins and between molecules and surfaces. However, it would be interesting to test different types of molecules in order to observe the opposite effect (*i.e.* reduction of the adsorption time). Moreover, in order to verify the theory, the same experiment with two specific molecules having very high k_{off} could be performed. In this case, it is expected one would observe a change of lateral dispersion in function of their size and of the complex size, rather than in function of binding kinetics.

7.2 Future perspectives

What about the future? While some scientists are still trying to identify novel phenomena appearing in nanofluidic systems, others are trying to understand nanofluidics directly from nature. On the one hand, even if the current microfabrication technology is very new compared to the nature complexity, it is already possible to fabricate synthetic ion channels and to simulate the cell biology in well defined conditions¹⁷³.

7. CONCLUSION AND OUTLOOK

On the other hand, it is also possible to use directly existing biological cell ion channels¹⁷⁴. Research on nanofluidics is definitively at the crossing of these two scientific approaches.

Starting from the achievements presented in this thesis, a series of concepts can be envisioned in order to go forward with nanofluidics. In this section, I will briefly propose some ideas related to the fabrication, manipulation, design, and finally will point out some applications that can be considered from this work.

7.2.1 Technical improvements

In a perspective of reducing the size of the optical measurement unit, efforts to integrate the optical system can be envisaged. In far-term, fabricating light sources, detectors and/or optics directly on-chip may be the best way to achieve high-sensitivity in an inexpensive and truly portable fluorescence-based micro- and nanosystem¹⁷⁵. For example, Yang *et al.*¹⁷⁶ have recently demonstrated that using near-field optical forces to confine matter inside waveguides, they were able to detect, trap and transport 75-nm dielectric nanoparticles and λ -DNA molecules. Based on a similar system, an interesting alternative to standard FCS unit can be envisaged by coupling optical waveguides with nanofluidics in order to confine light directly in the nanochannels and to avoid optical problems such as reflection and transmission losses.

In terms of future micro- and nanofluidic system developments, the current trend is to maximize the number of functions as well as the channel density. As illustrated in figure 1.3, Hong and Quake³ have realized such a dense microfluidic high-throughput cell assays device. It contains more than 2,000 integrated valves used for manipulating 256 compartments containing different bacterial cells. Their technical achievement is really impressive, but one important weak point is that liquid solutions have to be deposited into different very small cavities, and thus are quite difficult to manipulate for a human. I am persuaded that for future short-term diagnostic system developments, it will be worthwhile to realize simpler designs without any top cavities to fill and multiple functions to control, but rather multiple single very small devices containing integrated small apertures which will be automatically filled by capillarity when a solution is deposited onto the devices.

7.2.2 Biomedical and biological applications

Using the technology presented in this thesis, powerful nanofluidic devices for biomedical and biological applications can be designed. In this section, I will briefly describe applications that will be of great interest for biologists and physicians.

Immunology on-chip

Currently, the enzyme linked immunosorbent assay (ELISA) test is widely used to evaluate either the presence of an antibody or antigen in a sample. For example, it is used to test HIV or pregnancy, and in such cases, the labelling of the antibodies is performed by a fluorescent probe. After the reaction, the antibody-antigen complexes have to be separated from the free antibodies. The main limitation with this technique is the incubation time, due to the large diffusion distances that molecules have to travel.

The miniaturization of immunoassay is particularly relevant to diagnostic applications because the reduction of sample volume is of great importance when only minimal amounts of samples are available. In addition, immunoassay miniaturization allows the development of rapid and multiplexed assays that are more sensitive than macroscopic ones. As highlighted in the outlook of chapter 4, immunology can be performed in nanochannels. Different kinds of antigens can be attached to surfaces and the solution containing the antibodies can be injected through the nanochannels. Thus, the reaction can be measured electrically, optically, or even both to decrease the risk of wrong or unspecific detection. Such immunological tests can be parallelized and even multiplexed, but it is needed to modify the fluidic and electrical design, and to adapt the microfabrication process. Another important aspect to consider in this case is the complex surface chemistry, in order to deposit locally well-oriented target biomolecules and immobilize them properly.

Solving DNA puzzles

In 1978, Nathans, Arber and Smith received the Nobel Prize in Medicine for the discovery of restriction enzymes and their application to problems of molecular genetics. They showed that bacteria are developing restriction enzymes (or restriction endonuclease), which is an enzyme that cuts double-stranded or single stranded DNA at specific recognition nucleotide sequences in order to provide a defence mechanism against invading viruses¹⁷⁷. Inside a bacterial host, the restriction enzymes selectively cut up foreign DNA in a process called restriction, while the host DNA is methylated by a

7. CONCLUSION AND OUTLOOK

modification enzyme (a methylase) to protect it from the restriction enzyme's activity. An example of an application based on this mechanism is the large scale production of human insulin for diabetics using *Escherichia coli* bacteria¹⁷⁸.

Currently, this cutting DNA step is routinely performed in research laboratories by putting the DNA molecules in a solution containing restriction enzymes. The current need is to realize the sequencing of the initial DNA strand in order to know the sequence of the nucleotide before being cut. Currently, the main methods for DNA sequencing are the Sanger sequencing¹⁷⁹ and the pyrosequencing¹⁸⁰. A potential alternative was imagined during a discussion with Prof. Schrenzel from HUG (Hôpitaux Universitaires de Genève), Prof. Lasser and Prof. Renaud from EPFL. This concept of DNA puzzle solver based on nanofluidics is shortly explained here.

First, protocols and methods for attaching microbeads at one extremity of a DNA strand are quite simple and well known¹⁸¹. Furthermore, Han *et al.*⁶⁷ have successfully shown the possibility to trap long DNA molecules in nanochannels using an electric field. So let's imagine that a fluorescently-labeled DNA strand is trapped in a nanochannel, maintained inside by a microbead.

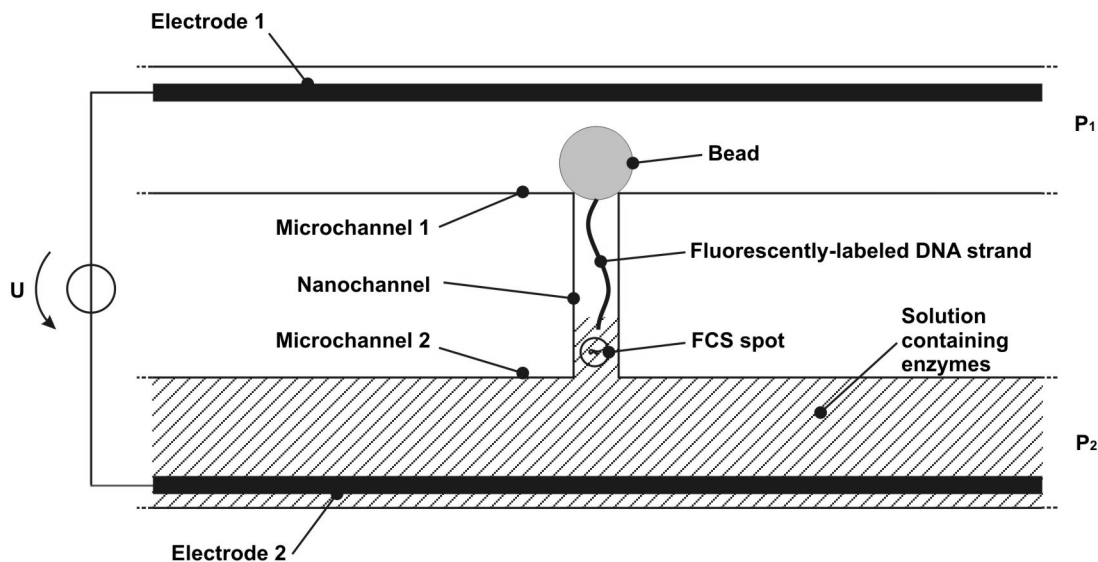


Figure 7.3: Concept of a nanofluidic system for identifying the order of sequences of nucleotide constituting the DNA strand before being cut by the restriction enzyme (top view). First a long DNA strand is attached to a microbead and is introduced in the nanochannel by the application of an electric field. Then, a solution containing the restriction enzymes is injected in the second microchannel and in the nanochannel by an external pressure difference ($P_2 > P_1$). As the enzymes front advances slowly in the nanochannel, it cuts the DNA strand into small pieces which are optically identified.

In figure 1.15, I have shown that the flat front of the injected fluorescently-labelled proteins was very slow due to the strong reduction of the effective diffusion in nanoconfined areas. Let's consider here that a solution containing non-charged restriction enzymes (k_{off} of the restriction enzyme should be low enough to strongly decrease the apparent diffusion coefficient, and the pH of the solution must match the pI of the enzymes) is injected in microchannel 2 and driven by pressure in the nanochannel with a similar slow front advance ($P_2 > P_1$). Consequently, the immobilized DNA strand in the nanochannel will be slowly cut when reacting with the restriction enzymes, and each cut sequence of nucleotide will cross the FCS spot and may be identified that reading the change of diffusion (assuming that the different cut sequences diffuse differently), giving information about the order of the nucleotide sequence initially constituting the DNA molecule. This scenario is depicted in figure 7.3.

Combine sieving, preconcentration and sensing

As seen in chapter 1, many research groups have successfully demonstrated the possibility to preconcentrate, sieve and sense different biomolecules, but until now, they have mainly concentrated their efforts on only one particular function. The next steps will consist of controlling and mixing all these functions in a single device, to perform direct manipulation and detection from solutions such as blood, saliva or urine, capable of performing the Western Blot, for example.

7.3 Concluding remarks

My deep conviction is that nanofluidics holds great promise for biomedical and biological diagnostics due to its capabilities to increase performance in detecting ultra-low concentrated solutions, and to decrease significantly the time to results. Even if the current technology is still very basic, novel models describing the diffusive transport of proteins have already been successfully elaborated. This thesis contributes to a better understanding of the biomolecular transport in nanofluidics.

I am persuaded it will be worthwhile to continue putting efforts in nanofluidics research and development in order to provide clinicians and biologists with the next generation of lab-on-a-chip for proteomics and diagnostics purposes.

7. CONCLUSION AND OUTLOOK

"Biology is not simply writing information; it is doing something about it. A biological system can be exceeding small. Many of the cells are very tiny, but they are very attractive; they manufacture various substances; they walk around; they wiggle; and they do all kinds of marvelous things, all on a very small scale. Also they store information. Consider the possibility that we too can make a thing very small which does what we want, that we can manufacture an object that maneuvers at that level!"

Richard Feynman, 1959

BIBLIOGRAPHY

- [1] M. Gad-el Hak. *The MEMS Handbook*, vol. 1. CRC, 2002.
- [2] A. S. et Sociales de l'Etat Francais. "Les déchets d'activités de soins.", 2009.
- [3] J. W. Hong and S. R. Quake. "Integrated nanoliter systems." *Nature Biotechnology*, **21**(10), 1179–1183, 2003.
- [4] J. C. T. Eijkel and A. Van den Berg. "Nanofluidics: what is it and what can we expect from it?" *Microfluidics and Nanofluidics*, **1**, 249–267, 2005.
- [5] R. B. Schoch. "Transport phenomena in nanofluidics." *Reviews of Modern Physics*, **80**, 839–883, 2008.
- [6] W. Sparreboom, A. Van Den Berg, and J. C. T. Eijkel. "Principles and applications of nanofluidic transport." *Nature Nanotechnology*, **4**(11), 713–720, 2009.
- [7] J. O. Tegenfeldt, C. Prinz, H. Cao, R. L. Huang, R. H. Austin, S. Y. Chou, E. C. Cox, and J. C. Sturm. "Micro- and nanofluidics for DNA analysis." *Analytical Bioanalytical Chemistry*, **378**(7), 1678–1692, 2004.
- [8] Y.-C. Wang, M. H. Choi, and J. Han. "Two-Dimensional Protein Separation with Advanced Sample and Buffer Isolation Using Microfluidic Valves." *Analytical Chemistry*, **76**, 4426–4431, 2004.
- [9] J. C. T. Eijkel and A. van den Berg. "The promise of nanotechnology for separation devices - From a top-down approach to nature-inspired separation devices." *Electrophoresis*, **27**(3), 677–685, 2006.

7. CONCLUSION AND OUTLOOK

- [10] Y.-C. Wang, A. L. Stevens, and J. Han. “Million-fold Preconcentration of Proteins and Peptides by Nanofluidic Filter.” *Analytical Chemistry*, **77**, 4293–4299, 2005.
- [11] W. A. Lyon and S. Nie. “Confinement and Detection of Single Molecules in Submicrometer Channels.” *Analytical Chemistry*, **69**(16), 3400–3405, 1997.
- [12] D. Mijatovic, J. C. T. Eijkel, and A. van den Berg. “Technologies for nanofluidic systems: top-down vs. bottom-up - a review.” *Lab on a Chip*, **5**(5), 492–500, 2005.
- [13] T. S. Hug, N. F. de Rooij, and U. Staufer. “Fabrication and electroosmotic flow measurements in micro- and nanofluidic channels.” *Microfluidics and Nanofluidics*, **2**(2), 117–124, 2006.
- [14] O. A. Saleh and L. L. Sohn. “An Artificial Nanopore for Molecular Sensing.” *Nano Letters*, **3**(1), 37–38, 2002.
- [15] J. Haneveld, H. Jansen, E. Berenschot, N. Tas, and M. Elwenspoek. “Wet anisotropic etching for fluidic 1D nanochannels.” *Journal of Micromechanics and Microengineering*, **13**(4), S62–S66, 2003.
- [16] P. Mao and J. Han. “Fabrication and characterization of 20nm planar nanofluidic channels by glass-glass and glass-silicon bonding.” *Lab on a Chip*, **5**(8), 837–844, 2005.
- [17] A. J. Storm, J. H. Chen, X. S. Ling, H. W. Zandbergen, and C. Dekker. “Fabrication of solid-state nanopores with single-nanometre precision.” *Nature Materials*, **2**(8), 537–540, 2003.
- [18] D. M. Cannon, B. R. Flachsbarth, M. A. Shannon, J. V. Sweedler, and P. W. Bohn. “Fabrication of single nanofluidic channels in poly(methylmethacrylate) films via focused-ion beam milling for use as molecular gates.” *Applied Physics Letters*, **85**(7), 1241–1243, 2004.
- [19] P. Scopece, L. A. Baker, P. Ugo, and C. R. Martin. “Conical nanopore membranes. solvent shaping of nanopores.” *Nanotechnology*, **17**, 3951–3956, 2006.
- [20] J. Li, D. Stein, C. McMullan, D. Branton, M. J. Aziz, and J. A. Golovchenko. “Ion-beam sculpting at nanometre length scales.” *Nature*, **412**(6843), 166–169, 2001.

- [21] K. Wang, S. Yue, L. Wang, A. Jin, C. Gu, P. Wang, H. Wang, X. Xu, Y. Wang, and H. Niu. “Nanofluidic channels fabrication and manipulation of DNA molecules.” *IEE Proceedings Nanobiotechnology*, **153**(1), 11–15, 2006.
- [22] R. B. Schoch, H. Van Lintel, and P. Renaud. “Effect of the surface charge on ion transport through nanoslits.” *Physics of Fluids*, **17**(10), 100604.1–3, 2005.
- [23] A. L. Cai, H. Y. Zhang, H. Hua, and Z. B. Zhang. “Direct formation of self-assembled nanoporous aluminium oxide on SiO₂ and Si substrates.” *Nanotechnology*, **13**(5), 627–630, 2002.
- [24] N. R. Tas, J. W. Berenschot, P. Mela, H. V. Jansen, M. Elwenspoek, and A. van den Berg. “2D-confined nanochannels fabricated by conventional micromachining.” *Nano Letters*, **2**(9), 1031–1032, 2002.
- [25] C. Lee, E. H. Yang, N. V. Myung, and T. George. “A nanochannel fabrication technique without nanolithography.” *Nano Letters*, **3**(10), 1339–1340, 2003.
- [26] A. Han, N. F. De Rooij, and U. Staufer. “Design and fabrication of nanofluidic devices by surface micromachining.” *Nanotechnology*, **17**(10), 2498–2503, 2006.
- [27] J. C. T. Eijkel, J. Bomer, N. R. Tas, and A. van den Berg. “1-D nanochannels fabricated in polyimide.” *Lab on a Chip*, **4**(3), 161–163, 2004.
- [28] W. Sparreboom, J. C. T. Eijkel, J. Bomer, and A. Van den Berg. “Rapid sacrificial layer etching for the fabrication of nanochannels with integrated metal electrodes.” *Lab on a Chip*, **8**, 402–407, 2008.
- [29] P. Takmakov, I. vlassiuk, and S. Smirnov. “Hydrothermally shrunk alumina nanopores and their application to DNA sensing.” *Analyst*, **131**, 1248–1253, 2006.
- [30] J. J. Dumond, H. Y. Low, and I. Rodriguez. “Isolated, sealed nanofluidic channels formed by combinatorial-mould nanoimprint lithography.” *Nanotechnology*, **17**(8), 1975–1980, 2006.
- [31] D. Huh, K. L. Mills, X. Zhu, M. A. Burns, M. D. Thouless, and S. Takayama. “Tunable elastomeric nanochannels for nanofluidic manipulation.” *Nature Materials*, **6**(6), 424–428, 2007.

7. CONCLUSION AND OUTLOOK

- [32] L. J. Guo, X. Cheng, and C.-F. Chou. “Fabrication of Size-Controllable Nanofluidic Channels by Nanoimprinting and Its Application for DNA Stretching.” *Nano Letters*, **4**(1), 69–73, 2004.
- [33] B. Ilic, D. Czaplewski, M. Zalalutdinov, B. Schmidt, and H. G. Craighead. “Fabrication of flexible polymer tubes for micro and nanofluidic applications.” *Journal of Vacuum Science and Technology B*, **20**(6), 2459–2465, 2002.
- [34] X. Wang, L. Ge, J. Lu, X. Li, K. Qiu, Y. Tian, S. Fu, and Z. Cui. “Fabrication of enclosed nanofluidic channels by UV cured imprinting and optimized thermal bonding of SU-8 photoresist.” *Microelectronic Engineering*, 2009.
- [35] C. Peng and S. W. Pang. “Three-dimensional nanochannels formed by fast etching of polymer.” *Journal of Vacuum Science and Technology B*, **24**(4), 1941–1946, 2006.
- [36] P. Sivanesan, K. Okamoto, D. English, C. S. Lee, and D. L. DeVoe. “Polymer nanochannels fabricated by thermomechanical deformation for single-molecule analysis.” *Analytical Chemistry*, **77**(7), 2252–2258, 2005.
- [37] C. C. Harrell, S. B. Lee, and C. R. Martin. “Synthetic single-nanopore and nanotube membranes.” *Analytical Chemistry*, **75**(24), 6861–6867, 2003.
- [38] B. R. Flachsbart, K. Wong, J. M. Iannacone, E. N. Abante, R. L. Vlach, P. A. Rauchfuss, P. W. Bohn, J. V. Sweedler, and M. A. Shannon. “Design and fabrication of a multilayered polymer microfluidic chip with nanofluidic interconnects via adhesive contact printing.” *Lab on a Chip*, **6**(5), 667–674, 2006.
- [39] C. Dekker. “Solid-state nanopores.” *Nature Nanotechnology*, **2**(4), 209–215, 2007.
- [40] L. M. Bellan, E. A. Strychalski, and H. G. Craighead. “Nanochannels fabricated in polydimethylsiloxane using sacrificial electrospun polyethylene oxide nanofibers.” *Journal of Vacuum Science and Technology B*, **26**(5), 1728–1731, 2008.
- [41] A. Noy, H. G. Park, F. Fornasiero, J. K. Holt, C. P. Grigoropoulos, and O. Bakajin. “Nanofluidics in carbon nanotubes.” *Nano Today*, **2**(6), 22–29, 2007.
- [42] L. Sun and R. M. Crooks. “Single carbon nanotube membranes: A well-defined model for studying mass transport through nanoporous materials.” *Journal of the American Chemical Society*, **122**(49), 12340–12345, 2000.

- [43] D. Mattia and Y. Gogotsi. “Review: static and dynamic behavior of liquids inside carbon nanotubes.” *Microfluidics and Nanofluidics*, **5**, 289–305, 2008.
- [44] K. P. Nichols, J. C. T. Eijkel, and H. J. G. E. Gardeniers. “Nanochannels in SU-8 with floor and ceiling metal electrodes and integrated microchannels.” *Lab on a Chip - Miniaturisation for Chemistry and Biology*, **8**(1), 173–175, 2007.
- [45] J. J. Kasianowicz, E. Brandin, D. Branton, and D. W. Deamer. “Characterization of individual polynucleotide molecules using a membrane channel.” *Proceedings of the National Academy of Sciences of the United States of America*, **93**(24), 13770–13773, 1996.
- [46] O. A. Saleh and L. L. Sohn. “Quantitative sensing of nanoscale colloids using a microchip Coulter counter.” *Review of Scientific Instruments*, **72**(12), 4449–4451, 2001.
- [47] J. L. Li, M. Gershow, D. Stein, E. Brandin, and J. A. Golovchenko. “DNA molecules and configurations in a solid-state nanopore microscope.” *Nature Materials*, **2**(9), 611–615, 2003.
- [48] D. Fologea, M. Gershow, B. Ledden, D. S. McNabb, J. A. Golovchenko, and J. Li. “Detecting Single Stranded DNA with a Solid State Nanopore.” *Nanoletters*, **5**(10), 1905–1909, 2005.
- [49] I. Vlassiuk, P. Takmakov, and S. Smirnov. “Sensing DNA Hybridization via Ionic Conductance through a Nanoporous Electrode.” *Langmuir*, **21**, 4776–4778, 2005.
- [50] O. A. Saleh and L. L. Sohn. “Direct detection of antibody-antigen binding using an on-chip artificial pore.” *Proceedings of the National Academy of Sciences of the United States of America*, **100**, 820–824, 2003.
- [51] J. D. Uram, K. Ke, A. J. Hunt, and M. Mayer. “Submicrometer pore-based characterization and quantification of antibody-virus interactions.” *Small*, **2**(8-9), 967–972, 2006.
- [52] S. M. Iqbal, D. Akin, and R. Bashir. “Solid-state nanopore channels with DNA selectivity.” *Nature Nanotechnology*, **2**(4), 243–248, 2007.
- [53] R. Fan, R. Karnik, M. Yue, D. Li, A. Majumdar, and P. Yang. “DNA Translocation in Inorganic Nanotubes.” *Nano letters*, **5**(9), 1633–1637, 2005.

7. CONCLUSION AND OUTLOOK

- [54] B. Bourlon, J. Wong, C. Miko, L. Forro, and M. Bockrath. “A nanoscale probe for fluidic and ionic transport.” *Nature Nanotechnology*, **2**(2), 104–107, 2007.
- [55] R. Karnik, K. Castelino, and A. Majumdar. “Field-effect control of protein transport in a nanofluidic transistor circuit.” *Applied Physics Letters*, **88**(12), 2006. 123114.
- [56] X. Wang, Y. Chen, K. A. Gibney, S. Erramili, and P. Mohanty. “Silicon-based nanochannel glucose sensor.” *Applied Physics Letters*, **92**, 013903, 2008.
- [57] H. Im, X. J. Huang, B. Gu, and Y. K. Choi. “A dielectric-modulated field-effect transistor for biosensing.” *Nature Nanotechnology*, **2**(7), 430–434, 2007.
- [58] I. Vlassiuk and Z. S. Siwy. “Nanofluidic Diode.” *Nano Letters*, **7**(3), 552–556, 2007.
- [59] R. Karnik, C. Duan, K. Castelino, H. Daiguji, and A. Majumdar. “Rectification of Ionic Current in a Nanofluidic Diode.” *Nano Letters*, **7**(3), 547–551, 2007.
- [60] M. Yi, K. H. Jeong, and L. P. Lee. “Theoretical and experimental study towards a nanogap dielectric biosensor.” *Biosensors and Bioelectronics*, **20**(7), 1320–1326, 2005.
- [61] R. Karnik, K. Castelino, R. Fan, P. Yang, and A. Majumdar. “Effect of Biological Reactions and Modifications on Conductance of Nanofluidic Channels.” *Nano Letters*, **5**(9), 1638–1642, 2005.
- [62] R. B. Schoch, L. F. Cheow, and J. Han. “Electrical detection of fast reaction kinetics in nanochannels with an induced flow.” *Nano Letters*, **7**(12), 3895–3900, 2007.
- [63] M. Foquet, J. Korlach, W. R. Zipfel, W. W. Webb, and H. G. Craighead. “Focal Volume Confinement by Submicrometer-Sized Fluidic Channels.” *Analytical Chemistry*, **76**, 1618–1626, 2004.
- [64] G. Lopez, A. Chilkoti, P. Atanassov, and V. Goparaju. “Stimuli responsive hybrid materials containing molecular actuators and their applications.” University of New Mexico, 2002. US 6,491,061 B1.
- [65] H. Cao, J. O. Tegenfeldt, S. Chou, and R. H. Austin. “Gradient structures interfacing microfluidics and nanofluidics, methods for fabrication and uses thereof.” Princeton University, 2007. US 7,217,562 B2.

- [66] S. Cruchon-Dupeyrat, M. Nelson, R. Elghanian, J. S. Fragala, I. Touzov, and D. Banerjee. “Methods and apparatus for ink delivery to nanolithographic probe systems.” NanoInk, Inc., 2005. US 2005/0035983 A1.
- [67] J. Han, S. W. Turner, and H. G. Craighead. “Entropic trapping and escape of long DNA molecules at submicron size constriction.” *Physical Review Letters*, **83**(8), 1688–1691, 1999.
- [68] J. Han and H. G. Craighead. “Entropic trapping and sieving of molecules.” Cornell Research Foundation, Inc., 2003. US 6,635,163 B1.
- [69] J. Fu, P. Mao, and J. Han. “Nanofilter array chip for last gel-free biomolecule separation.” *Applied Physics Letters*, **87**(263902), 2005.
- [70] G. B. Salieb-Beugelaar, K. D. Dorfman, A. Van Den Berg, and J. C. T. Eijkel. “Electrophoretic separation of DNA in gels and nanostructures.” *Lab on a Chip - Miniaturisation for Chemistry and Biology*, **9**(17), 2508–2523, 2009.
- [71] J. C. T. Eijkel and A. Van Den Berg. “Nanotechnology for membranes, filters and sieves.” *Lab on a Chip - Miniaturisation for Chemistry and Biology*, **6**(1), 19–23, 2006.
- [72] J. Fu, R. B. Schoch, A. L. Stevens, S. R. Tannenbaum, and J. Han. “A Patterned Anisotropic Nanofluidic Sieving Structure for Continuous-Flow Separation of DNA and Proteins.” *Nature Nanotechnology*, **2**, 121–128, 2007.
- [73] T. D. Yager, P. Waterhouse, A. M. Izmailov, B. Maruzzo, J. K. Stevens, and M. T. Larson. “Nanofabricated separation matrix for analysis of biopolymers and methods of biopolymers and methods of making and using same.” Visible Genetics, Inc., 2000. US 6,110,339.
- [74] G. P. Lopez, S. R. J. Brueck, L. K. Ista, M. O’Brien, and S. D. Hersee. “Nanostructured devices for separation and analysis.” Science & Technology Corporation (UNM), 2004. US 6,685,841 B2.
- [75] S. W. Turner, A. M. Perez, A. Lopez, and H. G. Craighead. “Monolithic nanofluid sieving structures for DNA manipulation.” *Journal of Vacuum Science and Technology B*, **16**(6), 3835–3840, 1998.
- [76] H. Cao, J. O. Tegenfeldt, R. H. Austin, and S. Y. Chou. “Gradient nanostructures for interfacing microfluidics and nanofluidics.” *Applied Physics Letters*, **81**(16), 3058–3060, 2002.

7. CONCLUSION AND OUTLOOK

- [77] J. W. Lee and T. G. Thundat. “DNA and RNA sequencing by nanoscale reading through programmable electrophoresis and nanoelectrode-gated tunneling and dielectric detection.” UT-Battelle, LLC, 2005. US 6,905,586 B2.
- [78] Y. C. Wang, J. Fu, P. Mao, and J. Han. “Nanofluidic molecular filters for efficient protein separation and preconcentration.” In “International Conference on Solid State Sensors and Actuators and Microsystems, Transducers 05,” vol. 1, pp. 352–355. 2005.
- [79] Y.-C. Wang and J. Han. “Pre-binding dynamic range and sensitivity enhancement for immuno-sensors using nanofluidic preconcentrator.” *Lab on a Chip*, **8**, 392–394, 2008.
- [80] A. Plecis, C. Nanteuil, A.-M. Haghiri-Gosnet, and Y. Chen. “Electroconcentration with Charge-Selective Nanochannels.” *Analytical Chemistry*, **80**, 9542–9550, 2008.
- [81] J. Khandurina, S. C. Jacobson, L. C. Waters, R. S. Foote, and J. M. Ramsey. “Microfabricated porous membrane structure for sample concentration and electrophoretic analysis.” *Analytical Chemistry*, **71**(9), 1815–1819, 1999.
- [82] R. S. Foote, J. Khandurina, S. C. Jacobson, and J. M. Ramsey. “Preconcentration of proteins on microfluidic devices using porous silica membranes.” *Analytical Chemistry*, **77**(1), 57–63, 2005.
- [83] T. Kim and E. Meyhöfer. “Nanofluidic Concentration of Selectively Extracted Biomolecule Analytes by Microtubules.” *Analytical Chemistry*, 2008.
- [84] M. S. Munson, K. R. Hawkins, M. S. Hasenbank, and P. Yager. “Diffusion based analysis in a sheath flow microchannel: The sheath flow T-sensor.” *Lab on a Chip*, **5**(8), 856–862, 2005.
- [85] D. Henderson and M. Lozada-Cassou. “A simple theory for the force between spheres immersed in a fluid.” *Journal of Colloid and Interface Science*, **114**(1), 180–183, 1986.
- [86] P. G. De Gennes. “Polymers at an interface; a simplified view .” *Advances in Colloid and Interface Science*, **27**((3-4)), 189–209, 1987.
- [87] J. Israelachvili. *Intermolecular & Surface Forces*. Academic Press Limited, London, 2nd ed., 1992.

- [88] G. K. Batchelor. *An introduction to fluid dynamics*. Cambridge University Press, 1967.
- [89] C. J. Van Oss, M. K. Chaudhury, and R. J. Good. “Interfacial Lifshitz-van der Waals and polar interactions in macroscopic systems.” *Chemical Reviews*, **88**(6), 927–941, 1988.
- [90] H. J. Taunton, C. Toprakcioglu, L. J. Fetters, and J. Klein. “Interactions between surfaces bearing end-adsorbed chains in a good solvent.” *Macromolecules*, **23**(2), 571–580, 1990.
- [91] R. Zangi. “Water confined to a slab geometry: a review of recent computer simulation studies.” *Journal of Physics: Condensed Matter*, **16**, S5371 – S5388, 2004.
- [92] A. S. Ziarani and A. A. Mohamad. “A molecular dynamics study of perturbed Poiseuille flow in a nanochannel .” *Microfluidics and Nanofluidics*, **2**, 12–20, 2005.
- [93] O. Renolds. “An Experimental Investigation of the Circumstances Which Determine Whether the Motion of Water Shall Be Direct or Sinuous, and of the Law of Resistance in Parallel Channels .” *Philosophical Transactions of the Royal Society of London*, **174**, 935–982, 1883.
- [94] A. Einstein, R. Furth, and A. D. Cowper. *Investigations on the Theory of the Brownian Movement*. Courier Dover Publications, New York, 1956.
- [95] J. Crank. *The Mathematics of Diffusion*. Clarendon Press, Oxford, 2nd ed., 1975.
- [96] T. F. Tadros and J. Lyklema. “Adsorption of Potential-Determining Ions at Silica-Aqueous Electrolyte Interface and Role Of some Cations.” *Journal of Electroanalytical Chemistry*, **17**, 267, 1968.
- [97] J. T. G. Overbeek. “Thermodynamics of electrokinetic phenomena.” *Journal of Colloid Science*, **8**(4), 420–427, 1953.
- [98] R. J. Hunter. *Zeta Potential in Colloid Science, Principles and Applications*. Academic Press, London, 1981.
- [99] J. C. T. Eijkel and A. Van den Berg. “Nanofluidics and the chemical potential applied to solvent and solute transport.” *Chem Society Reviews*, **39**, 957–973, 2010.

7. CONCLUSION AND OUTLOOK

- [100] F. Hofmeister. “Zur Lehre von der Wirkung der Salze - Zweite Mittheilung.” *Archiv für Experimentelle Pathologie und Pharmakologie*, **24**(4-5), 247–260, 1888.
- [101] H. Chick and C. J. Martin. “On the "heat coagulation" of proteins. Part II. The action of hot water upon egg-albumen and the influence of acid and salts upon reaction velocity.” *Journal of Physiology*, **43**, 1–27, 1911.
- [102] D. Stigter, D. O. V. Alonso, and K. A. Dill. “Protein stability: Electrostatics and compact denatured states.” *Proceedings of the National Academy of Sciences of the United States of America*, **88**(10), 4176–4180, 1991.
- [103] U. Bohme and U. Scheler. “Effective charge of bovine serum albumin determined by electrophoresis NMR.” *Chemical Physics Letters*, **435**(4-6), 342–345, 2007.
- [104] W. Sparreboom, A. Van Den Berg, and J. C. T. Eijkel. “Transport in nanofluidic systems: A review of theory and applications.” *New Journal of Physics*, **12**, 2010.
- [105] Y. M. Wang, J. O. Tegenfeldt, W. Reisner, R. Riehn, X. J. Guan, L. Guo, I. Golding, E. C. Cox, J. Sturm, and R. H. Austin. “Single-molecule studies of repressor-DNA interactions show long-range interactions.” *Proceedings of the National Academy of Sciences of the United States of America*, **102**(28), 9796–9801, 2005.
- [106] A. Plecis, R. B. Schoch, and P. Renaud. “Ionic Transport Phenomena in Nanofluidics: Experimental and Theoretical Study of the Exclusion-Enrichment Effect on a Chip.” *Nano letters*, **5**(6), 1147–1155, 2005.
- [107] R. B. Schoch, A. Bertsch, and P. Renaud. “pH-Controlled Diffusion of Proteins with Different pI Values Across a Nanochannel on a Chip.” *Nano letters*, **6**(3), 543–547, 2006.
- [108] R. B. Schoch and P. Renaud. “Ion transport through nanoslits dominated by the effective surface charge.” *Applied Physics Letters*, **86**, 253111–3, 2005.
- [109] H. Scholze. “Glass-water interactions.” *Journal of Non-Crystalline Solids*, **102**(1-3), 1–10, 1988.
- [110] C. Calonder, Y. Tie, and P. R. Van Tassel. “History dependence of protein adsorption kinetics.” *Proceedings of the National Academy of Sciences of the United States of America*, **98**(19), 10664–10669, 2001.

- [111] Y. Tie, C. Calonder, and P. R. Van Tassel. “Protein adsorption: Kinetics and history dependence.” *Journal of Colloid and Interface Science*, **268**(1), 1–11, 2003.
- [112] M. Malmsten, G. Siegel, and W. G. Wood. “Ellipsometry studies of lipoprotein adsorption.” *Journal of Colloid and Interface Science*, **224**(2), 338–346, 2000.
- [113] C. F. Wertz and M. M. Santore. “Adsorption and relaxation kinetics of albumin and fibrinogen on hydrophobic surfaces: Single-species and competitive behavior.” *Langmuir*, **15**(26), 8884–8894, 1999.
- [114] C. F. Wertz and M. M. Santore. “Effect of surface hydrophobicity on adsorption and relaxation kinetics of albumin and fibrinogen: Single-species and competitive behavior.” *Langmuir*, **17**(10), 3006–3016, 2001.
- [115] C. F. Wertz and M. M. Santore. “Adsorption and reorientation kinetics of lysozyme on hydrophobic surfaces.” *Langmuir*, **18**(4), 1190–1199, 2002.
- [116] C. T. Shibata and A. M. Lenhoff. “TIRF of salt and surface effects on protein adsorption. I. Equilibrium.” *Journal of Colloid and Interface Science*, **148**(2), 469–484, 1992.
- [117] C. T. Shibata and A. M. Lenhoff. “TIRF of salt and surface effects on protein adsorption. II. Kinetics.” *Journal of Colloid and Interface Science*, **148**(2), 485–507, 1992.
- [118] D. R. Shankaran, K. V. Gobi, and N. Miura. “Recent advancements in surface plasmon resonance immunosensors for detection of small molecules of biomedical, food and environmental interest.” *Sensors and Actuators B: Chemical*, **121**(1), 158–177, 2007.
- [119] R. L. Rich and D. G. Myszka. “Advances in surface plasmon resonance biosensor analysis.” *Current Opinion in Biotechnology*, **11**(1), 54–61, 2000.
- [120] S. Sjolander and C. Urbaniczky. “Integrated fluid handling system for biomolecular interaction analysis.” *Analytical Chemistry*, **63**(20), 2338–2345, 1991.
- [121] N. Lion, F. Reymond, H. H. Girault, and J. S. Rossier. “Why the move to microfluidics for protein analysis?” *Current Opinion in Biotechnology*, **15**(1), 31–37, 2004.

7. CONCLUSION AND OUTLOOK

- [122] W. H. Reinmuth. “Diffusion to a plane with Langmuirian adsorption.” *Journal of Physical and Chemical Reference Data*, **65**(3), 473–476, 1961.
- [123] W. Norde. “My voyage of discovery to proteins in flatland ...and beyond.” *Colloids and Surfaces B: Biointerfaces*, **61**(1), 1–9, 2008.
- [124] W. Norde. “Adsorption of proteins from solution at the solid-liquid interface.” *Advances in Colloid and Interface Science*, **25**(4), 267–340, 1986.
- [125] M. A. C. Stuart, G. J. Fleer, J. Lyklema, W. Norde, and J. M. H. M. Scheutjens. “Adsorption of ions, polyelectrolytes and proteins.” *Advances in Colloid and Interface Science*, **34**, 477–535, 1991.
- [126] W. M. Deen. “Hindered Transport of Large Molecule in Liquid-Filled Pores.” *AIChE Journal*, **33**(9), 1409–1425, 1987.
- [127] P. Dechadilok and W. M. Deen. “Hindrance factors for diffusion and convection in pores.” *Industrial and Engineering Chemistry Research*, **45**(21), 6953–6959, 2006.
- [128] J. Shao and R. E. Baltus. “Hindered diffusion of dextran and polyethylene glycol in porous membranes.” *AIChE Journal*, **46**(6), 1149–1156, 2000.
- [129] M. Ladero, A. Santos, and F. Garcia-Ochoa. “Hindered diffusion of proteins and polymethacrylates in controlled-pore glass: An experimental approach.” *Chemical Engineering Science*, **62**(3), 666–678, 2007.
- [130] J. L. Anderson and J. A. Quinn. “Restricted transport in small pores. A model for steric exclusion and hindered particle motion.” *Biophysical Journal*, **14**(2), 130–150, 1974.
- [131] Y. Pawar and J. L. Anderson. “Hindered diffusion in slit pores: An analytical result.” *Industrial and Engineering Chemistry Research*, **32**(4), 743–746, 1993.
- [132] D. Stein, M. Kruithof, and C. Dekker. “Surface-charge-governed ion transport in nanofluidic channels.” *Physical Review Letters*, **93**(3), 035901, 2004.
- [133] J.-Y. Yoon and R. L. Garrell. “Using a Stirred Cell to Evaluate Structural Changes in Proteins Adsorbed on Particles.” *AIChE Journal*, **51**(3), 1048–1052, 2005.

- [134] M. R. Duncan, J. M. Lee, and M. P. Warchol. “Influence of surfactants upon protein/peptide adsorption to glass and polypropylene.” *International Journal of Pharmaceutics*, **120**(2), 179–188, 1995.
- [135] W. M. Clark, A. Bansal, M. Sontakke, and Y. H. Ma. “Protein adsorption and fouling in ceramic ultrafiltration membranes.” *Journal of Membrane Science*, **55**(1-2), 21–38, 1991.
- [136] M. Malmsten. *Biopolymers at interfaces*, vol. 110 of *Surfactant Science Series*. M. Dekker, 2003.
- [137] E. J. Van Der Wouden, D. C. Hermes, J. G. E. Gardeniers, and A. Van Den Berg. “Directional flow induced by synchronized longitudinal and zeta-potential controlling AC-electrical fields.” *Lab on a Chip*, **6**(10), 1300–1305, 2006.
- [138] L. J. Bousse, S. Mostarshed, and D. Hafeman. “Combined measurement of surface potential and zeta potential at insulator/electrolyte interfaces.” *Sensors and Actuators B: Chemical*, **B10**(1), 67–71, 1992.
- [139] P. Schwille and E. Haustein. *Fluorescence Correlation Spectroscopy, An Introduction to its Concepts and Applications*. Experimental Biophysics Group, Max-Planck-Institute for Biophysical Chemistry, 2004.
- [140] O. Krichevsky and G. Bonnet. “Fluorescence correlation spectroscopy: the technique and its applications.” *Reports on Progress in Physics*, **65**, 251–297, 2002.
- [141] H. G. Craighead, S. M. Stavis, and K. T. Samiee. “Nanodevices for single molecule studies.” *Lecture Notes in Physics*, **711**, 271–301, 2007.
- [142] M. Leutenegger, M. Gosch, A. Perentes, P. Hoffmann, O. J. F. Martin, and T. Lasser. “Confining the sampling volume for fluorescence correlation spectroscopy using a sub-wavelength sized aperture.” *Optics Express*, **14**(2), 956–969, 2006.
- [143] S. R. Aragon and R. Pecora. “Fluorescence correlation spectroscopy as a probe of molecular dynamics.” *Journal of Chemical Physics*, **64**(4), 1791–1803, 1976.
- [144] D. E. Koppel. “Statistical accuracy in fluorescence correlation spectroscopy.” *Physical Review A*, **10**(6), 1938–1945, 1974.

7. CONCLUSION AND OUTLOOK

- [145] M. Wachsmuth, W. Waldeck, and J. Langowski. “Anomalous diffusion of fluorescent probes inside living cell investigated by spatially-resolved fluorescence correlation spectroscopy.” *Journal of Molecular Biology*, **298**(4), 677–689, 2000.
- [146] M. J. Saxton and K. Jacobson. “Single-particle tracking: Applications to membrane dynamics.” *Annual Review of Biophysics and Biomolecular Structure*, **26**, 373–399, 1997.
- [147] M. J. Wirth and M. A. Legg. “Single-molecule probing of adsorption and diffusion on silica surfaces.” *Annual Review of Physical Chemistry*, **58**, 489–510, 2007.
- [148] I. Hanasaki, H. Takahashi, G. Sazaki, K. Nakajima, and S. Kawano. “Single-molecule measurements and dynamical simulations of protein molecules near silicon substrates.” *Journal of Physics D: Applied Physics*, **41**(9), 2008.
- [149] N. F. Y. Durand, A. Bertsch, M. Todorova, and P. Renaud. “Direct measurement of effective diffusion coefficients in nanochannels using steady-state dispersion effects.” *Applied Physics Letters*, **91**, 203106–3, 2007.
- [150] K. Pappaert, J. Biesemans, D. Clicq, S. Vankrunkelsven, and G. Desmet. “Measurements of diffusion coefficients in 1-D micro- and nanochannels using shear-driven flows.” *Lab on a Chip*, **5**(10), 1104–1110, 2005.
- [151] M. Kosmulski and E. Matijevic. “Zeta-potentials of silica in water-alcohol mixtures.” *Langmuir*, **8**(4), 1060–1064, 1992.
- [152] E. Cussler. *Diffusion, Mass Transfer in Fluid Systems*, vol. Second Edition. Cambridge University Press, 1997.
- [153] R. J. Green, J. Davies, M. C. Davies, C. J. Roberts, and S. J. B. Tendler. “Surface plasmon resonance for real time in situ analysis of protein adsorption to polymer surfaces.” *Biomaterials*, **18**(5), 405–413, 1997.
- [154] Y. L. Cheng, S. A. Darst, and C. R. Robertson. “Bovine serum albumin adsorption and desorption rates on solid surfaces with varying surface properties.” *Journal of Colloid and Interface Science*, **118**(1), 212–223, 1987.
- [155] R. Karlsson, A. Michaelsson, and L. Mattsson. “Kinetic analysis of monoclonal antibody-antigen interactions with a new biosensor based analytical system.” *Journal of Immunological Methods*, **145**(1-2), 229–240, 1991.

- [156] J. Gutenwik, B. Nilsson, and A. Axelsson. “Determination of protein diffusion coefficients in agarose gel with a diffusion cell.” *Biochemical Engineering Journal*, **19**(1), 1–7, 2004.
- [157] A. C. Ouano. “Diffusion in liquid systems. I. A simple and fast method of measuring diffusion constants.” *Industrial and Engineering Chemistry Fundamentals*, **11**(2), 268–271, 1972.
- [158] H. Kempe, P. Persson, A. Axelsson, B. Nilsson, and G. Zacchi. “Determination of diffusion coefficients of proteins in stationary phases by frontal chromatography.” *Biotechnology and Bioengineering*, **93**(4), 656–664, 2006.
- [159] C. B. Ahn, S. Y. Lee, O. Nalcioglu, and Z. H. Cho. “An improved nuclear magnetic resonance diffusion coefficient imaging method using an optimized pulse sequence.” *Medical Physics*, **13**(6), 789–793, 1986.
- [160] N. Baden and M. Terazima. “A novel method for measurement of diffusion coefficients of proteins and DNA in solution.” *Chemical Physics Letters*, **393**(4-6), 539–545, 2004.
- [161] J. L. Duda, W. L. Sigelko, and J. S. Vrentas. “Binary diffusion studies with a wedge interferometer.” *Journal of Physical Chemistry*, **73**(1), 141–149, 1969.
- [162] L. Leoni, A. Boiarski, and T. A. Desai. “Characterization of nanoporous membranes for immunoisolation: Diffusion properties and tissue effects.” *Biomedical Microdevices*, **4**(2), 131–139, 2002.
- [163] M. K. Menon and A. L. Zydney. “Effect of ion binding on protein transport through ultrafiltration membranes.” *Biotechnology and Bioengineering*, **63**(3), 298–307, 1999.
- [164] R. L. Panton. *Incompressible flow*, vol. 3. John Wiley & Sons, Inc., 2005.
- [165] P. S. Williams, S. Levin, T. Lenczycki, and J. C. Giddings. “Continuous SPLITT fractionation based on a diffusion mechanism.” *Industrial and Engineering Chemistry Research*, **31**(9), 2172–2181, 1992.
- [166] A. Hatch, A. E. Kamholz, K. R. Hawkins, M. S. Munson, E. A. Schilling, B. H. Weigl, and P. Yager. “A rapid diffusion immunoassay in a T-sensor.” *Nature Biotechnology*, **19**(5), 461–465, 2001.

7. CONCLUSION AND OUTLOOK

- [167] A. J. Chmura, M. S. Orton, and C. F. Meares. “Antibodies with infinite affinity.” *Proc. Natl. Sci. USA*, **98**(15), 8480–8484, 2001.
- [168] P. Takmakov, I. Vlassiuk, and S. Smirnov. “Application of anodized aluminum in fluorescence detection of biological species.” *Analytical and Bioanalytical Chemistry*, **385**(5), 954–958, 2006.
- [169] R. B. H. Veenhuis, E. J. Van Der Wouden, J. W. Van Nieuwkasteele, A. Van Den Berg, and J. C. T. Eijkel. “Field-effect based attomole titrations in nanoconfinement.” *Lab on a Chip - Miniaturisation for Chemistry and Biology*, **9**(24), 3472–3480, 2009.
- [170] N. L. Thompson and B. L. Steele. “Total internal reflection with fluorescence correlation spectroscopy.” *Nature Protocols*, **2**(4), 878–890, 2007.
- [171] A. M. Lieto, R. C. Cush, and N. L. Thompson. “Ligand-Receptor Kinetics Measured by Total Internal Reflection with Fluorescence Correlation Spectroscopy.” *Biophysical Journal*, **85**(5), 3294–3302, 2003.
- [172] S. G. Penn, L. He, and M. J. Natan. “Nanoparticles for bioanalysis.” *Current Opinion in Chemical Biology*, **7**(5), 609–615, 2003.
- [173] S. M. Bezrukov, I. Vodyanoy, and V. A. Parsegian. “Counting polymers moving through a single ion channel.” *Nature*, **370**(6487), 279–281, 1994.
- [174] R. Weiss, W. M. Roberts, W. Stuhmer, and W. Almers. “Mobility of Voltage-dependant Ion Channels and Lectin Receptors in the Sarcolemma of Frog Skeletal Muscle.” *J. Gen. Physiol.*, **87**, 955–983, 1986.
- [175] S. Pennathur and D. K. Fygenson. “Improving fluorescence detection in lab on chip devices.” *Lab on a Chip - Miniaturisation for Chemistry and Biology*, **8**(5), 649–652, 2008.
- [176] A. H. J. Yang, S. D. Moore, B. S. Schmidt, M. Klug, M. Lipson, and D. Erickson. “Optical manipulation of nanoparticles and biomolecules in sub-wavelength slot waveguides.” *Nature*, **457**(7225), 71–75, 2009.
- [177] W. Arber and S. Linn. “DNA modification and restriction.” *Annual Review of Biochemistry*, **38**, 467–500, 1969.

- [178] L. Villa-Komaroff, A. Efstratiadis, and S. Broome. “A bacterial clone synthesizing proinsulin.” *Proceedings of the National Academy of Sciences of the United States of America*, **75**(8), 3727–3731, 1978.
- [179] F. Sanger, S. Nicklen, and A. R. Coulson. “DNA sequencing with chain-terminating inhibitors.” *Proceedings of the National Academy of Sciences of the United States of America*, **74**(12), 5463–5467, 1977.
- [180] M. Ronaghi. “Pyrosequencing sheds light on DNA sequencing.” *Genome Research*, **11**(1), 3–11, 2001.
- [181] M. D. Wang, H. Yin, R. Landick, J. Gelles, and S. M. Block. “Stretching DNA with optical tweezers.” *Biophysical Journal*, **72**(3), 1335–1346, 1997.

7. CONCLUSION AND OUTLOOK

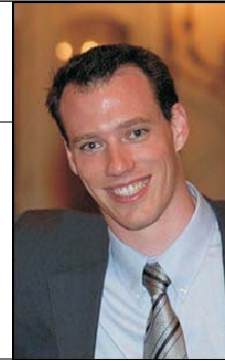
APPENDIX

A

CURRICULUM VITAE

A. CURRICULUM VITAE

Nicolas F.Y. Durand



Date of birth: February 12, 1982
Marital status: Married
Nationality: Swiss and European (French)

Education

- | | |
|-------------|---|
| 2006 – 2010 | Swiss Federal Institute of Technology Lausanne (EPFL), Switzerland
Ph.D. (Dr. ès Sciences) in Nanosystems and Biotechnology |
| 2005 – 2006 | Carnegie Mellon University (CMU), USA
Master thesis : <i>Conception and Investigation of Resonating Biosensors</i> |
| 2000 – 2005 | Swiss Federal Institute of Technology Lausanne (EPFL), Switzerland
MSc. (Master of Science) in Microengineering |
| 1997 – 2000 | College of Beaulieu, Lausanne, Switzerland
Highschool Baccalaureate |

Awards

- | | |
|------|---|
| 2010 | Young Entrepreneur Award
for the best entrepreneurial project in connection with France
(supported by the French Advisory Committee for Foreign Trade in Switzerland). |
| 2010 | 1st Prize of the Trophées PERL (Prix Entreprendre Région Lausanne)
for the best entrepreneurial project elaborated in Lausanne area. |
| 2010 | KPMG Inspiration Grant
supported by KPMG and EPFL. |
| 2010 | Co-Captain of the Swiss Start-up national team (Venture Leaders)
supported by the Innovation Promotion Agency (Venturelab & CTI). |
| 2006 | OMEGA Award
for one of the best Master theses in Microengineering |

Languages

- | | |
|----------------|--|
| French | Native |
| English | Fluent (Master's thesis conducted in USA) |
| German | Good knowledge (Parts of military service conducted in German) |

Research and Industrial Experience

From 2010	Abionic, Switzerland Chief Executive Officer (CEO)
2007 – 2010	Swiss Federal Institute of Technology Lausanne (EPFL), Switzerland Group Information Technology (IT) Manager
2006 – 2007	Swiss Federal Institute of Technology Lausanne (EPFL), Switzerland Teaching assistant of Prof. Theo Lasser for the lecture "Biomicroscopy"
2005	European Space Agency (ESA), Netherlands Realization of an autonomous satellite and testing in microgravity during the 8th Student Parabolic Flight Campaign (under supervision of Prof. Claude Nicollier)
2004 – 2005	Swiss Federal Institute of Technology Lausanne (EPFL), Switzerland Teaching assistant of Prof. Philippe Renaud for the lecture "Sensors and actuators"
2004	Fluid Automation System SA, Versoix, Switzerland Internship in the R&D department. Realization of a micro pressure regulator
1999 – 2000	State of Vaud, College of Beaulieu, Switzerland Computer expert

Further skills and interests

Aeronautical	Private Pilot , May 2002 Acrobatic Flight license, July 2005 Founder and President of the Aeronautical Association of EPFL (AéroPoly, 135 members), 2007-09 Organization of several regional conferences Astronaut candidate (400 / 50,000) European Space Agency, 2008
Military	Explorer Officer (Platoon Chief, First-Lieutenant) Swiss Ground Forces, 2003
Nautical	Motor boat license Several sea sailing cruises
Robotic	President of the Robotic Association of EPFL (Robopoly), 2002-04 Creation of the "Avril" robot (50 fabricated), April 2002 Conception of the "Prisme" robotic platform (500 fabricated), 2003-08
Sports	Ski touring, trekking, squash, nautical sports
Scouts	11 years of boyscouting, 2 years as unit chief, Lausanne, 1990-2001

A. CURRICULUM VITAE

APPENDIX

B

PUBLICATIONS

B. PUBLICATIONS

Peer-reviewed papers

N.F.Y. Durand, C. Dellagiacomma, R. Goetschmann, A. Bertsch, I. Märki, T. Lasser and P. Renaud, "Direct observation of transitions between surface-dominated and bulk diffusion regimes in nanochannels", *Analytical Chemistry*, **81**, 5407-5412, 2009.

N.F.Y. Durand and P. Renaud, "Label-free determination of protein-surface interaction kinetics by ionic conductance inside a nanochannel", *Lab on a Chip*, **9**(2), 319-324, 2009.

Editorial choice for *Virtual Journal of Nanoscale Science and Technology*, **19**(3), 2009.

N.F.Y. Durand, E. Saveriades and P. Renaud, "Detecting proteins complex formation using steady-state diffusion in a nanochannel", *Analytical Bioanalytical Chemistry*, **394**(2), 421-425, 2009.

N.F.Y. Durand, C. Dellagiacomma, R. Goetschmann, A. Bertsch, I. Märki, T. Lasser and P. Renaud, "Direct measurement of diffusing proteins in nanochannels using fluorescence correlation spectroscopy", *Procedia Chemistry*, **1**(1), 1343-1346, 2009.

N.F.Y. Durand, A. Bertsch, M. Todorova and P. Renaud, "Direct measurement of effective diffusion coefficients in nanochannels using steady-state dispersion effects", *Applied Physics Letters*, **91**, 203106, 2007.

Editorial choice for *Virtual Journal of Nanoscale Science and Technology*, **16**(22), 2007, and for *Virtual Journal of Biological Physics Research*, **14**(10), 2007.

N.F.Y. Durand, I. Märki, G. del Val, P. Renaud and T. Lasser, "Diffusion-based nanofluidic device for rapid immuno-sensing", to be published.

Patents

N.F.Y. Durand, I. Märki and T. Lasser, "APPARATUS AND METHOD FOR DETECTING AND MEASURING BIOMOLECULAR INTERACTIONS", International Patent Application, PCT/IB2010/050867, 2010.

N.F.Y. Durand, Y. Fournier and T. Lasser, "NANOFLUIDIC BIOSENSOR AND ITS USE FOR RAPID MEASUREMENT OF BIOMOLECULAR INTERACTIONS IN SOLUTION AND METHODS", International Patent Application, PCT/01824/09, 2009.

Proceedings

N.F.Y. Durand, C. Dellagiacomma, R. Goetschmann, A. Bertsch, I. Märki, T. Lasser and P. Renaud, "Direct measurement of diffusing proteins in nanochannels using fluorescence correlation spectroscopy", Proceedings of *The 23rd European Conference on Sensors, Actuators and Microsystems (Euroensors)*, Sep. 6-9, 2009, Lausanne, Switzerland.

N.F.Y. Durand, F. Wildhaber and P. Renaud, "Nanofluidic platform for label-free proteins detection", Proceedings of *The 5th International Conference on Microtechnologies in Medicine and Biology (MMB)*, Apr. 1-3, 2009, Quebec City, Canada.

Proceedings (continued)

N.F.Y. Durand, E. Saveriades, and P. Renaud, "Competitive dispersion immunoassay based on nanofluidic inverted H-filter", Proceedings of *The Annual European Conference on Microscale and Nanoscale Technologies for the Biosciences (NanoTech)*, Nov. 17-19, 2008, Montreux, Switzerland.

N.F.Y. Durand, E. Saveriades, A. Valero and P. Renaud, "Rapid immunoassay using steady-state dispersion effects in nanochannels", Proceedings of *The 12th International Conference on Miniaturized Systems for Chemistry and Life Sciences (MicroTAS)*, Oct. 12-16, 2008, San Diego, USA.

N.F.Y. Durand, A. Bertsch, and P. Renaud, "A novel method for determining the effective diffusion coefficients of proteins into confined areas", Proceedings of *The Union of the Swiss Societies for Experimental Biology (USGEB)*, Feb. 6-7, 2008, Lausanne, Switzerland.

N.F.Y. Durand, M. Todorova, A. Bertsch, and P. Renaud, "Determining the diffusion coefficients of proteins inside a nanoslit", Proceedings of *The Annual European Conference on Microscale and Nanoscale Technologies for the Biosciences (NanoTech)*, Nov. 14-16, 2007, Montreux, Switzerland.

C. Dellagiacomma, **N.F.Y. Durand**, R. Goetschmann, I. Märki, A. Bertsch, P. Renaud and T. Lasser, "Diffusion of single molecules in nanochannels", Proceedings of *Biomedical Photonics Network day 2009 (BMPN)*, Jun. 10, 2009, St. Gallen, Switzerland.

C. Dellagiacomma, **N.F.Y. Durand**, R. Goetschmann, I. Märki, A. Bertsch, P. Renaud and T. Lasser, "Diffusion of single molecules in nanochannels", Proceedings of *The European Conferences on Biomedical Optics (ECBO)*, Jun. 14-18, 2009, Munich, Germany.

Invited speaker presentation

N.F.Y. Durand, "Protein transport phenomena in nanofluidic channels", *MicroNanoFabrication Annual Review Meeting*, CMI, EPFL, Lausanne, Switzerland, May 19, 2009.

Thesis-based company creation

"**Abionic SA**", Start-up aiming to provide a new generation of portable biomedical diagnostic devices based on nanofluidics, 2010.

Press releases (results featured in the news)

24 Heures: "Abionic tient à alléger le processus de détection des allergies", March 15, 2010.

Le Temps: "Abionic veut développer des tests d'allergies rapides et indolores", April 6, 2010.

24 Heures: "Abionic remporte le Premier Prix des Trophées PERL", April 21, 2010.

Le Temps: "Nouveau prix pour Abionic", April 22, 2010.

La Télé: "Détecer les allergies en quelques minutes", April 23, 2010.

Le Régional: "L'innovation distinguée à Beaulieu", April 27, 2010.

Flash EPFL: "Pour la 3ème fois, le "Prix du Jeune Entrepreneur" est remporté par un étudiant de l'EPFL", May 19, 2010.